



3 1293 00895 7296

This is to certify that the
dissertation entitled
Conceptual Design and Orbit Dynamics in a 250 MeV
Superconducting Synchrocyclotron
presented by
Xiaoyu Wu
has been accepted towards fulfillment
of the requirements for
Ph. D degree in Physics

M M Gordon

Major professor

Date 11/29/90

**LIBRARY
Michigan State
University**

PLACE IN RETURN BOX to remove this checkout from your record.
TO AVOID FINES return on or before date due.

DATE DUE	DATE DUE	DATE DUE
_____	_____	_____
_____	_____	_____
_____	_____	_____
_____	_____	_____
_____	_____	_____
_____	_____	_____
_____	_____	_____

MSU Is An Affirmative Action/Equal Opportunity Institution

c:\circ\dtedue.pm3-p.1

CONCEPTUAL DESIGN AND ORBIT DYNAMICS IN A 250 MeV
SUPERCONDUCTING SYNCHROCYCLOTRON

by

XiaoYu Wu

A DISSERTATION

Submitted to
Michigan State University
in partial fulfillment of the requirements
for the degree of

DOCTOR OF PHILOSOPHY

Department of Physics and Astronomy

1990

ABSTRACT

CONCEPTUAL DESIGN AND ORBIT DYNAMICS IN A 250 MeV
SUPERCONDUCTING SYNCHROCYCLOTRON

by

XiaoYu Wu

A feasibility study has been carried out on a 250 MeV superconducting synchrocyclotron specifically designed for use in cancer therapy. A superconducting magnet has been designed with a pole radius of 53 cm and a strong central magnetic field of 55.3 kG. The extraction system is based on a regenerator followed by a passive magnetic channel which contains a series of deflecting and focusing elements, and the properties of this system are described. The extraction efficiency for different initial conditions and the resultant properties of the extracted beam have been calculated using the Z^4 Orbit Code which treats nonlinear effects realistically. A central region electrode configuration with a closed ion source plus puller has been designed and orbit calculations have been performed to determine the orbit behavior in the central region. An ion

source experiment has been carried out to determine whether sufficient ion current can be produced with this type of central region geometry. A transfer matrix program has been developed and used to perform the capture time calculations, and to determine conditions for optimizing the capture efficiency. Possible RF frequency programs have also been studied that would avoid a loss of particles by maintaining a constant bucket area.

To my wife
JingLing Wang

ACKNOWLEDGMENTS

I would like to thank the staff and faculty of the National Superconducting Cyclotron Laboratory for their support of my education and the completion of this dissertation. To my advisor, Dr. Morton Gordon, I owe my deepest gratitude for his guidance, encouragement and supervision during my graduate career, without his help, this thesis would be all blank pages. His patience, depth of vision, sense of humor, and understanding have been greatly appreciated and are acknowledged. My special thanks go to Dr. Henry Blosser for his continuous advice and comments on my research work. His guidance and deep knowledge of this field have made the completion of this work possible. I want to specially thank Dr. Felix Marti for his advice, help and numerous discussions about my research and thesis work. His patience and friendship helped me pass many difficult times. In addition, I wish to thank Dr. Thomas Kuo for his advice and numerous discussions about the ion source and his friendship. I would also like to thank Dr. Timothy Antaya, Dave Johnson, Jame Bailey, Dr. Lee Harwood and Dr. Bruce Milton for their help in my graduate career. I am grateful to Drs. M. Abolins, H. Blosser, T. Kaplan, J. Nolen and B. Pope for their service on my Ph. D guidance committee.

I want to thank my parents Wang, YuZhen and Wu, FuQuan for helping me reach this point and for the special role they have played in my life.

Finally, I want to thank the person who supported and stood by me in all 5 years of my graduate study, and give me the necessary love and encouragement to make it through: my wife JingLing Wang.

I am also grateful to Michigan State University and the National Science Foundation for the financial support during my graduate study.

TABLE OF CONTENTS

	Page
LIST OF TABLES.....	ix
LIST OF FIGURES.....	x
Chapter 1 - Introduction.....	1
1.1 Background.....	1
1.2 Features of Design.....	5
Chapter 2 - Magnet Design and Magnetic Field.....	10
2.1 Introduction.....	10
2.2 Magnet Design and Field Properties.....	11
2.3 Magnet Shimming in the Central Region.....	21
Chapter 3 - Extraction System Design.....	25
3.1 Introduction.....	25
3.2 Orbit Calculation Program.....	29
3.3 Regenerator Design.....	32
3.4 Magnetic Channel Design.....	43
3.5 Accelerated Orbit Calculations.....	48
3.5.1 Radial Motion.....	48
3.5.2 Combined Radial and Vertical Motion..	50
3.6 Summary and Conclusions.....	54
Chapter 4 - Ion Source Experiment.....	61
4.1 Introduction.....	61

4.2	Ion Source Experiment Setup.....	63
4.3	Ion Source Experiment Result.....	63
4.4	Result Analysis and Conclusions.....	71
Chapter 5	- Central Region Design.....	83
5.1	Introduction.....	83
5.2	Central Region Design.....	84
5.3	Field and Orbit Calculations.....	95
5.4	Orbit Properties and Discussions.....	97
5.5	Capture Time Calculations.....	107
5.5.1	Transfer Matrix Program.....	108
5.5.2	Capture Time Calculation Results.....	110
Chapter 6	- RF Frequency Program.....	118
6.1	Introduction.....	118
6.2	Fixed Dee Voltage.....	123
6.3	Fixed Energy Gain per Turn.....	124
6.4	Acceleration Time.....	129
Chapter 7	- Summary and Conclusions.....	134
Appendices	139
A	- Geometry and Position of the Regenerator...	139
B	- Geometry and Position of the magnetic Channel Elements.....	143
C	- Transfer Matrix Program Equations.....	147
LIST OF REFERENCES	150

LIST OF TABLES

TABLE		PAGE
2-1	Computed Median Plane Magnetic Field and Field Index vs. Radius.....	15
2-2	Compensating Rings' Geometric Parameters.....	23
3-1	The Summary of the Extraction Orbit Calculation Results.....	53
3-2	The Calculation Results of the Extraction Orbit Properties at the Exit of the Channel.....	56
4-1	Geometry Parameters in Ion Source Experiment.....	67
5-1	Capture Time and Capture Efficiency Results.....	114
6-1	Required Parameters of the RF Systems.....	133

LIST OF FIGURES

FIGURE		PAGE
1-1	The schematic diagram of a stand-alone proton cancer therapy facility using the 250 MeV superconducting synchrocyclotron.....	6
1-2	Plan view of the 250 MeV superconducting synchrocyclotron.....	7
1-3	Vertical cross section view of the 250 MeV superconducting synchrocyclotron.....	8
2-1	Magnet geometry for the 250 MeV superconducting synchrocyclotron.....	12
2-2	Plots of the magnetic field B and the field index n vs. radius in the median plane.....	14
2-3	Plot of the resultant fringe magnetic field distribution in the median plane.....	17
2-4	Plot of the resultant fringe magnetic field distribution along the vertical z-axis in the machine center.....	18
2-5	Plots of the v_r and $2v_z$ of the 250 MeV superconducting synchrocyclotron field vs. R.....	19

2-6	Plot of the proton revolution frequency vs. energy in the 250 MeV superconducting synchrocyclotron magnetic field.....	20
2-7	Cross section of the compensating rings situated on the face of the magnet pole and the magnetic fields produced by compensating rings, ion source hole and both of them together.....	22
2-8	Plots of K values and the magnetic field index n vs. radius in the central region.....	24
3-1	Plots of v_r and $2v_z$ vs. energy both with and without regenerator and the magnetic channel.....	28
3-2	Layout of the extraction system.....	30
3-3	Theoretical regenerator field B and its gradient $\frac{dB}{dr}$ vs. radius.....	35
3-4	The radial profile and the plan view of the regenerator, and its resultant magnetic field B as well as field index n.....	36
3-5	Radial phase plots showing the radial motion of two different orbits at 255.2 MeV and the stability boundaries at 255.0 and 255.2 MeV.....	37
3-6	Plots of r vs. θ for the last five turns of an typical extracted orbit.....	39

3-7	Plots of Height Δz vs. turn number for a group orbits having an initial height $\Delta z_0 = 0.1$ in. and energies of 252.0 and 252.5 MeV.....	41
3-8	Plots of Height Δz vs. turn number for a group orbits having an initial height $\Delta z_0 = 0.1$ in. and energies of 253.0 and 253.5 MeV.....	42
3-9	Cross section of the deflecting magnet M1 with projecting wings and its resultant magnetic field and field gradient.....	46
3-10	Cross section of the radial focusing magnet M3 with projecting wings and its resultant magnetic field and field gradient.....	47
3-11	Radial phase plots at $E=254.5$ MeV and $\theta=180^\circ$ showing four invariant curves for initial radial amplitudes of 1.27, 2.54, 3.81 and 5.08 mm.....	49
3-12	Radial phase plot at the entrance of the magnetic channel ($\theta=100^\circ$) showing resultant distribution for median plane orbits.....	51
3-13	Initial (z, p_z) values at $E=254.5$ MeV and $\theta=180^\circ$ used for accelerated orbits.....	52
3-14	Phase plot at the entrance of the magnetic channel ($\theta=100^\circ$) showing the $(z, p_z/p_0)$ values for all the extracted orbits.....	55

3-15	Radial and vertical envelopes for all of the successfully extracted orbits as they traverse the magnetic channel.....	58
3-16	Radial and vertical phase plots at the exit of the magnetic channel ($\theta=210^\circ$) showing the distribution of successfully extracted orbits...	59
3-17	Distribution of final energies of the proton orbits with radial and vertical amplitudes smaller than 3 mm.....	60
4-1	Schematic diagram of the ion source experiment setup.....	64
4-2	Plot of the cross section of the central region with puller and supporting system in place for the ion source experiment.....	65
4-3	The cross section views of the source chimney used in the tests.....	66
4-4	Plot of ion current I_{ext} vs. extraction voltage V_{ext} in test #1.....	68
4-5	Plot of ion current I_{ext} vs. source current I_s in test #1.....	69
4-6	Plot of ion current I_{ext} vs. gas flow Q in test #1.....	70

4-7	Plot of ion current I_{ext} vs. extraction voltage V_{ext} in test #2.....	72
4-8	Plot of ion current I_{ext} vs. gas flow Q in test #2.....	73
4-9	The potential contour map of electric field between chimney and puller in test #1.....	75
4-10	The potential contour map of electric field between chimney and puller in test #2.....	76
4-11	Plots of electric field distributions along the Y-axis in test #1 and #2 with different extraction voltage.....	77
4-12	Plots of I_{ext} in test #1 and $2I_{ext}$ in test #2 vs. the extraction voltage V_{ext}	79
4-13	Plots of I_{ext} in test #1 and $2I_{ext}$ in test #2 vs. the gas flow.....	81
5-1	Central region electrodes in the median plane and the equipotentials of the resultant electric field.....	86
5-2	Plot of cross sections of the acceleration gaps with the symmetric and unsymmetric dee and dummy-dee vertical apertures.....	88

5-3	Plots of z and p_z vs. Turns for the starting condition $(z, p_z) = (0.1, 0.0)$ in. at the top and for $(z, p_z) = (0.0, 0.01)$ in. at the bottom with protons starting at $\tau_0 = 200^\circ$ at the source with symmetric acceleration gap.....	89
5-4	Plots of z and p_z vs. Turns for the starting condition $(z, p_z) = (0.1, 0.0)$ in. at the top and for $(z, p_z) = (0.0, 0.01)$ in. at the bottom with protons starting at $\tau_0 = 200^\circ$ at the source with unsymmetric acceleration gap.....	90
5-5	Plots of the source chimney and puller in the median plane and equipotentials of the electric fields in the source-to-puller region using a gap of 2 mm and a 4.0 by 0.5 mm ² rectangular slit.....	92
5-6	Plots of the source chimney and puller in the median plane and equipotentials of the electric fields in the source-to-puller region using a gap of 1.5 mm, and a 0.75 mm diameter circular slit with a opening angle of 120°.....	93

5-7	Plot of the electric field distribution near the center of the chimney slit for two different cases shown in Figs. 5-3 and 5-4.....	94
5-8	Source chimney and puller electrodes, and the median plane equipotentials for the small electric field with eight plotted proton orbits with starting time $\tau_0 = 200^\circ$ to 265°	98
5-9	Central region electrodes and the median plane and equipotentials for the large electric field with eight plotted proton orbits with starting time $\tau_0 = 200^\circ$ to 265°	99
5-10	Plots of x vs. p_x for protons starting at $\tau_0 = 200^\circ$ to 260° for the first 20 turns.....	101
5-11	Plot of average phase ϕ vs. Turns for protons starting at $\tau_0 = 200^\circ$ to 265° for the first 20 turns.....	102
5-12	Plots of z and p_z vs. Turns for the starting condition $(z, p_z) = (0.1, 0.0)$ in. at the top and for $(z, p_z) = (0.0, 0.01)$ in. at the bottom with protons starting at $\tau_0 = 200^\circ$ at the source.....	104

5-13	Plots of z and p_z vs. Turns for the starting condition $(z, p_z) = (0.1, 0.0)$ in. at the top and for $(z, p_z) = (0.0, 0.01)$ in. at the bottom with protons starting at $\tau_0 = 230^\circ$ at the source.....	105
5-14	Plots of z and p_z vs. Turns for the starting condition $(z, p_z) = (0.1, 0.0)$ in. at the top and for $(z, p_z) = (0.0, 0.01)$ in. at the bottom with protons starting at $\tau_0 = 260^\circ$ at the source.....	106
5-15	Plots of the distributions of T vs. proton starting time τ_0 with initial $(-\frac{df}{dt})_i$ of 35.51, 56.62 and 71.02 MHz/ms.....	112
5-16	Plots of the distributions of T vs. proton starting time τ_0 with initial $(-\frac{df}{dt})_i$ of 106.53 and 142.04 MHz/ms.....	113
5-17	Plot of average capture time Δt_{av} vs. initial $(-\frac{df}{dt})_i$ together with the corresponding value of $\cos\phi_{s1}$	116
6-1	Three phase space three separatrices corresponding to $\cos\phi_s$ of 0.05, 0.1 and 0.3.....	120

6-2	Plot of the normalized bucket area A vs. the synchronous phase $\cos\phi_s$	121
6-3	Plot of the resultant synchronous phase $\cos\phi_s$ vs. energy with a fixed dee voltage $V_d = 20$ kV...	125
6-4	Plot of the required frequency time derivative $(-\frac{df}{dt})$ vs. energy with a fixed dee voltage $V_d = 20$ kV.....	126
6-5	Plot of $A' = (\frac{A}{(\cos\phi_s)^{1/2}})$ vs. synchronous phase $\cos\phi_s$	128
6-6	Plot of the resultant $\cos\phi_s$ vs. energy with a fixed energy gain of 10 keV/turn at large energies.....	130
6-7	Plot of the required frequency time derivative $(-\frac{df}{dt})$ vs. energy with a fixed energy gain of 10 keV/turn at large energies.....	131
6-8	Plot of the required dee voltage of RF system vs. energy with a fixed energy gain of 10 KeV/turn at large energies.....	132
A-1	The radial profile of the regenerator above the median plane showing its 5 parts.....	141

A-2	Coordinates required to define the iron rings in the each regenerator part.....	142
B-1	Coordinates required to define the rectangular iron bars in the magnetic channel element.....	146

Chapter 1

Introduction

1.1 Background

Cancer therapy using protons was first proposed by Robert Wilson [1] in 1946 and the first work on the biological and medical application of proton beams was done by J. H. Lawrence and C. A. Tobias [2] at Berkeley in 1948. As reported by B. Gottschalk [3], the advantages of using protons in cancer therapy rest on two physical characteristics. First, the dose delivered by a proton penetrating tissue rises as the proton slows down, reaching about three to four times the entrance dose near the stopping point (Bragg Peak), and is zero beyond the stopping point. Protons in a monoenergetic beam have very nearly the same range and therefore deliver maximum dose at the same depth. The high localizability of protons in a monoenergetic beam means that side effects are smaller than with neutrons. Secondly, being heavy, protons do not deviate very much from a straight line as they penetrate into the tissue and come to rest. Their physical peak-plateau dose ratio is also higher than that of any other beam.

There have been many years of successful clinical applications of proton beams in cancer therapy at different institutions around the world and different kinds of accelerators have been used to provide the proton beams for cancer therapy, such as cyclotrons, synchrocyclotrons and synchrotrons.

Initial clinical work at Berkeley in 1954 used 340 MeV protons and from 1957 to 1988 work at the 184" cyclotron has made use of 910 MeV helium ions. (The biological effects of helium ions are similar to those of protons and the physical dose distribution is even sharper than for protons [3].) Many patients have received treatment with success. Another early work in this field was done starting in 1955 by the Uppsala group under B. Larsson and L. Leksell [4] using the 185 MeV synchrocyclotron of the Gustav Werner Institute. Since 1959, a 160 MeV synchrocyclotron has been used at the Harvard University Cyclotron Laboratory [5, 6] for cancer therapy and some 3400 patients have been treated to date. There is also an extensive program in the USSR using a synchrotron and synchrocyclotrons to provide the proton beam for cancer therapy at three centers: a 1000 MeV proton beam from the synchrocyclotron in Gatchina, a 200 MeV proton beam from the Dubna 680 MeV synchrocyclotron and a proton beam of 70 - 200 MeV, in 5 MeV steps, from the 7.2 GeV synchrotron ring at the ITEP [3, 7] in Moscow.

In the United States, considerable attention has been recently directed toward the development of accelerator systems optimized for radiation therapy with protons. The most recent development is a cancer therapy facility at Loma Linda University Medical Center [8, 9]. A 250 MeV proton synchrotron has been used to provide 70 - 250 MeV protons with a beam intensity goal of 1.2×10^{11} protons per pulse in a two second cycle time. The current beam intensity achieved is about 4.0×10^{10} protons per pulse in a four second cycle time. There are a total of four quadrants around the accelerator circumference, each composed of a 90° bending and a straight section, and the central orbit is approximately 19 feet in diameter. The beam is injected with an energy of 2.0 MeV and then accelerated to the desired energy by a radiofrequency system. After acceleration, the beam is extracted and then transported through a beam switchyard to different treatment rooms.

Of all the accelerators used in proton cancer therapy facilities, the synchrocyclotron is the least demanding machine. It uses an internal ion source to provide a proton beam directly to the accelerator; no injector is needed. A RF system with frequency modulation is used to avoid the resonance limitation due to a fixed frequency and to allow acceleration to higher energies. A simple symmetric weak

focusing magnetic field is used to contain the protons in circular orbits and provide adequate radial and vertical focusing force. Cyclotrons can accelerate many more particles than synchrocyclotrons per unit time, but the beam intensity from a synchrocyclotron is entirely adequate for cancer therapy.

All the synchrocyclotrons used in present proton therapy programs are older, massive room temperature machines which are located in physics laboratories and are overall poorly matched to a hospital environment. H. Blosser has asserted [10] that such a machine would be inordinately costly to reproduce in present conditions. If the synchrocyclotron is redesigned as a superconducting high magnetic field device, the mass and cost are greatly reduced and an overall system with many appealing features results. The advantages of adapting the superconducting cyclotron to medical use have been demonstrated by the construction and completion of the first superconducting cyclotron for neutron therapy - Harper Cyclotron by H. Blosser [11,12,29,43,44] at MSU from 1984 to 1990. A 250 MeV superconducting synchrocyclotron has been proposed at the National Superconducting Cyclotron Laboratory. The conceptual design of the magnet, extraction system and central region and the orbit dynamics in this machine are described in this thesis.

1.2 Features of the Design

As reported by H. Blosser, et. al. [11], design studies of the 250 MeV superconducting synchrocyclotron magnet have been carried out at MSU based on the pillbox magnet concepts used in earlier MSU isochronous cyclotrons [12]. The magnet of such a cyclotron weighs about 60 tons, and it is still compatible with direct gantry mounting. A possible system arrangement is shown schematically in Fig. 1-1. Figures 1-2 and 1-3, respectively, show the plan view and the vertical cross section view of the proposed 250 MeV superconducting synchrocyclotron.

The proton energy of 250 MeV is chosen because of the range of protons in tissue. It is sufficient for irradiation of even obese patients from many directions and corresponds to the range in tissue of 37 cm. The beam current is closely related to the treatment time desired for patients. A few nanoamps are marginally adequate and tens of nanoamps are comfortable for even the largest tumors. The performance and design parameters of the 250 MeV superconducting synchrocyclotron are:

Particle	Protons
Energy	250 MeV
Beam current	20 - 100 nA
Central Magnetic Field	55.3 kG
Magnet Pole Radius	21.0 in.

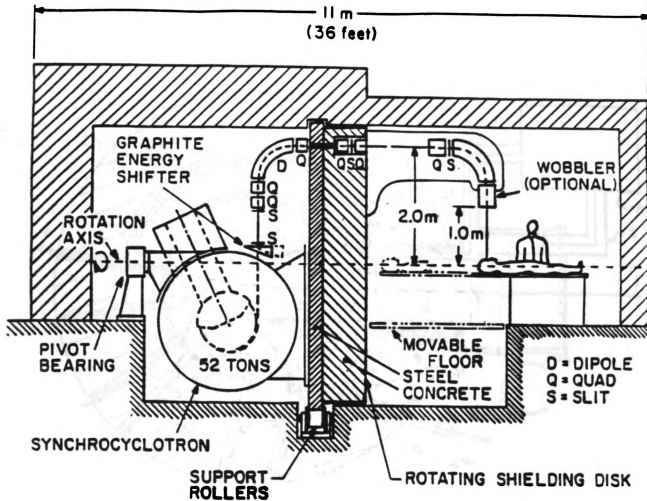


Fig. 1-1 -- The schematic diagram of a possible stand-alone proton cancer therapy facility using the 250 MeV superconducting synchrocyclotron with the rotating gantry arrangement.

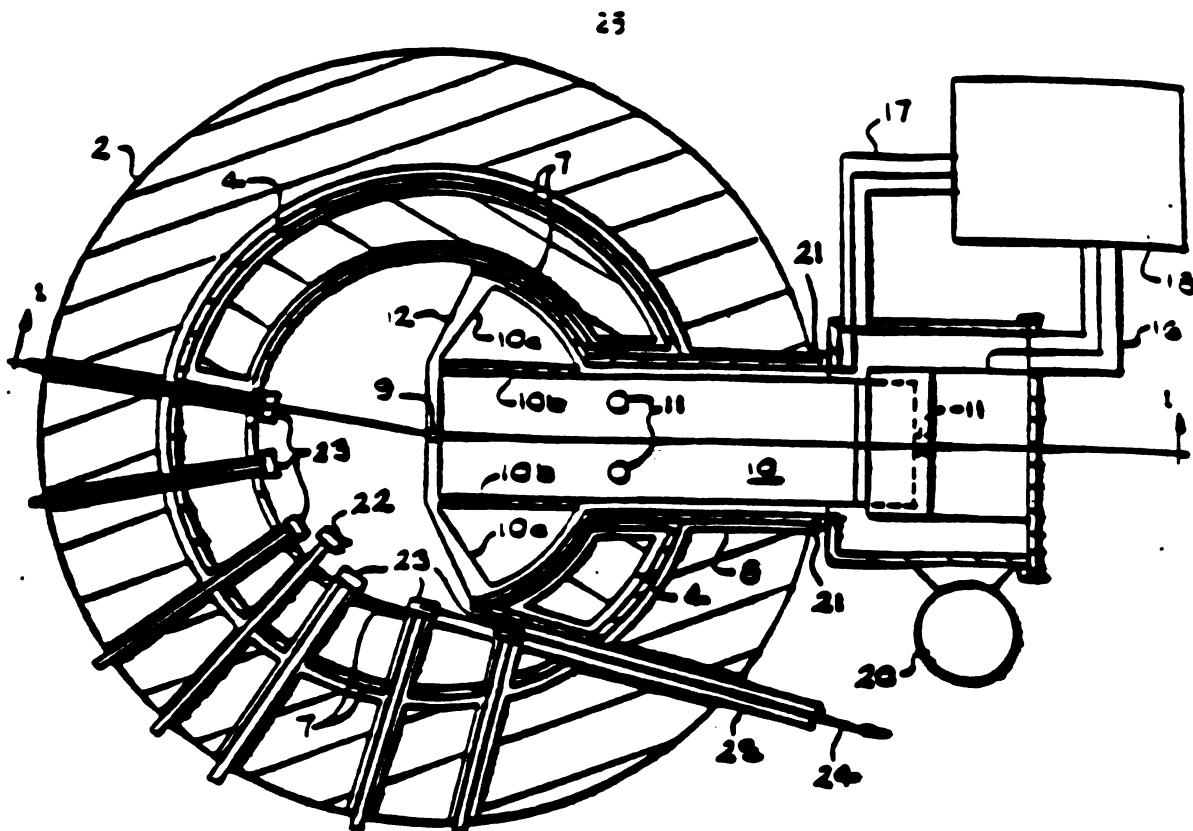


Fig. 1-2 -- Plan view of the 250 MeV superconducting synchrocyclotron. Identified features include: 2 - the outer yoke of magnet. 10 - the cyclotron stems. 22 - the regenerator of the extraction system. 23 - focusing channel for the extracted beam. 24 - path of the external beam leaving the synchrocyclotron.

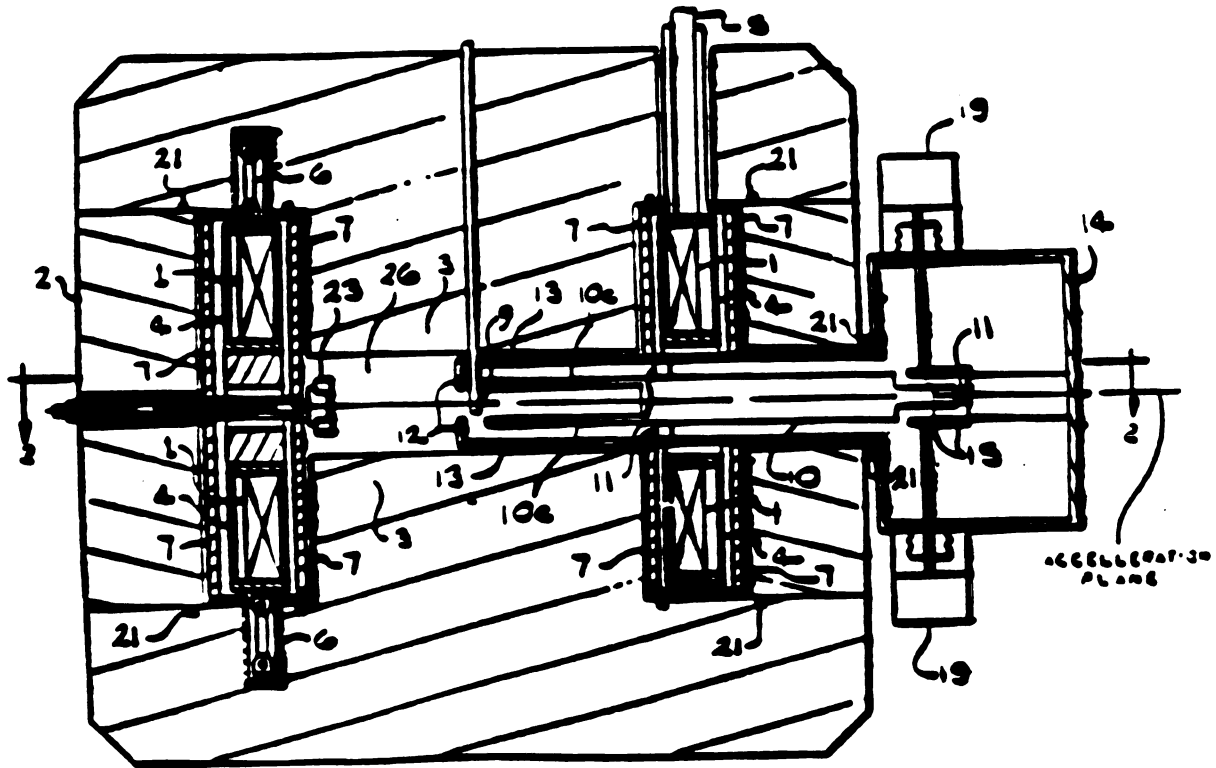


Fig. 1-3 -- Vertical cross section view of the 250 MeV superconducting synchrocyclotron. Reference number include:
 1 - the superconducting main coil. 2 - the outer yoke of the magnet. 4 - the outer wall of the liquid helium vessel. 9 - a closed proton ion source.

Range of RF Frequency	84.27 - 61.75 MHz
Modulation Frequency	1 kHz
RF voltage	20 kV
Electric Gap	2 mm

Because of its strong magnetic field produced by the superconducting magnet, the 250 MeV superconducting synchrocyclotron has many advantages and appealing features. It is very compact and light - the radius of the outer yoke of the magnet is only 52 inches and the approximate weight of the accelerator plus the counterweight and the supporting system is about 150 tons. It could provide high proton beam current of 20 - 100 nA. It is specifically designed to fit a hospital environment with a reasonable cost. However, three main technical issues must be addressed in designing such a machine. First, its strong magnetic field will lead to smaller orbit turn separations at larger radii and hence provide difficulties in designing the extraction system. Secondly, the feasibility of designing a set of central electrodes with a closed ion source within the limited space in the central region needs to be studied. Finally the high RF frequency 84.27 MHz - 61.75 MHz, the moderately large frequency range and the desired high repetition rate will require a special effort to design a suitable RF system.

Chapter 2

Magnet Design and Magnetic Field

2.1 Introduction

The 250 MeV superconducting synchrocyclotron has a strong magnetic field that takes advantage of the high state of development of superconducting magnet technology to reduce the size and weight of the machine. The base magnetic field is axially symmetric and decreases with radius to provide adequate radial and vertical focusing forces. The fringe magnetic field outside the machine must be limited within an acceptable range, since this machine is specifically designed for medical work. The magnet design also has to provide adequate space for the internal ion source, electrodes in the central region, dee structure and the extraction system. Finally, the magnetic field in the central region must be tailored to optimize the capture efficiency. The basic design of the magnet and coils was carried out by H. Blosser and others before this thesis work began.

The POISSON program was used to carry out two-dimensional relaxation calculations and hence to determine the axially symmetric magnetic field in the median plane for

a given magnet configuration. The equilibrium orbit code [13] was then used to calculate the basic orbit properties in the given magnetic field. The magnet design process required the magnetic field computation plus the evaluation of the orbit characteristics for each tentative magnet configuration in order to systematically improve the design parameters.

2.2 Magnet Design and Magnetic Field Properties

Figure 2-1 shows the proposed magnet configuration for the 250 MeV superconducting synchrocyclotron. The magnet is symmetric about the $r=0$ axis and the $z=0$ plane except for the extraction system. The magnetic field index n , and the radial and vertical orbit oscillation frequencies are given by:

$$n = - \frac{r}{B} \left(\frac{dB}{dr} \right) ,$$

$$v_r = (1-n)^{1/2} ,$$

and
$$v_z = n^{1/2} .$$

The superconducting magnet coil has a rectangular cross section and carries a current density of 5200 amps per square centimeter. The cross section of the superconducting coil is 294 square centimeters. The main region of the magnet configuration is occupied by conventional iron. The

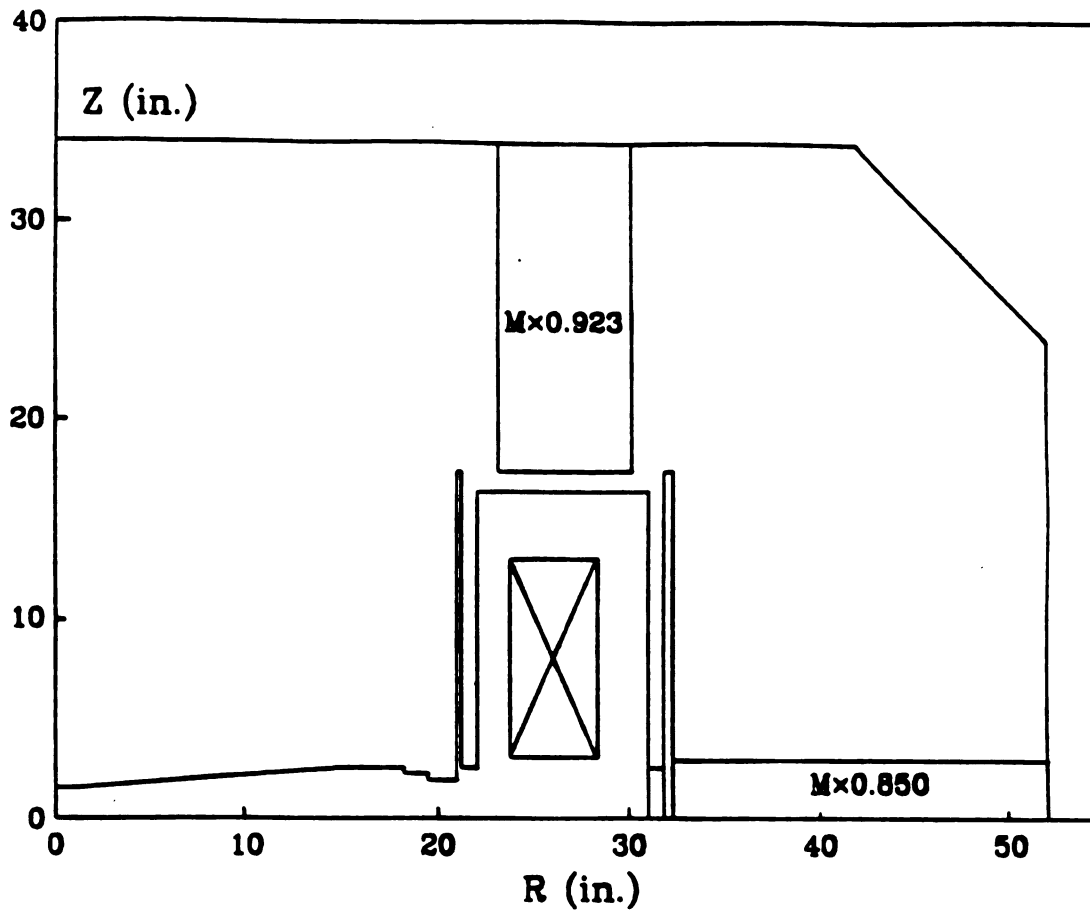


Fig. 2-1 -- Magnet geometry for the 250 MeV superconducting synchrocyclotron. The current density in the superconducting coil is 5200 amps per square centimeter and the coil cross section is 294 square centimeters.

dee stem region and coil support regions are assumed to be partially occupied by iron to the fractional degree indicated by the multiplier beside the label "M" in Figure 2-1.

Figure 2-2 shows the resultant magnetic field and field index in the median plane. It also shows the pole surface of the magnet configuration except for the extraction elements described in the next chapter. As can be seen, the small magnet gap of 3.0 in. is used in the center in order to increase the central magnetic field. The value of the field index n varies smoothly from zero in the center to about 0.1 at large radii. Then as the field falls off rapidly near the pole edge, the value of n rises sharply. The $n = 0.2$ point represents an approximate limit for acceleration and hence defines the approximate maximum energy. At this value of n , the $v_r = 2v_z$ coupling resonance occurs and causes loss of the beam through vertical blow-up. The magnet gap near the edge was carefully contoured to push the $n = 0.2$ point as far out as possible in order to maximize the final energy. Table 2-1 gives the computed magnetic field B and the field index n as a function of radius for the magnet configuration illustrated in Fig. 2-1.

Since the 250 MeV superconducting synchrocyclotron is specially designed for a hospital environment, the fringe

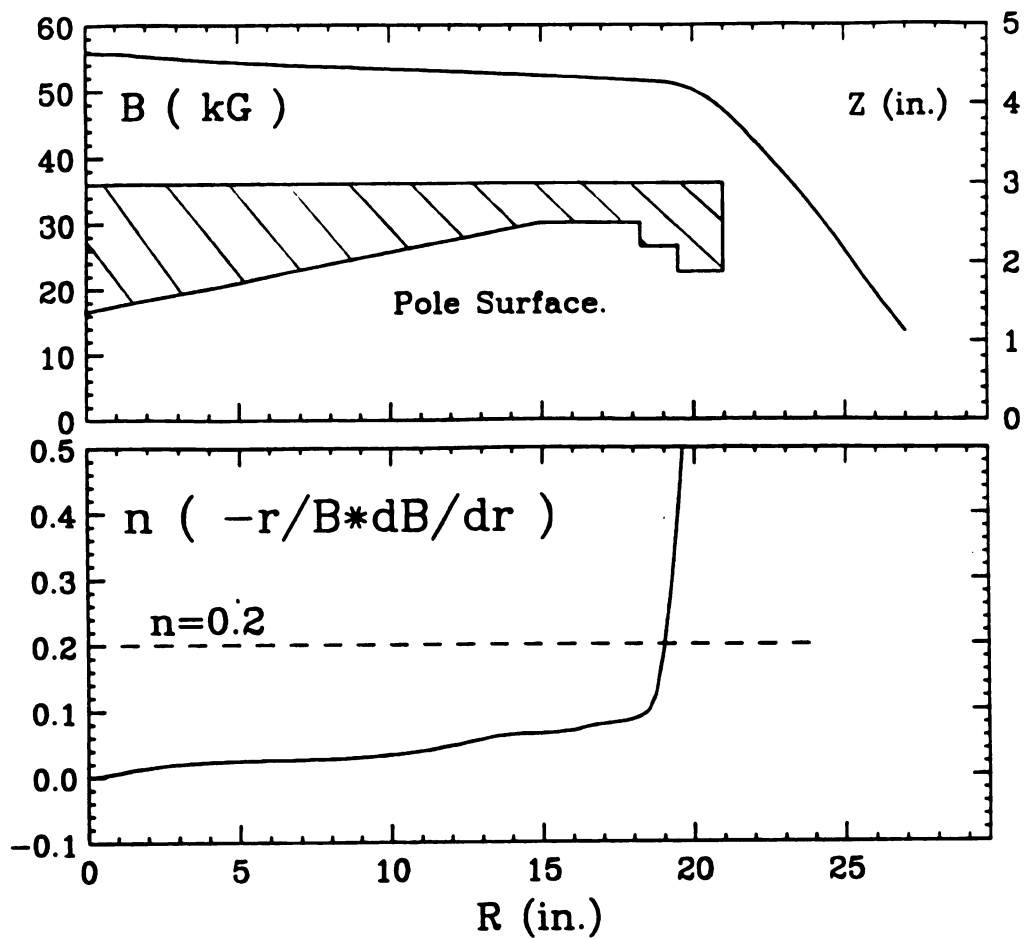


Fig. 2-2 -- Plots of the magnetic field B (kG) and the field index $n = \left(-\frac{r}{B} \frac{dB}{dr}\right)$ vs. radius in the median plane. Also shown in the plot is the magnet pole shape of the 250 MeV superconducting synchrocyclotron.

Table 2-1 Computed median plane magnetic field in kilogauss and the field index n vs. radius in inches for the magnet configuration illustrated in Fig. 2-1.

Radius	Magnetic Field	Field Index
0.00000	55.76844	0.00000
0.50000	55.72196	0.00175
1.00000	55.59104	0.00532
1.50000	55.42340	0.00967
2.00000	55.23993	0.01325
2.50000	55.05836	0.01641
3.00000	54.88191	0.01844
3.50000	54.71828	0.02044
4.00000	54.56526	0.02140
4.50000	54.42445	0.02257
5.00000	54.29353	0.02309
5.50000	54.17251	0.02382
6.00000	54.05994	0.02417
6.50000	53.95396	0.02473
7.00000	53.85477	0.02509
7.50000	53.76028	0.02573
8.00000	53.67034	0.02633
8.50000	53.58306	0.02722
9.00000	53.49809	0.02852
9.50000	53.41361	0.02992
10.00000	53.32915	0.03206
10.50000	53.24273	0.03439
11.00000	53.15395	0.03773
11.50000	53.06131	0.04121
12.00000	52.96288	0.04588
12.50000	52.85963	0.05024
13.00000	52.74966	0.05505
13.50000	52.63571	0.05977
14.00000	52.51820	0.06277
14.50000	52.40087	0.06440
15.00000	52.28598	0.06477
15.50000	52.17461	0.06597
16.00000	52.06357	0.06833
16.50000	51.95006	0.07433
17.00000	51.83169	0.07787
17.50000	51.71257	0.08097
18.00000	51.59169	0.08583
18.50000	51.46432	0.09832
19.00000	51.29268	0.18837
19.50000	50.91124	0.42219
20.00000	50.14992	0.80654

magnetic field outside the machine has to be limited within a certain range. Using a larger magnet yoke would certainly reduce the fringe field, but at the same time, it would increase the size and weight of the magnet as well. As is shown in Fig. 2-1, the half height of 34 inches and radius of 52 inches for the outer yoke have been used to limit the fringe field. The corner of the outer yoke has been cut off to reduce the size and weight of the magnet without significantly affecting the magnetic field in the region of acceleration. The resultant fringe fields in the median plane and along the $r=0$ axis are shown in Figs. 2-3 and 2-4, respectively.

The equilibrium orbit code was used to calculate the basic orbit properties in the given magnetic field. Figure 2-5 shows the plots of the resultant focusing frequencies ν_r and $2\nu_z$ vs. radius. The $2\nu_z$ values rise with increasing radius while the ν_r values fall. These values cross the $\nu_r = 2\nu_z$ ($n=0.2$) resonance at 19.1 in. The proton revolution frequency vs. proton energy is shown in Fig. 2-6. The frequency value falls almost linearly from 84.27 MHz in the center to 61.75 MHz at maximum proton energy. The range of frequency therefore is about 22.5 MHz.

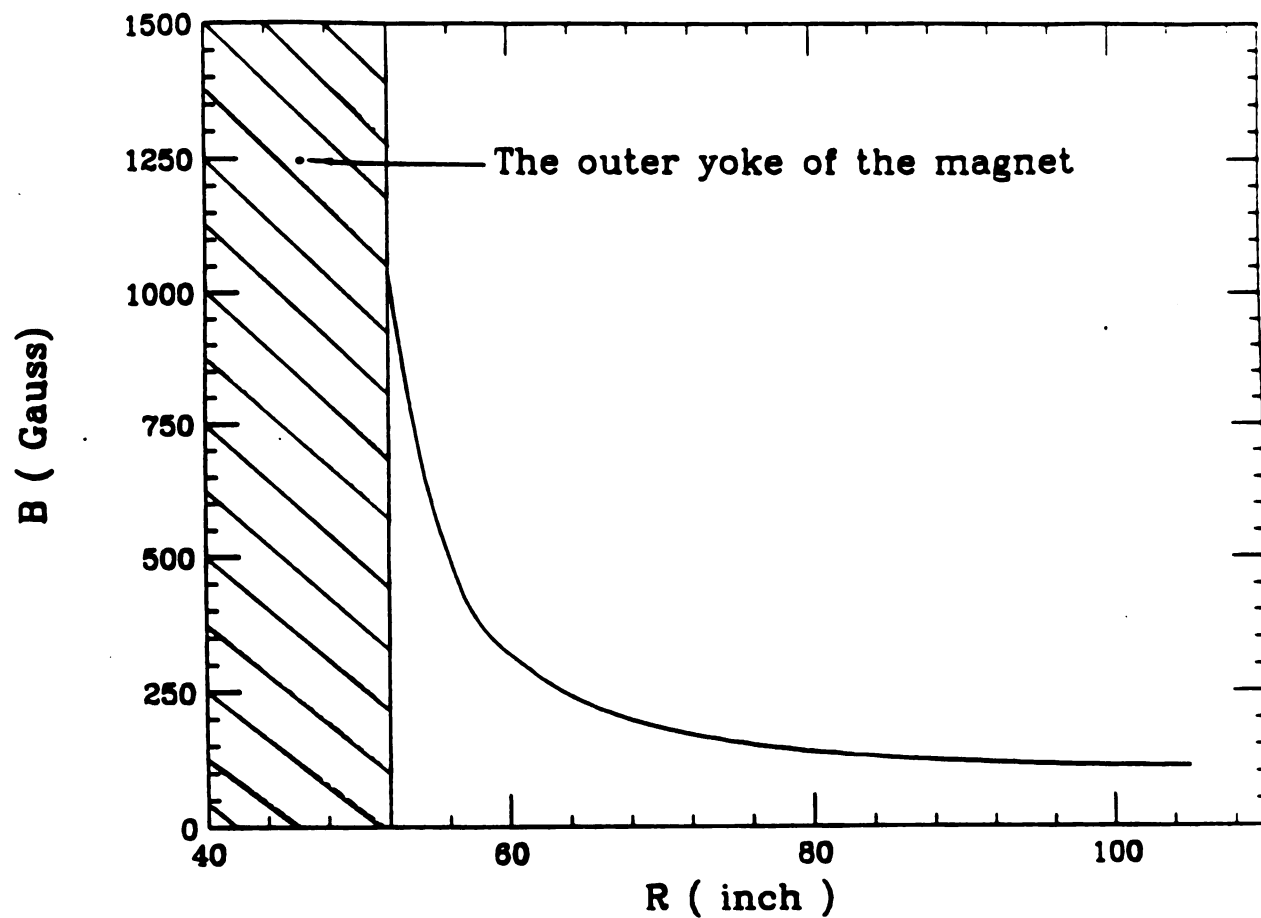


Fig. 2-3 -- Plot of the resultant fringe magnetic field distribution in the median plane.

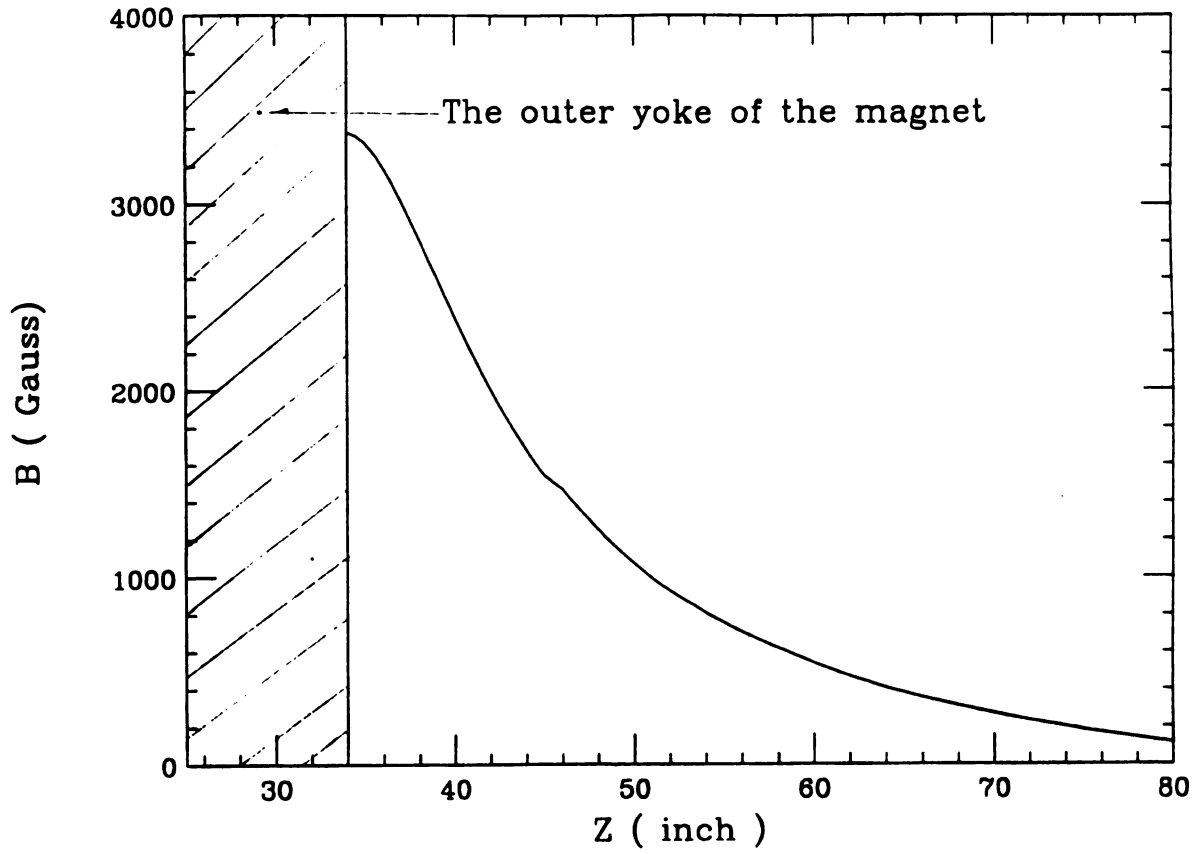


Fig. 2-4 -- Plot of the resultant fringe magnetic field distribution along the vertical z axis in the machine center.

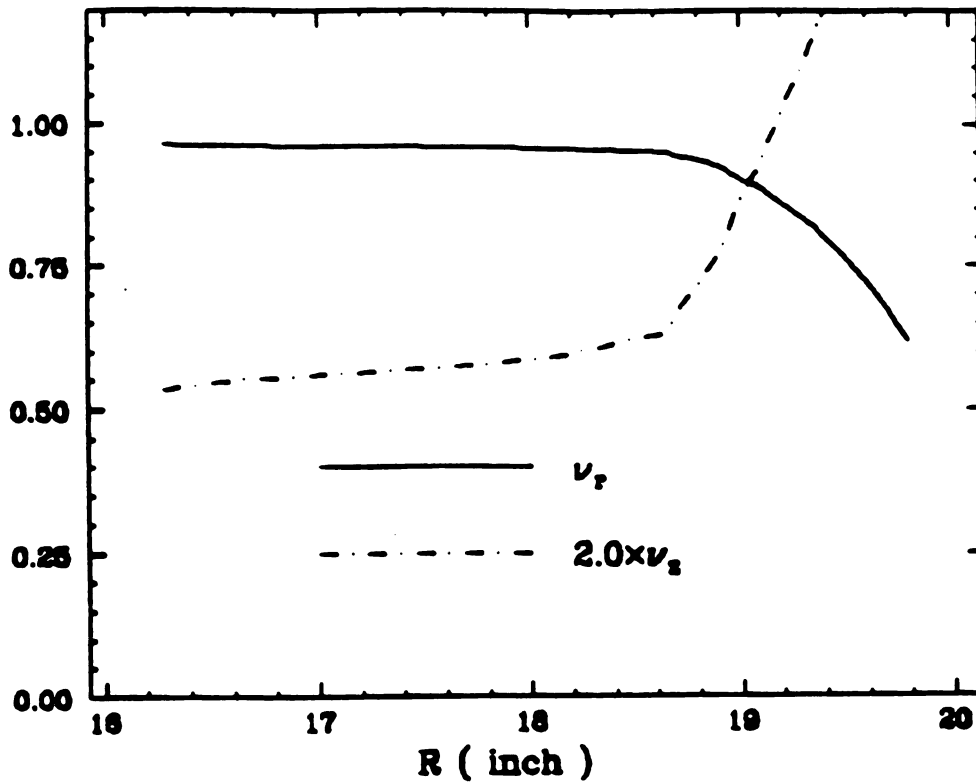


Fig. 2-5 -- Plots of the resultant ν_r and $2\nu_z$ of the 250 MeV superconducting synchrocyclotron magnetic field. The $2\nu_z$ values rise with increasing radius while the ν_r values fall. These values cross at the $\nu_r = 2\nu_z$ ($n=0.2$) resonance at 19.1 in.

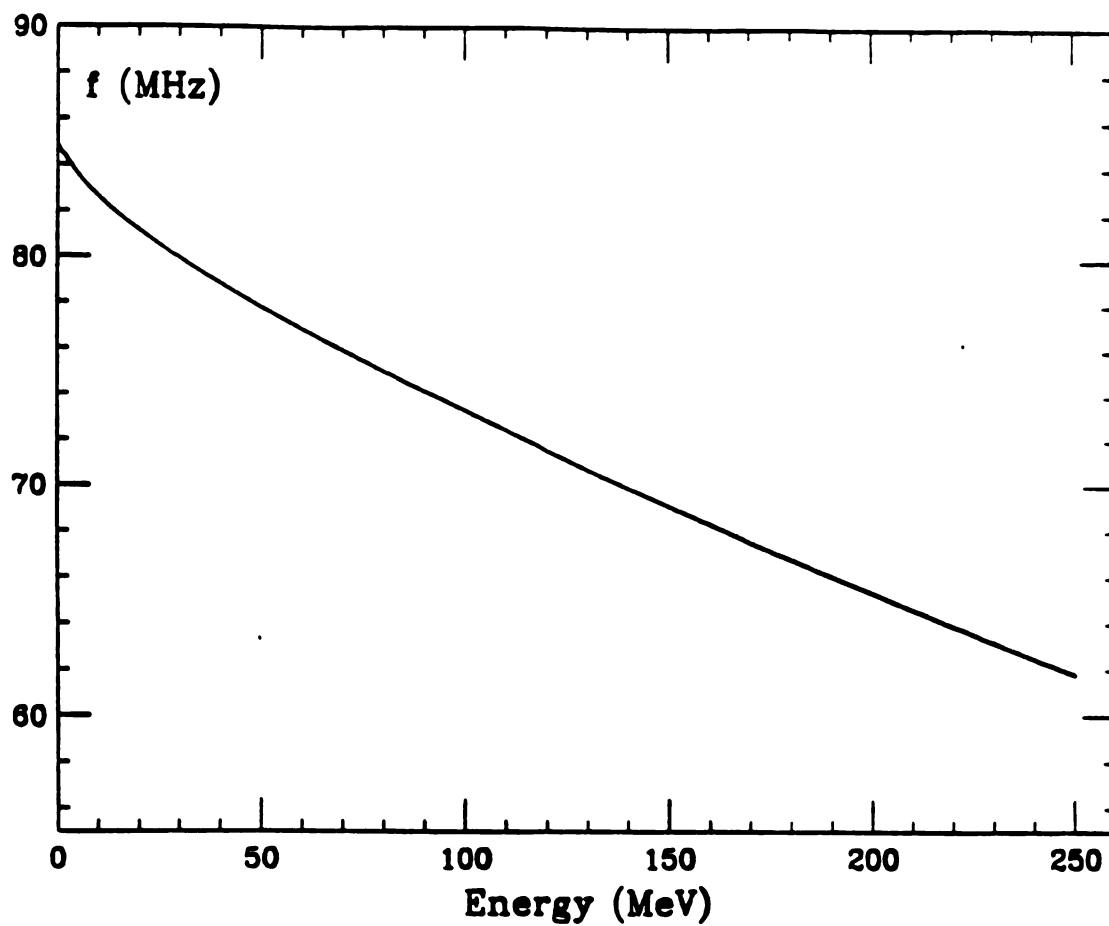


Fig. 2-6 -- Plot of the proton revolution frequency vs. energy in the 250 MeV superconducting synchrocyclotron magnetic field. The frequency range is about 22.5 MHz.

2.3 Magnet Shimming in the Central Region

The axial insertion of the ion source requires a hole through the magnetic poles in the center, which changes the magnetic field shape in the central region. As a result of this change, the field increases initially with radius, reaches a maximum value, and then falls off smoothly with radius. Thus, the field index n is initially negative so that vertical defocusing occurs at small radii. The effect becomes stronger if a larger ion source hole is used.

As reported by E. Braunersreuther, et. al. [14], this defocusing can be minimized by careful shimming. We use the smallest possible hole diameter (0.8 in.) and introduce an intricate set of compensating circular shims. Furthermore, the calculations described in chapter 5 indicate that the capture time depends strongly on the magnetic field shape in the center. A high value of

$$K = - \frac{E}{\omega} \left(\frac{d\omega}{dE} \right) = 1 + \frac{n}{B^2(1-n)}$$

in the center is desired to increase the capture time and the capture efficiency. This can also be achieved to some extent by changing the configuration of the compensating rings. A set of compensating rings was designed and used to meet all these requirements. The cross section of the magnet pole with the ion source hole and compensating rings is shown in Fig. 2-7. The diameter of the central hole for the

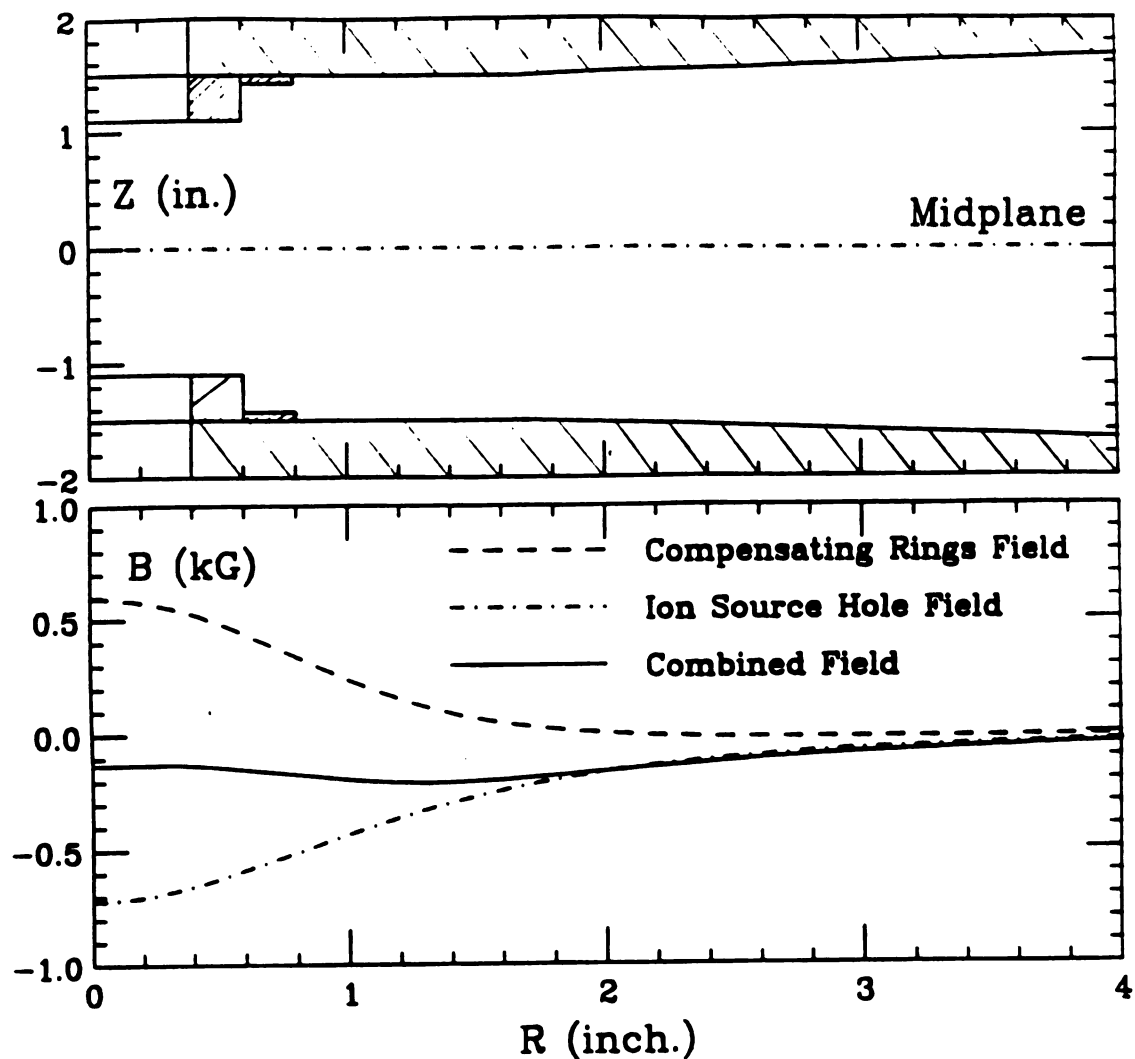


Fig. 2-7 -- At top, cross section of the compensating rings situated on the face of the magnet pole. The diameter of the central hole for the ion source is 0.8 inches. At bottom, plots of the magnetic field produced by the compensating rings, the magnetic field change caused by opening the central hole, and the combined magnetic field.

ion source is 0.8 inches, and the geometric parameters of the compensating rings are listed in Table 2-2.

Table 2-2

Compensating Rings' Geometric Parameters

Compensating Ring No.	Inside Radius (in.)	Outside Radius (in.)	Thickness (in.)
1	0.4	0.6	0.400
2	0.6	0.8	0.075

A magnetic charge sheet program was used to calculate the magnetic field produced by the compensating rings and the ion source hole in the center. The median plane field is so strong that saturation conditions can safely be assumed for the iron. Figure 2-7 also shows the calculation results for the field produced by the ion source hole and the compensating rings as well as their combined magnetic field. The combined magnetic field is then added to the magnetic field produced by the POISSON code to form the main magnetic field. Figure 2-8 shows the K value and the field index n of the main magnetic field in the central region after the compensating rings and the central hole for the ion source are added. The influence of the compensating rings and the ion source hole on the magnetic field is limited to the central region and should not affect the magnetic field properties at large radii.

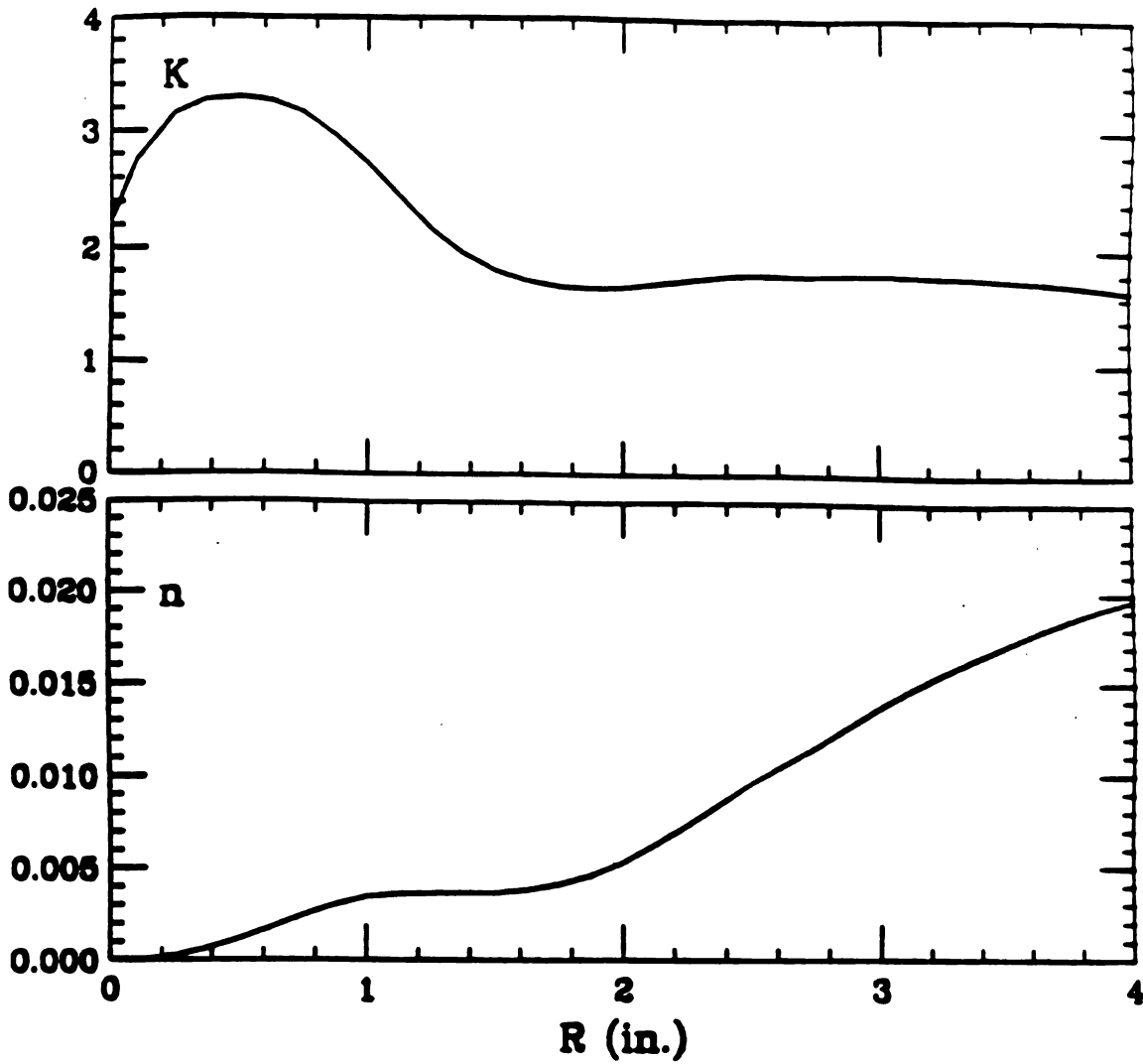


Fig. 2-8 -- At top, plot of the $K = \left(-\frac{Ed\omega}{\omega dE}\right)$ values vs. radius, and at bottom, plot of the magnetic field index vs. radius in the center after the compensating rings and the central hole for the ion source are added.

Chapter 3

Extraction System Design

3.1 Introduction

The 250 MeV superconducting synchrocyclotron has a magnetic field which is about three times stronger than conventional synchrocyclotrons. The magnetic field is about 55.3 kG in the center and remains very strong out to the pole radius of 21 inches where it is about 47.1 kG. This leads to much smaller orbits and therefore creates difficulty in extracting the proton beam. The desire for low activation raises the demand for a high extraction efficiency.

Many methods have been used in the past to extract the circulating beam from the conventional synchrocyclotrons with varying degrees of success. These include, among others, the pulsed electrostatic system [15] and scattering the beam from a thin, high Z target into a magnetic channel [16]. The most successful method, however, has been the regenerative method. This method was invented by Tuck and Teng [17] and developed by Le Couteur [18, 19, 20] during the 1950's, and has been applied to the 450 MeV Chicago synchrocyclotron [21, 22], 160 MeV Harvard synchrocyclotron

[23] and many other synchrocyclotrons since then. Using the traditional passive magnetic channel, the typical extraction efficiency of these older synchrocyclotrons reached the 5 - 10% level. However, using a closed ion source and a high current coaxial coil septum at the channel entrance, the regenerative extraction system of the improved CERN 600 MeV synchrocyclotron [24, 25] has an impressive extraction efficiency of 75%. Based on our desire for a simple and reliable extraction system with high extraction efficiency and good output beam quality, the regenerative method was the logical choice for the 250 MeV superconducting synchrocyclotron.

The regenerative method of particle extraction uses a magnetic field disturbance, the "regenerator", which is superimposed on the synchrocyclotron main magnetic field. As we have shown in Fig. 2-2 in chapter 2, before the regenerator and the magnetic channel are added, the v_z values rise with increasing radius while the v_r values fall. These values cross the $v_r = 2v_z$ ($n=0.2$) resonance at 19.1 in. The beam will not travel out beyond this radius because the $v_r = 2v_z$ ($n=0.2$) resonance couples the large radial oscillations of the orbits into vertical motion, so that the beam blows up vertically. One has to extract the beam before

it reaches this resonance, and this radius determines the approximate starting point for the regenerator.

The regenerator provides a powerful field bump whose strong gradient drives ν_r into the $\nu_r = 2/2$ stop-band while simultaneously depressing ν_z . This is shown in Fig. 3-1 where ν_r and $2\nu_z$ are plotted as a function of energy. The pair of curves for the unperturbed field come together and cross at 258.9 MeV, the $n = 0.2$ resonance as noted above. With the regenerator and magnetic channel present, the two curves diverge with ν_r rising sharply to $\nu_r = 1$ at 255.7 MeV, which becomes the approximate energy of the extracted protons. At this point, $\nu_z = 0.33$, which shows the defocusing effect of the regenerator.

As the beam accelerates out to the regenerator, the stability region shrinks rapidly to zero, thereby spilling the particles out onto unstable orbits along which their radius-gain per turn increases rapidly. Once the turn separation is much larger than the width of the channel septum, the "regenerated" proton beam is extracted rapidly using a magnetic channel. For successful extraction, it is also necessary that the vertical oscillations remain bounded.

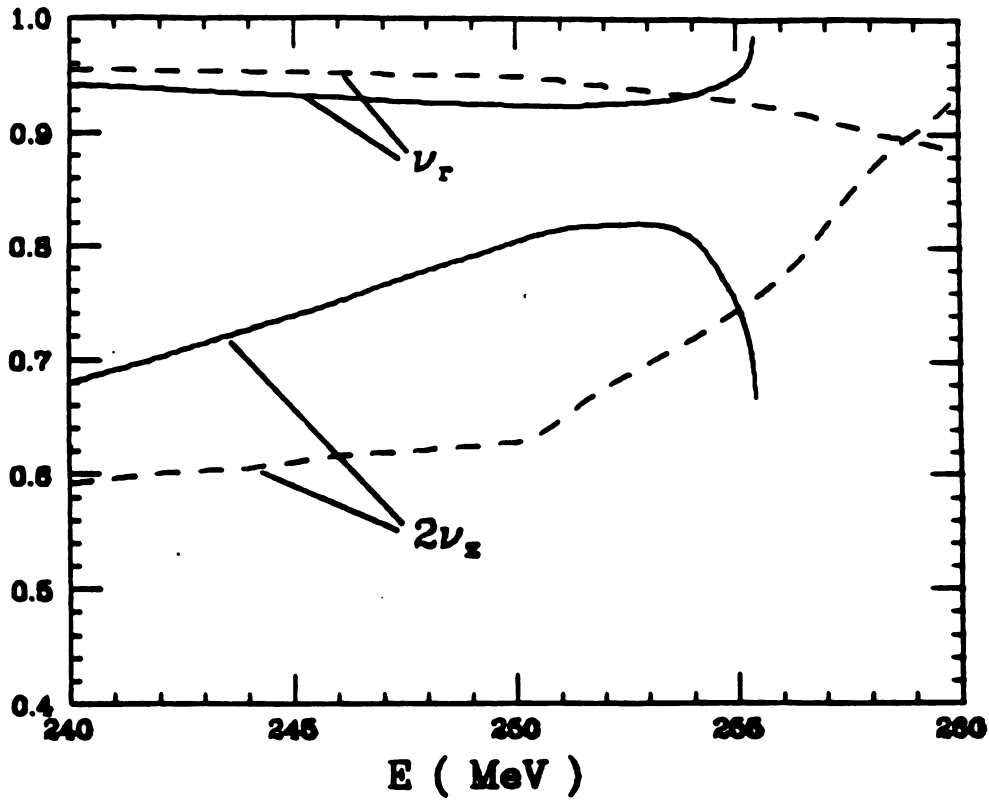


Fig. 3-1 -- Plots of ν_r and $2\nu_2$ vs. energy both without regenerator and the magnetic channel (broken curve) and with regenerator and the channel added (solid curve). $\nu_r = 1$ at 255.7 MeV, the approximate extraction energy.

Our design process consisted of iterating back and forth between calculation of the field produced by the regenerator and the magnetic channel, and computation of extraction orbits in order to systematically improve the design parameters and optimize the extraction efficiency. Figure 3-2 shows the layout of our final design for the extraction system. It shows the arrangement of the regenerator and the magnetic channel elements as well as the last two turns of a typical extracted orbit.

3.2 Orbit Calculation Program

The Z^4 orbit code developed by M. M. Gordon and V. Taivassalo [26] was used in the extraction orbit computations. This code provides an accurate evaluation of the important coupling effects between the radial and vertical motion, since it treats nonlinear effects realistically. It was specifically developed to investigate nonlinear effects in the extraction systems of superconducting cyclotrons where such effects are particularly strong.

In the standard orbit codes used for basic design computations, the median plane field is calculated exactly while the field off the median plane is obtained correctly only to first order in z . This applies to the focusing and

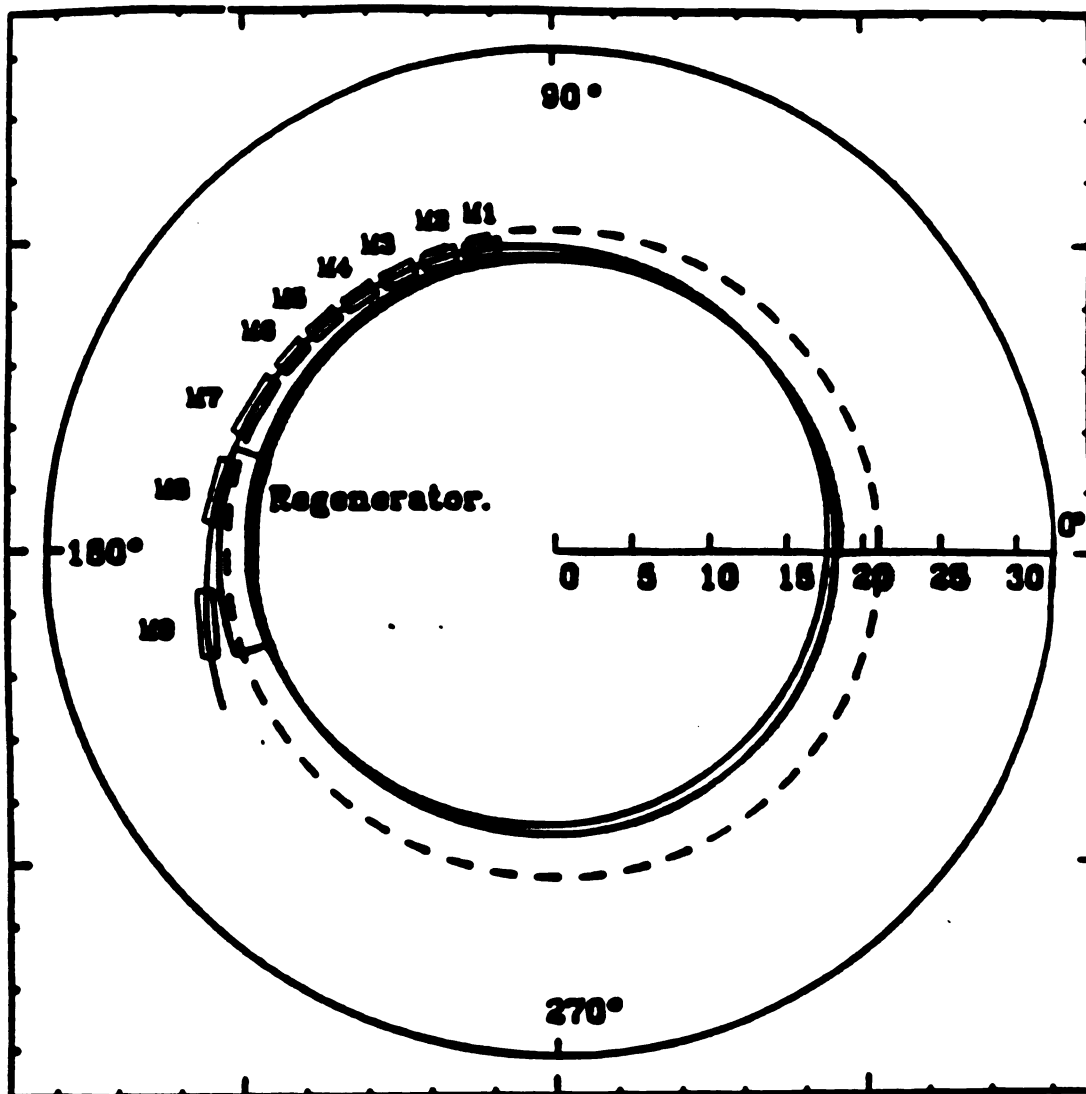


Fig. 3-2 -- Layout of the extraction system showing the arrangement of the regenerator and the nine magnetic channel elements. M1, M2, M5, and M6 are deflecting magnets, and M3, M4, M7, M8, and M9 are all focusing magnets. The solid curve shows the last two turns of an extracted orbit, and the broken curve shows the pole boundary.

deflecting bar fields as well as the main field. In the Z^4 orbit code, the median plane field data are processed so as to allow the main field components to be calculated correctly to fourth order in z . It then uses analytical formulas to calculate the "exact" field produced by the focusing and deflecting elements in the magnetic channel. The regenerator field was pre-calculated and added as a part of the main field. In the magnetic field calculations, we simply assume that the main field is so strong (central field $B = 55.3$ kG) that the regenerator and channel elements are all uniformly magnetized in the vertical direction.

The formulas used in the main field expansion are the following:

$$B_z = - \left[B(r, \theta) - \frac{z^2}{2} B'(r, \theta) + \frac{z^4}{24} B''(r, \theta) \right],$$

$$B_r = -z \frac{\partial}{\partial r} C(r, \theta, z),$$

$$B_\theta = -\frac{z}{r} \frac{\partial}{\partial \theta} C(r, \theta, z),$$

where $C(r, \theta, z) = B(r, \theta) - \frac{z^2}{6} B'(r, \theta)$.

Here, $B'(r, \theta) = LB(r, \theta)$, and $B''(r, \theta) = LB'(r, \theta)$, where L represents the two dimensional Laplace operator. Thus, B_z has terms of order z^2 and z^4 off the median plane, while B_r and B_θ have a z^3 term in addition to the usual linear one.

For the Z^4 orbit code, not only the median plane field $B(r,\theta)$, which is derived from measured or computed field data, is required as input, but the corresponding tables for $B'(r,\theta)$ and $B''(r,\theta)$ are also required, and these must be calculated and stored in advance.

The program assumes that each magnetic channel element is constructed from a set of rectangular iron bars all having one surface parallel to the median plane. This geometry is used because analytical formulas are available [26] for calculating exactly the magnetic field produced by a uniformly magnetized rectangular iron bar. The program then uses these formulas together with superposition to find the exact field produced by all of the channel elements at any point along the orbit of the particle. Although this calculation is very time consuming, it is quite important since the particle orbits come very close to the channel elements.

3.3 Regenerator Design

Our choice of regenerator parameters was derived from an extrapolation of those used in the Harvard cyclotron [23]. According to Le Couteur [20], if the regenerator occupies an angular width $\Delta\theta$ and starts at $r = r_s$ where the field is B_s , then the field it produces should have the form:

$$\Delta B_z = \left(\frac{2\pi}{\Delta\theta}\right) B_s \rho (0.2 + 0.2\rho),$$

for $r > r_s$, where $\rho = \frac{r-r_s}{r_s}$. We chose $\Delta\theta = 30^\circ$ and $r_s = 19$ in.

where the field is $B_s = 51.293$ kG. In addition, we generalize the above formula to the following:

$$\Delta B_z = \left(\frac{2\pi}{\Delta\theta}\right) B_s \rho (k_0 + k_1\rho + k_2\rho^2 + k_3\rho^3),$$

where k_0 , k_1 , k_2 and k_3 are adjustable parameters, and where we have added two high order terms for greater flexibility.

Vertical stability ultimately limits the radius-gain per turn that can safely be achieved in the regenerative process. That is, as the orbits move progressively farther off center, strong coupling effects eventually cause the vertical height of the beam to expand beyond the allowed limits. In order to determine the optimum theoretical regenerator field, each tentative set of k_i values was used to generate a regenerator field, which was combined with the main magnetic field to form a new main field. Orbit calculations were then carried out using our Z^4 orbit code to check the resultant radius-gain per turn and monitor the vertical stability. Many attempts were made to find the optimized regenerator field. Our final regenerator field is given by:

$$\Delta B_z = \left(\frac{2\pi}{\Delta\theta}\right) B_s \rho (0.2 + 0.2\rho - 1.75\rho^2 - 0.85\rho^3).$$

Figure 3-3 shows the final theoretical regenerator field and field gradient, which became the basis for designing the regenerator iron configuration.

A magnetic charge sheet program was used to calculate the real magnetic field produced by the regenerator. The final iron configuration of our proposed regenerator [27] is shown schematically in Fig. 3-4 along with the field change and field gradient that it produces. The regenerator lies between $r = 19.25$ to $r = 21.5$ inches, and has an average angular width of 30° . It has terraced edges to smooth out the azimuthal and radial field variations, and thereby reduce the nonlinear effects of the field on the orbits. The geometry and position of the regenerator are shown in Appendix A.

The nature of the extraction process can best be understood by examining radial phase plots like the one shown in Fig. 3-5. Here values of (x, P_x) are plotted once per turn at $\theta = 180^\circ$ (the center of the regenerator) for two unaccelerated orbits at 255.2 MeV which start just outside the two ends of the stability region. In addition, the contour near the stability boundary at 255.0 MeV is also shown, and it is clear that these orbits lie inside this stability boundary. Thus the shrinking of the stability

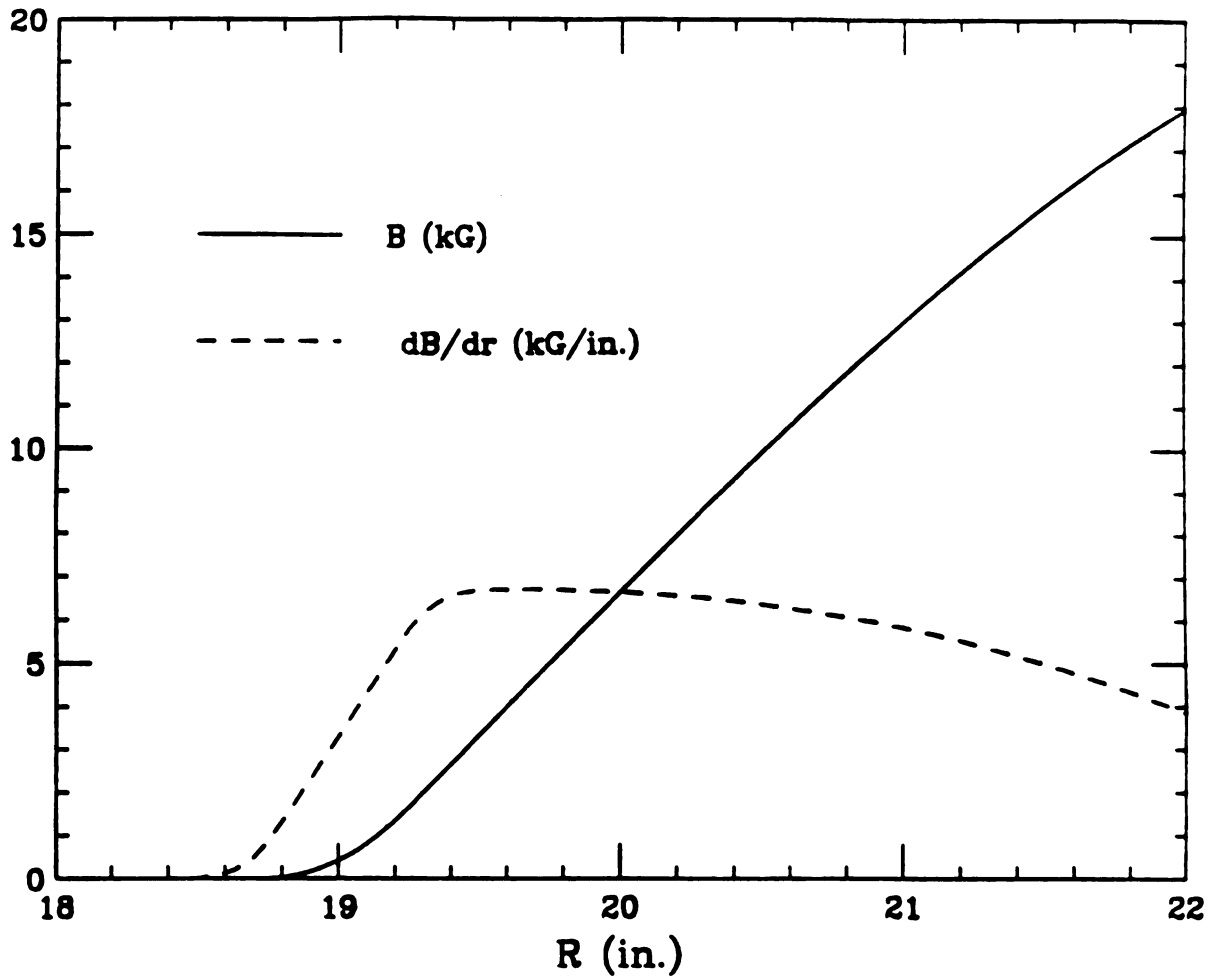


Fig. 3-3 -- Theoretical regenerator field B (solid curve), and its gradient $\frac{dB}{dr}$ (broken curve) vs. radius.

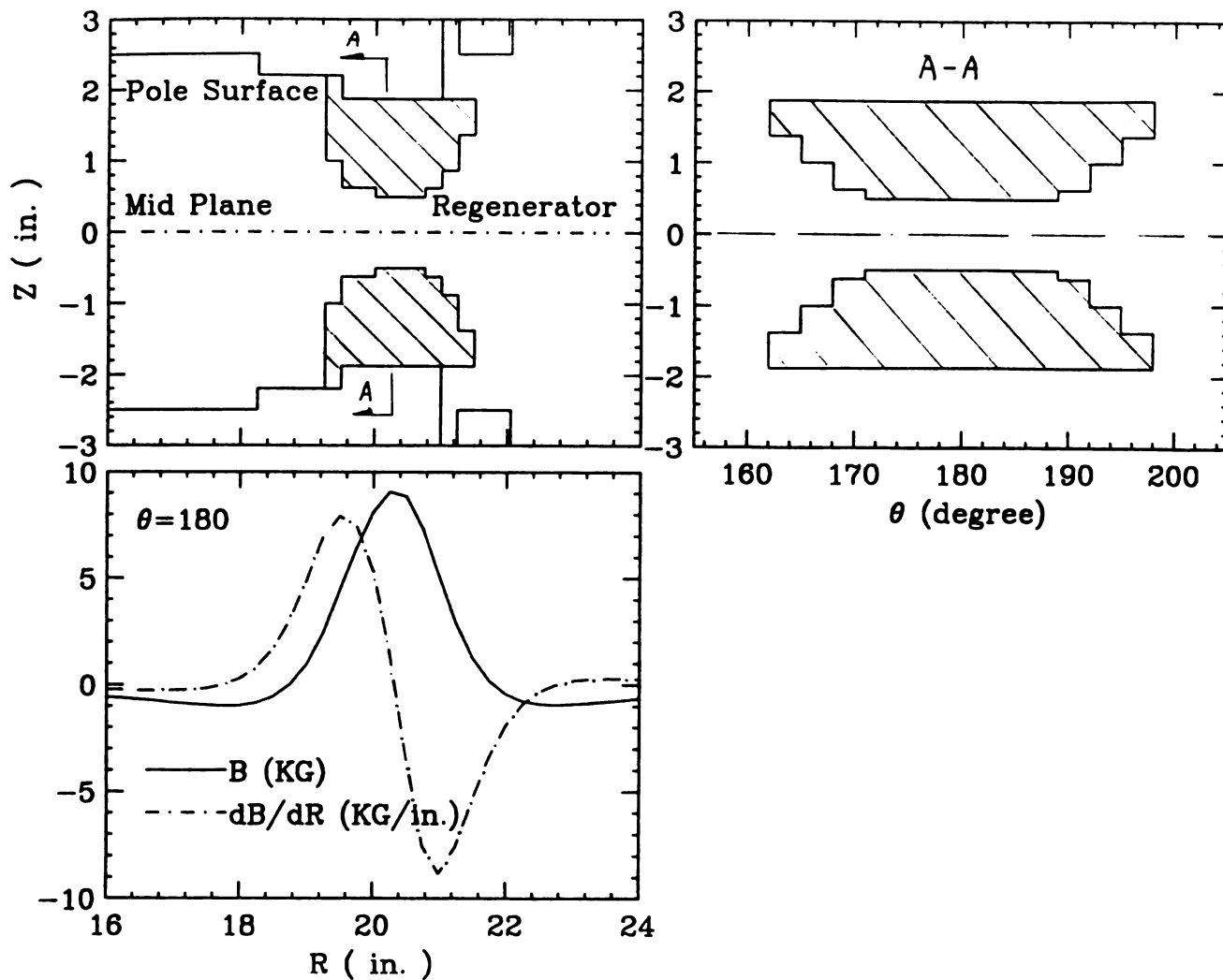


Fig. 3-4 -- At top, the radial profile of the regenerator situated on the edge of the magnet poles. At bottom, the magnetic field B (solid curve) produced by the regenerator, and its gradient dB/dr (broken curve) vs. radius. Plots are at $\theta = 180^\circ$, the center of the regenerator. The azimuthal cross section of the regenerator at 20.0 in. is shown on the right. See Appendix A for more detail.

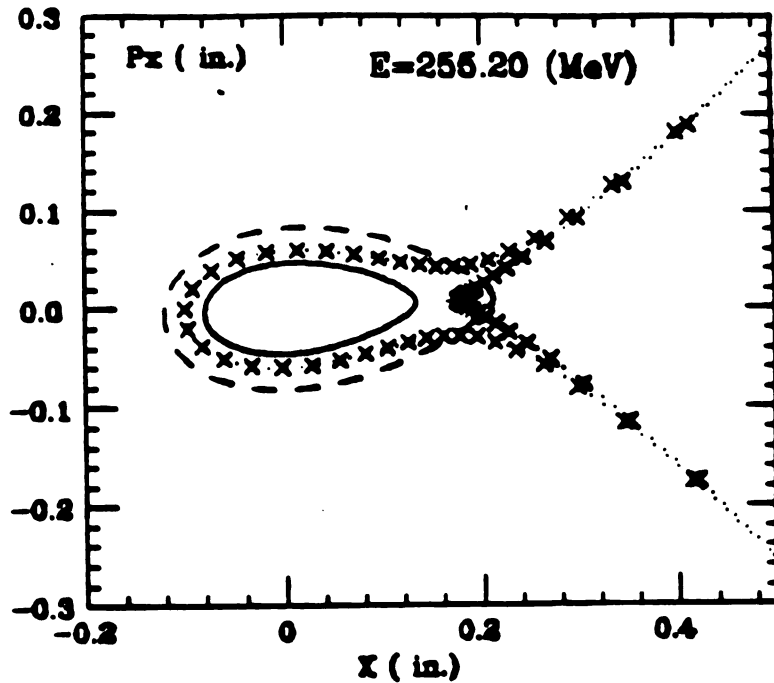


Fig. 3-5 -- Radial phase plots showing the radial motion of two different orbits at 255.2 MeV which start outside the stability boundary indicated by the solid curve. The broken curve shows the contour near the stability boundary at 255.0 MeV, and shows that these orbits were inside the stability region at the lower energy.

region with energy eventually shifts an accelerated orbit into the unstable region. This stability region shrinks to zero completely at 255.7 MeV where $v_r = 1$.

One can therefore see that as the protons accelerate outward, they encounter a rapidly shrinking stability region that eventually causes their orbits to spill over the boundary into the radially unstable region. As shown in Figure 3-5, the phase points then move onto the outflowing asymptote along which their radius-gain per turn increases rapidly, thereby enabling the protons to clear the septum and enter the magnetic channel. Figure 3-6 shows plots of r vs. θ between $\theta = 0^\circ$ and 250° for the last 5 turns of a typical extracted orbit. One can clearly see the rapid growth in orbit turn separation at the entrance of the magnetic channel. In addition to showing the characteristic "node" near $\theta = 50^\circ$, these r vs. θ plots indicate that a radius-gain per turn of about 0.6 in. can be achieved at $\theta = 100^\circ$ and near $r = 19.7$ inches where the channel septum would be inserted.

The impact of the vertical motion on the extraction process was investigated using the Z^4 orbit code. Our results show that strong coupling effects restrict the range of orbit-center displacements and vertical amplitudes that can be extracted successfully. In addition to a given

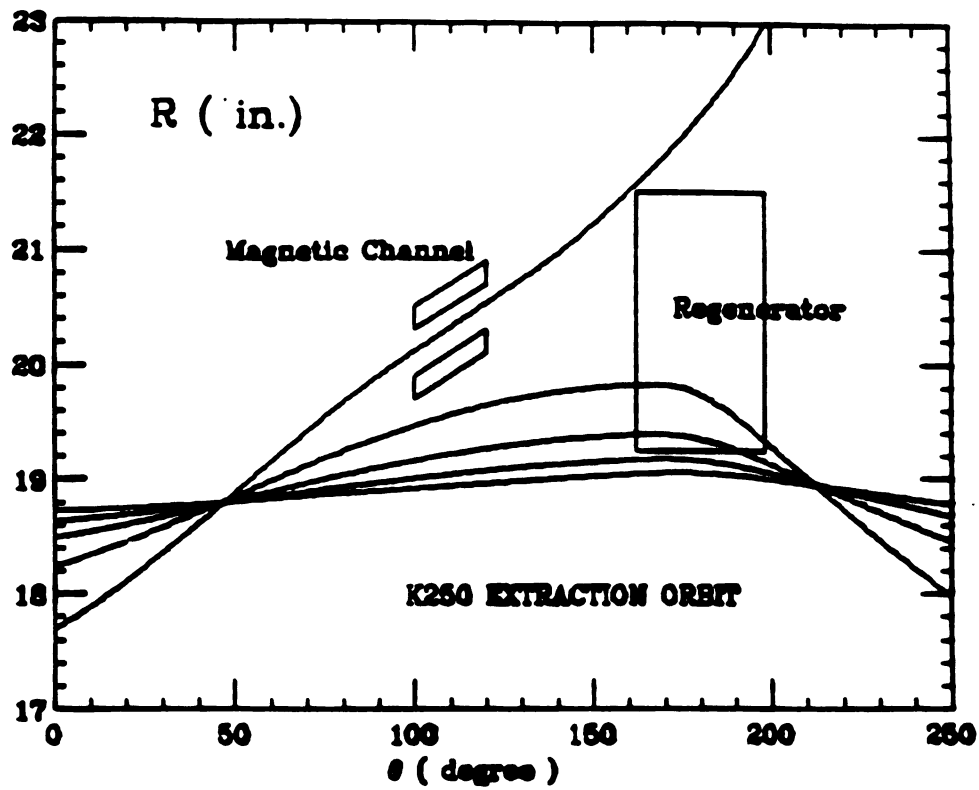


Fig. 3-6 -- Plots of r vs. θ for the last five turns of an extracted orbit showing the growth in turn separations at $\theta = 100^\circ$, the channel entrance. The regenerator shims lie within an area from $\theta = 162^\circ$ to 198° and from $r = 19.25$ to 21.5 in.

starting value for (r, p_r) at each energy investigated, the initial conditions consist of eight (z, p_z) points uniformly spaced around an eigenellipse having a given maximum height Δz_0 . Actually, as a result of median plane symmetry, only four distinct (z, p_z) values are required.

Because of the shrinking stability region, protons with large orbit-center displacements begin extraction at lower energies than those with small displacement. The lower energy extraction orbits therefore suffer the largest growth in vertical height as a result of the stronger coupling action. This is shown in Figs. 3-7 and 3-8 where the height Δz is plotted as a function of turn number for four different energies from 252.0 to 253.5 MeV. In each case, $\Delta z_0 = 0.1$ in., a relatively small value, and the initial (r, p_r) point was chosen so that the protons reach the channel entrance in about 24 turns.

As can be seen, the maximum Δz value increases by a factor ranging from 3.4 at 252 MeV down to 1.3 at 253.5 MeV. Moreover, as Δz_0 increases, the resultant growth factor at each energy also appears to increase. These results indicate that severe beam loss will occur for the part of beam that begins extraction below about 252.0 MeV, while only a small loss will occur for the part above 253.0 MeV.

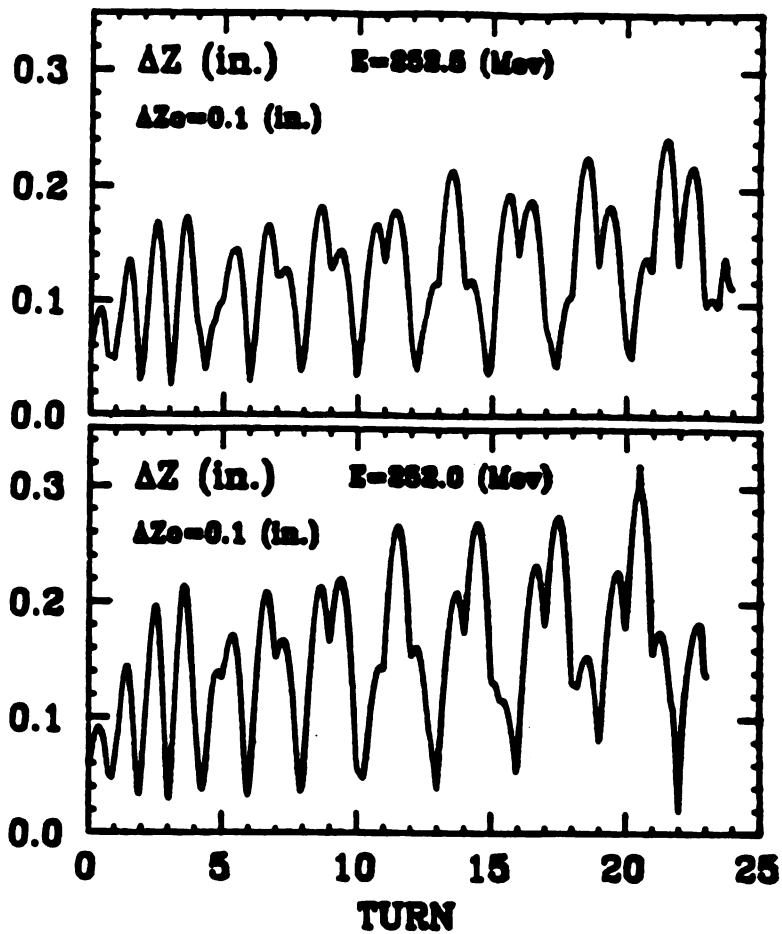


Fig. 3-7 -- Plots of height Δz vs. turn number for a group of orbits having an initial height $\Delta z_0 = 0.1$ in. and energies of 252.0 and 252.5 MeV. All orbits run for about 24 turns to reach the channel entrance. The initial (x, p_x) points are $(-0.265, 0.0)$ for 252.0 MeV, and $(-0.220, 0.0)$ for 252.5 MeV.

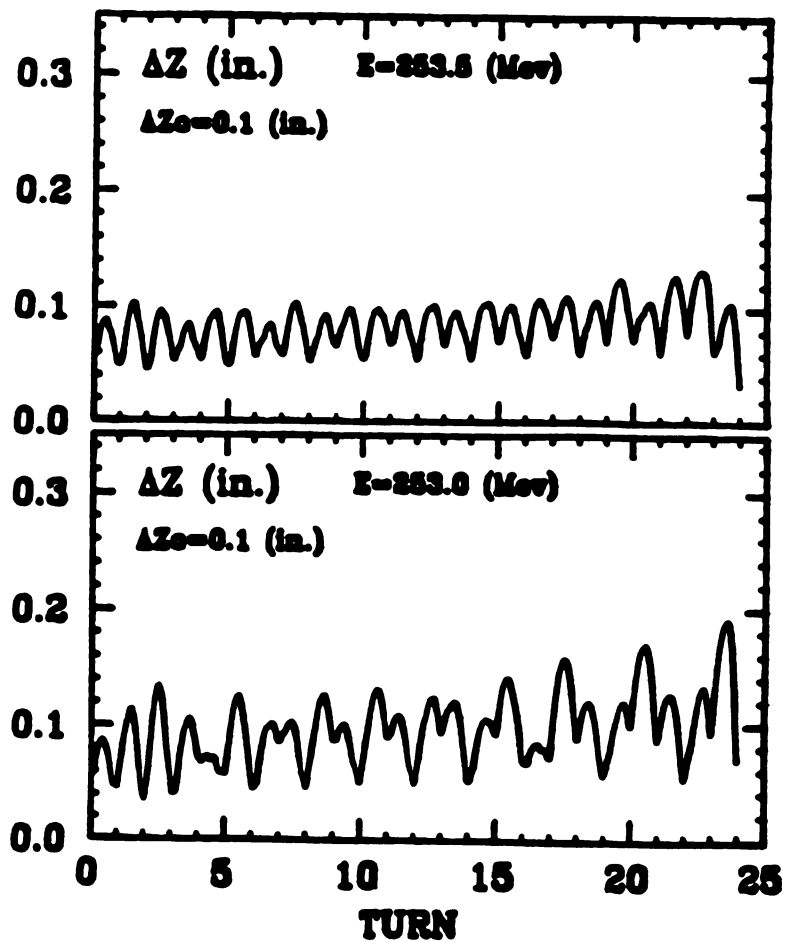


Fig. 3-8 -- Plots of height Δz vs. turn number for a group of orbits having an initial height $\Delta z_0 = 0.1$ in. and energies of 253.0 and 253.5 MeV. All orbits run for about 24 turns to reach the channel entrance. The initial (x, p_x) points are $(-0.170, 0.0)$ for 253.0 MeV, and $(-0.115, 0.0)$ for 253.5 MeV.

We also find that the concurrent coupling of the vertical into radial motion decreases the strength of the regenerator, and this weakening grows rapidly with increasing vertical amplitude. The net effect for a given (r, p_r) value is to increase the number of turns required to reach the channel entrance. Moreover, this increase in turn number is a complicated (seemingly discontinuous) function of both the phase and amplitude of the vertical oscillations. Such behavior is, of course, a consequence of the nonlinearities. In this part of our extraction study, we stop all of the orbits described above when the protons enter the channel at $\theta = 100^\circ$.

3.4 Magnetic Channel Design

The proposed passive magnetic channel consists of a sequence of deflecting and radial focusing elements that bend and focus the beam along its path around the regenerator [28]. A total of nine magnetic channel elements were used to extract the beam out to $r = 23$ inches. Because the orbit curvature is still very large when the particles enter the magnetic channel, the channel elements in the first half of the channel have to be short, since a rectangular bar configuration was used.

The first two channel elements M1 and M2 are deflecting magnets, which consist of two parallel rectangular iron bars symmetric to the median plane. The magnetic field reduction at the center of the channel is approximately given by the uniformly magnetized infinite long bars formula:

$$-\Delta B = \frac{4B_{sat}}{\pi} \left(\frac{th}{a^2 + h^2} \right),$$

where $B_{sat} = 21.4$ kG is the saturation field, $t =$ bar thickness, $h =$ bar height, and $a =$ channel aperture $+ t$. This $-\Delta B$ has its maximum value when $h = a$ and a should have a value close to the final orbit turn separation. However, having an extraction channel with a septum of thickness t and a regenerator which gives a turn separation Δr , the channel entrance efficiency ϵ can be written:

$$\epsilon = 1 - \frac{t}{\Delta r}, \text{ where } \Delta r \geq t.$$

One can therefore see that the thickness of the inner bar of M1 should be as small as possible so as to intercept the least amount of beam and increase the extraction efficiency, but still be thick enough to provide enough field reduction to extract the beam rapidly. The channel selected for this study has an entrance aperture of 0.5 in. and the thickness of the septum is 0.125 in. With the final orbit turn separation of about 0.6 in., the resultant maximum

extraction efficiency ϵ is 79% and the magnetic field reduction in M1 and M2 is 2.5 kG.

The focusing elements M3 and M4 consist of one inner and two outer parallel bars. This type of geometry produces a combination of quadrupole and dipole fields. These focusing bars can therefore provide significant deflecting action together with strong radial gradients inside the channel aperture to control the radial beam envelope. In order to reduce the effects of the fringe field produced by the channel elements on the internal beam, the inner bar of M3 and M4 can not be too thick either, because they are very close to the previous orbits.

The elements M5 and M6 are deflecting magnets like M1 and M2, but thicker bars can be used to increase the field reduction because they are farther away from the previous orbits. The final three channel elements, M7, M8, and M9 are all radial focusing magnets. All the channel elements except M8 and M9 are equipped with an elaborate set of "wings" which serve to shelter the internal beam from the extreme vertical overfocusing that would otherwise occur on the last few turns prior to channel entry. Since M8 and M9 are positioned far away from the previous proton orbits, their fringe field effects on the internal beam are quite small.

Figure 3-9 and Figure 3-10 show the cross-sections and field properties of two channel elements, M1 and M3. The

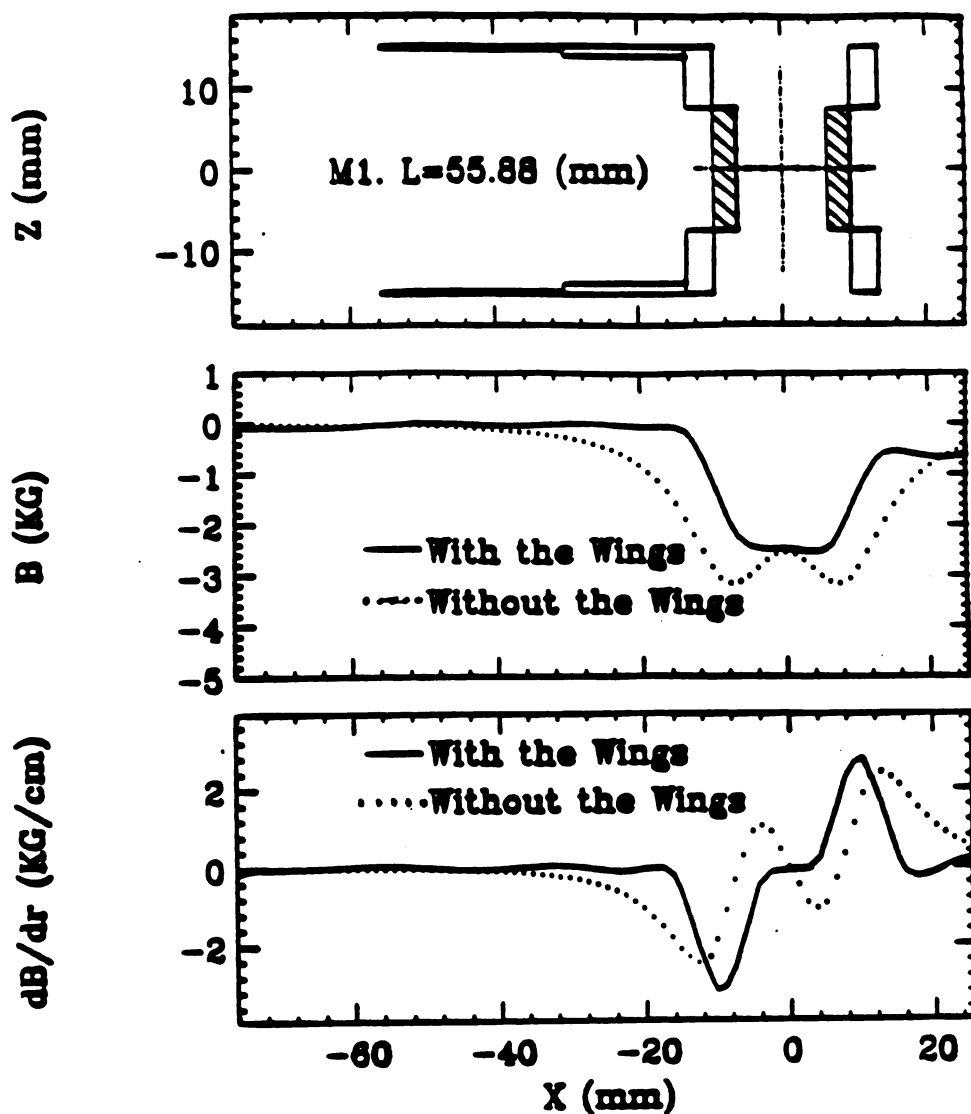


Fig. 3-9 -- Cross section of the deflecting magnet M1 with its projecting wings. Plots show the resultant field (kG) and field gradient (kG/cm) produced with (solid curve) and without (broken curve) the wings. The effectiveness of the wings is apparent. M2, M5, and M6 are similar.

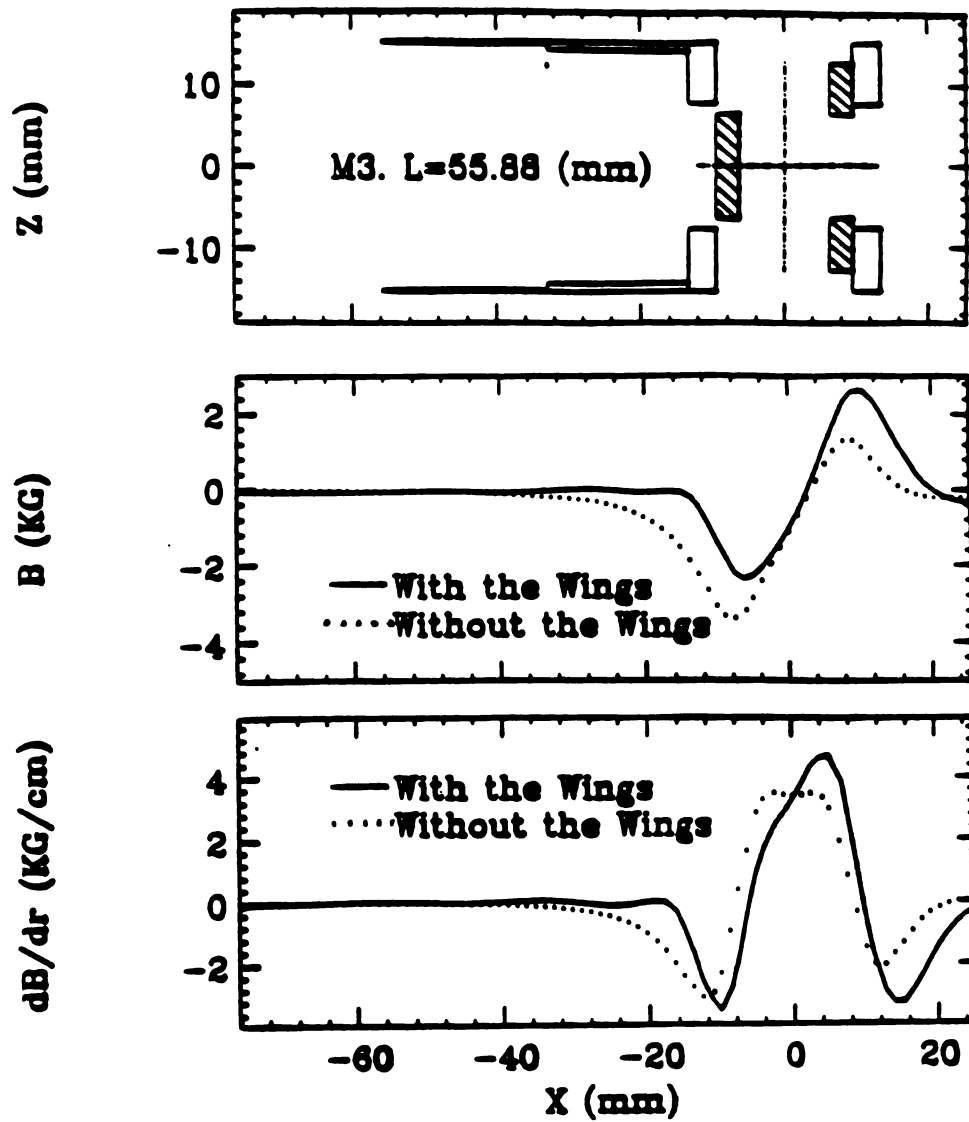


Fig. 3-10 -- Cross section of the radial focusing magnet M3 with its projecting wings. Plots of resultant field and field gradient are analogous to those in Fig. 3-9. M4 and M7 are similar in structure, but M8 and M9 do not require wings.

effectiveness of the wings is apparent. The geometry and position of the channel elements are shown in Appendix B.

3.5 Accelerated Orbit Calculations

The computations of radial and combined radial and vertical motion were also carried out using the Z^4 Orbit Code which is based on exact equations of motion and magnetic field components that are correct to fourth order in z . The results therefore provide a more realistic evaluation of the effects of the vertical motion. Using a constant energy-gain per turn of 10 KeV, the accelerated orbits are traced until they are either successfully extracted or lost through hitting an obstacle. In the combined radial and vertical motion calculations, vertical beam loss is also monitored.

3.5.1 Radial Motion

Figure 3-11 shows the four radial oscillations at $\theta=180^\circ$ and $E=254.5$ MeV that were used as initial conditions for the accelerated orbits. These oscillations correspond to initial radial displacements of 1.27, 2.54, 3.81 and 5.08 mm. Between 60 and 74 points uniformly distributed on these curves were used as initial conditions for the accelerated orbits. The approximate stability boundary is also shown.

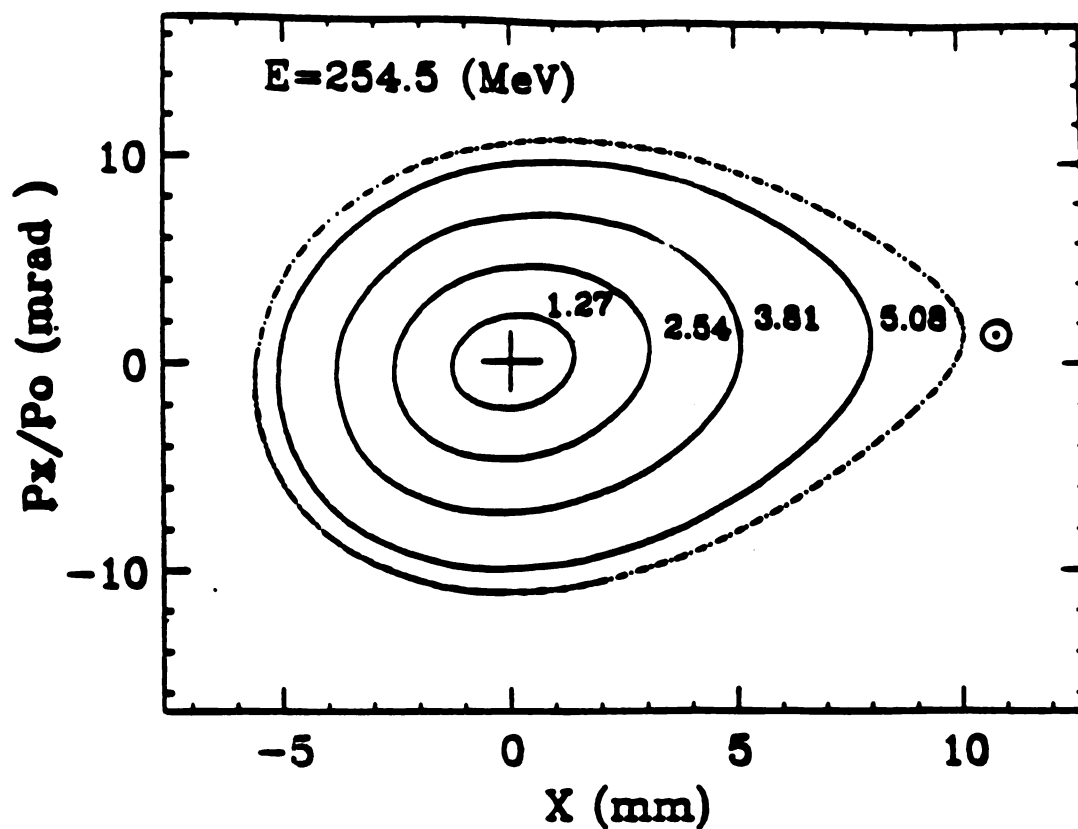


Fig. 3-11 -- Radial phase plots at $E=254.5$ MeV and $\theta=180^\circ$ showing four curves for initial radial displacements of 1.27, 2.54, 3.81 and 5.08 mm corresponding to v_r of 1.0658, 1.0617, 1.0599 and 1.0546 respectively. Between 60 and 74 points on these curves were used as initial conditions for the accelerated orbits. The dot-dash curve shows an approximate stability boundary at this energy.

(This boundary shrinks to zero at $E=255.7$ MeV where $v_r = 1$.) The resulting phase space distribution at the entrance of the magnetic channel is shown in Fig. 3-12 for the four different radial amplitudes. Plotted here are the differences between the (r, p_r) of the orbits and the (r_o, p_{r_o}) of the central ray; also shown are the position and size of the septum. Orbits entering the channel with too small or too large values of p_r hit the inner or outer wall, respectively. About 42% of the orbits are successfully extracted.

3.5.2 Combined Radial and Vertical Motion

For each of the (r, p_r) values used above at 254.5 MeV, we used eight initial (z, p_z) points uniformly spread around an eigenellipse having a given maximum height $\Delta z_o = 2.54$ or 5.08 mm. Figure 3-13 shows the initial (z, p_z) conditions used in these computations.

As shown in the work at CERN [26], orbits with too large radial amplitudes produce unacceptable growth in the vertical oscillations due to the $v_r = 2v_z$ coupling resonance. Our extraction studies show that the reverse can also be

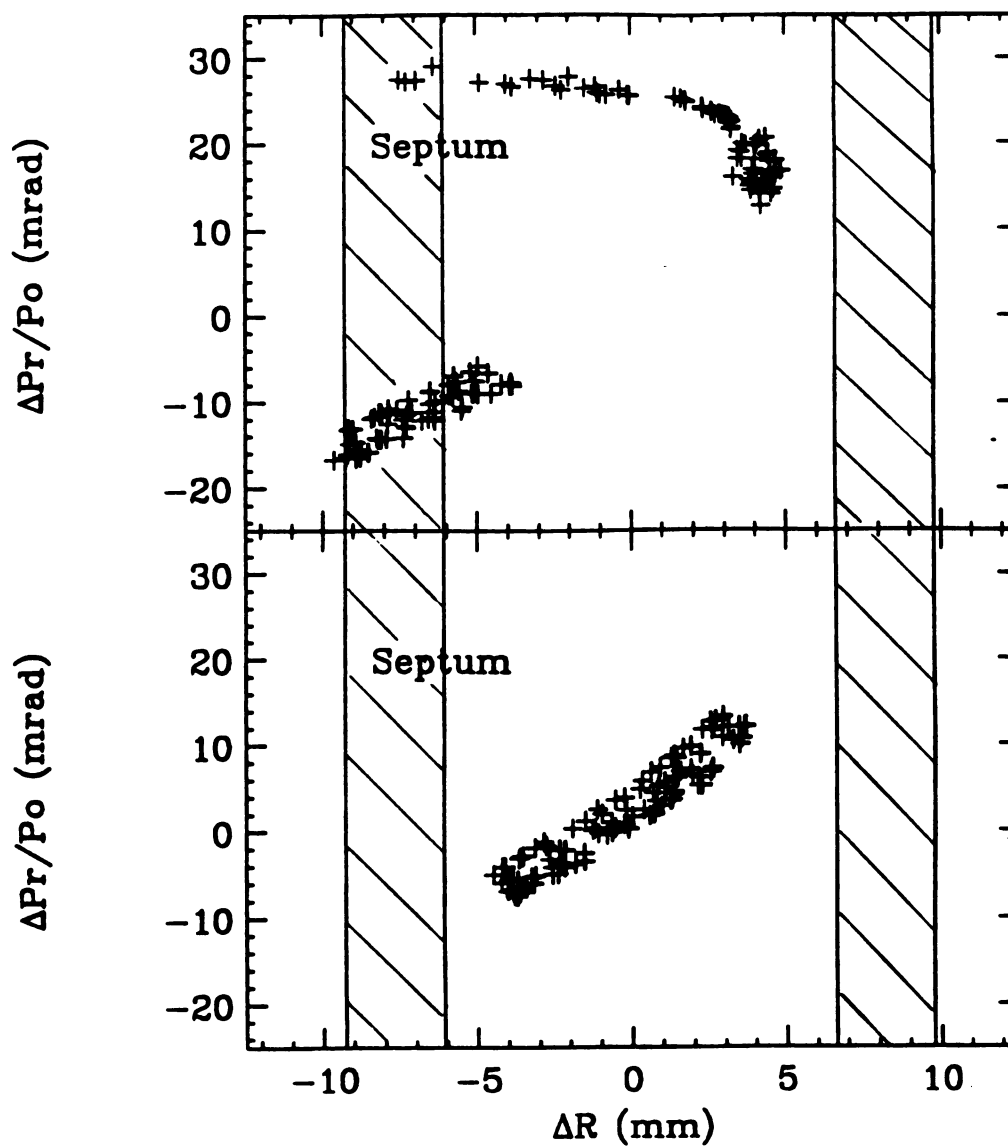


Fig. 3-12 -- Radial phase plot at the entrance of the magnetic channel ($\theta=100^\circ$) showing resultant distribution for median plane orbits with initial conditions given in Figure 3-11. The orbits that successfully go through the magnetic channel are plotted on the bottom and those lost in the extraction process are plotted on the top. (p_0 is the momentum corresponding to $E_0=255.0$ MeV.)

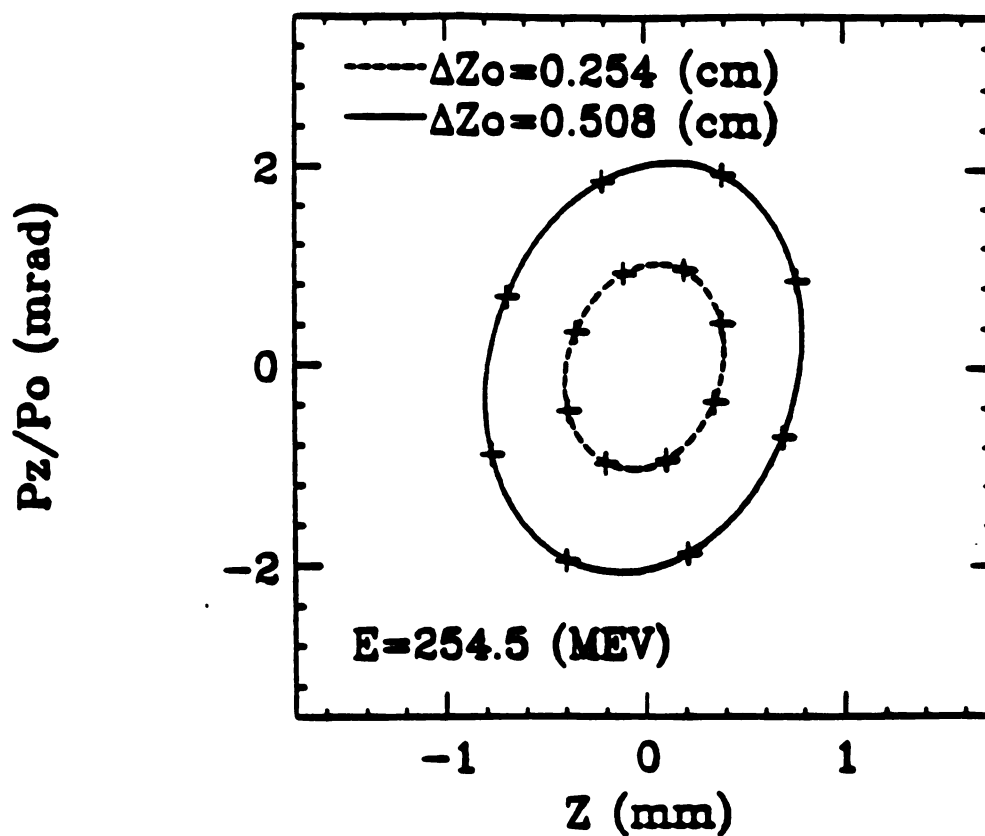


Fig. 3-13 -- Initial (z, p_z) values at $E=254.5$ MeV and $\theta=180^\circ$ used for accelerated orbits in conjunction with the (r, p_r) values given in Fig. 3-11. The two eigenellipses shown here have their maximum height $\Delta z_0 = 2.54$ and 5.08 mm near $\theta=0$.

true and that in some cases, the radial and vertical oscillations grow simultaneously to very large amplitudes. Since $v_r = 1$ and $v_z = 0.5$ in these cases, the $v_r + 2v_z = 2$ coupling resonance could account for this phenomenon. The summary of the accelerated orbit calculation results is shown in Table 3-1. The orbit are lost radially if they hit the magnetic channel elements and lost vertically if they exceed a vertical amplitude limit of 7.5 mm.

Table 3-1

Radial Displacement	Vertical Amplitude	Number of Orbit Run	Extraction Efficiency	Radial Loss	Vertical Loss
1.27 mm	0.00	60	36%	64%	0%
	2.54 mm	60	52%	48%	0%
	5.08 mm	60	50%	50%	0%
2.54 mm	0.00	64	44%	56%	0%
	2.54 mm	64	28%	62%	10%
	5.08 mm	64	35%	51%	14%
3.81 mm	0.00	64	41%	59%	0%
	2.54 mm	64	5%	5%	90%
	5.08 mm	64	5%	3%	92%
5.08 mm	0.00	74	45%	55%	0%
	2.54 mm	74	3%	7%	90%
	5.08 mm	74	3%	2%	95%

For the smallest initial radial displacement used in these studies, 1.27 mm, the coupling action remains within acceptable bounds and 46% of the orbits are successfully extracted. For the 2.54 mm case, the extraction efficiency drops to 36% with about 8% of the orbits exceeding a vertical amplitude limit of 7.5 mm prior to reaching the channel. Figure 3-14 shows the resultant vertical phase space distribution for all of these two sets of orbits at the entrance to the channel.

The results are very different for the two largest initial radial displacements, 3.81 and 5.08 mm. Once the vertical motions are added, about 91% and 93% of the orbits fail to reach the channel entrance. That is, the coupling effects described above produce vertical amplitudes that are too large for the given aperture, 15 mm. Thus we find that reasonably good extraction efficiency can be achieved only if the internal beam prior to extraction has a maximum radial displacement of about 3 mm. This is consistent with the results obtained at CERN where the limit is about 10 mm, since our field is about three times higher than the CERN field and one might expect lengths to scale inversely with the field values.

3.6 Summary and Conclusions

As can be seen from Tables 3-2 and 3-3, assuming now

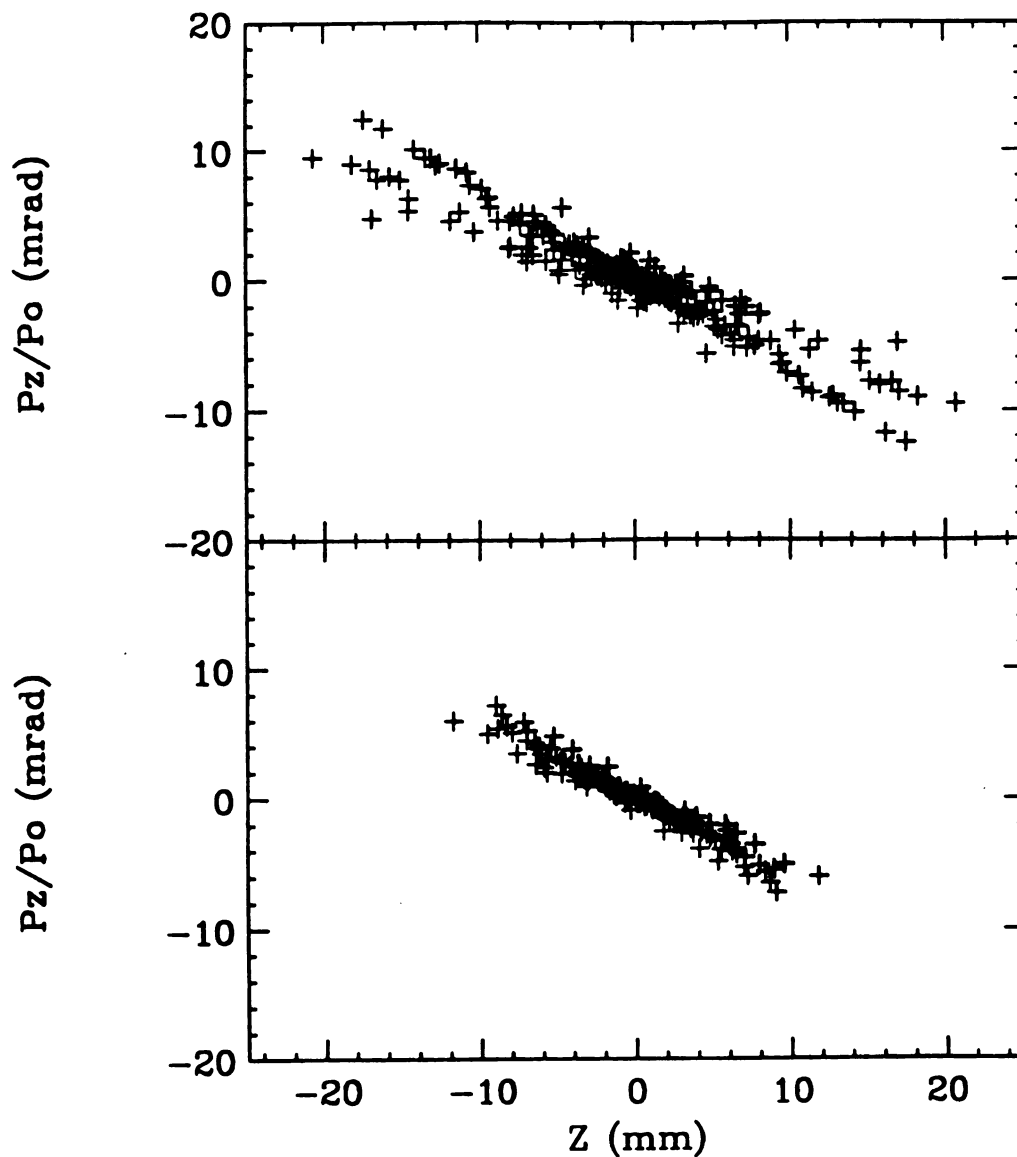


Fig. 3-14 -- Phase plot at the entrance of the magnetic channel ($\theta=100^\circ$) showing the $(z, p_z/p_0)$ values for all the orbits with initial conditions given in Figs. 3-11 and 3-13 for the two smaller initial radial displacements. The orbits that successfully traverse the magnetic channel are plotted on the bottom and those lost in the extraction process are plotted on the top.

that the internal beam can be controlled so that both the radial and vertical amplitudes do not exceed 3 mm, the calculation results indicate that an extraction efficiency of about 40% can be achieved. In agreement with the conclusions reached at CERN [25], our results demonstrate the importance of limiting the radial and vertical phase space occupied by the beam emerging from the central region.

The final calculation results of the extraction orbit properties at the exit of the magnetic channel are shown in Table 3-2. As can be seen, the energy spread, radial and vertical emittances depend quite strongly on the vertical amplitude as well as the radial amplitude.

Table 3-2

Radial Displacement	Vertical Amplitude	Radial Emittance	Vertical Emittance	Energy Spread
1.27 mm	0.00 mm	15 π mm-mrad	0	170 keV
	2.54 mm	19 π mm-mrad	9 π mm-mrad	160 keV
	5.08 mm	20 π mm-mrad	18 π mm-mrad	210 keV
2.54 mm	0.00 mm	14 π mm-mrad	0	220 keV
	2.54 mm	20 π mm-mrad	28 π mm-mrad	620 keV
	5.08 mm	20 π mm-mrad	30 π mm-mrad	590 keV

A plot of the radial and vertical envelopes for the resultant beam as it traverses the magnetic channel is shown in Fig. 3-15, and these results confirm that the beam remains well focused inside the magnetic channel. The corresponding radial and vertical phase space distributions are shown in Fig. 3-16 with resultant over-all emittances of about 20π mm-mrad radially and 30π mm-mrad vertically with 90% of the orbits included. Finally, the projected energy distribution of the extracted beam is shown in Fig. 3-17, and indicates an energy spread of about 600 KeV.

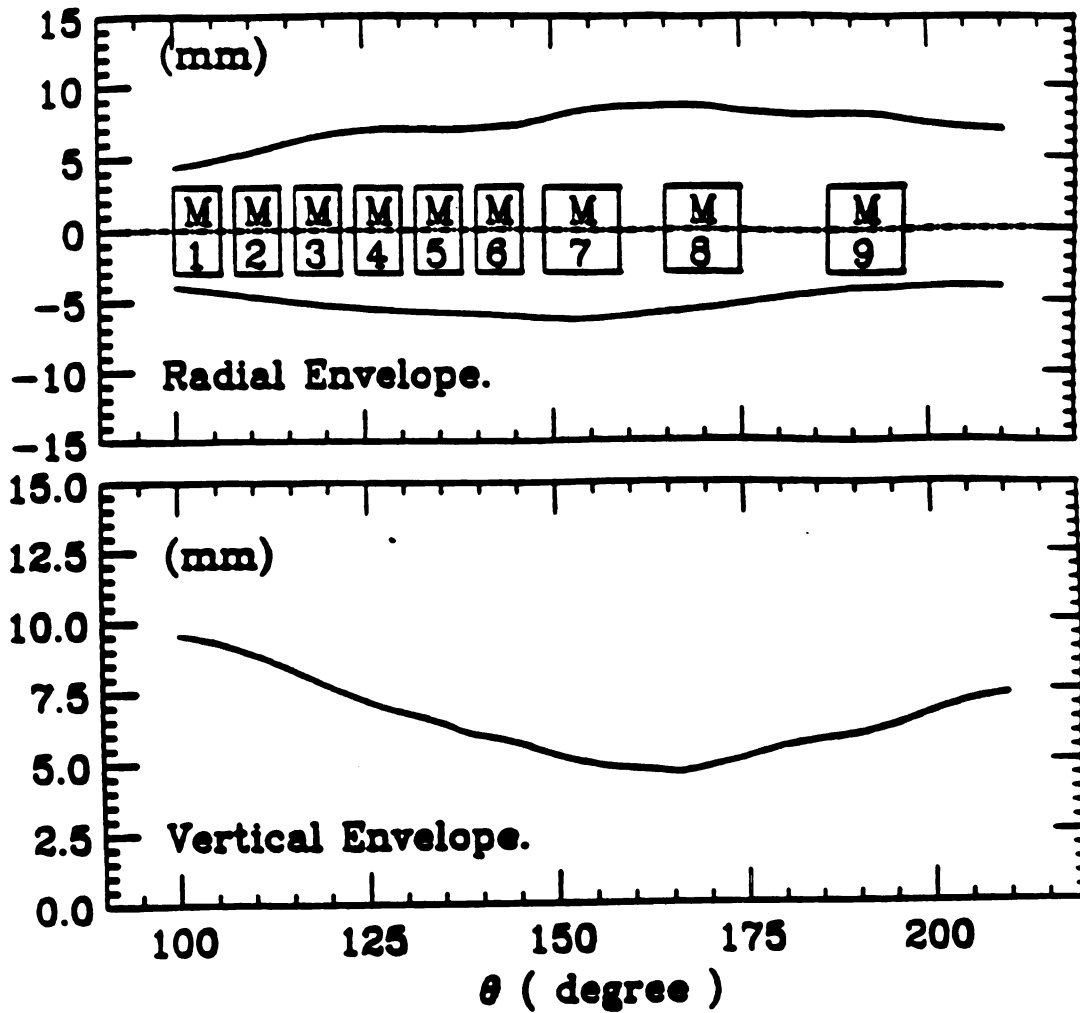


Fig. 3-15 -- Radial and vertical envelopes for all of the successfully extracted orbits as they traverse the magnetic channel. Plots show $(r-r_0)$ and $|z|$ vs. θ from 100° to 210° . All 145 orbits used here started at 254.5 MeV with initial radial displacement and vertical amplitude less than 3 mm.

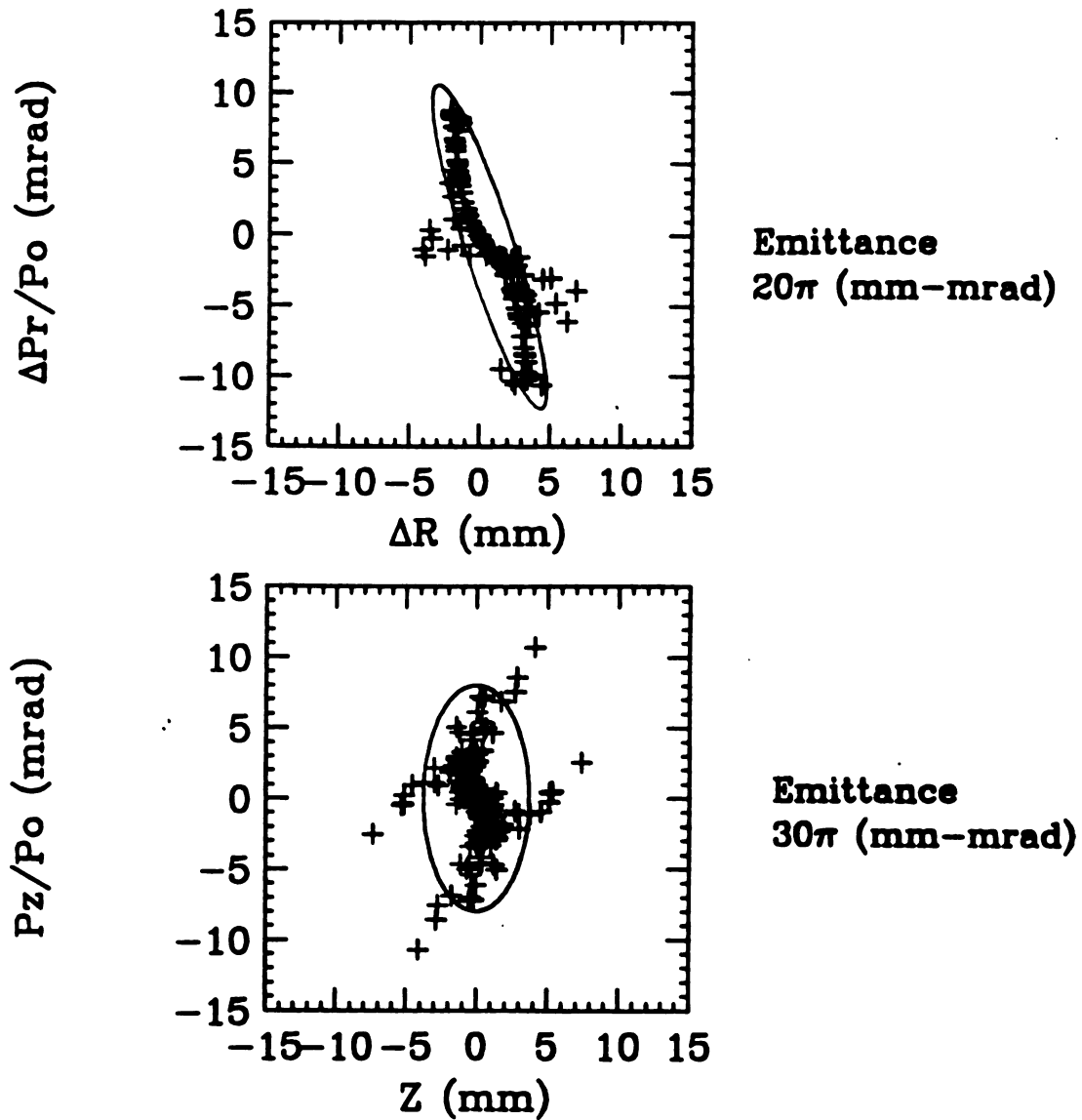


Fig. 3-16 -- Radial and vertical phase plots at the exit of the magnetic channel ($\theta=210^\circ$) showing the distribution of points for the orbits started at 254.5 MeV with initial radial displacement and vertical amplitude less than 3 mm.

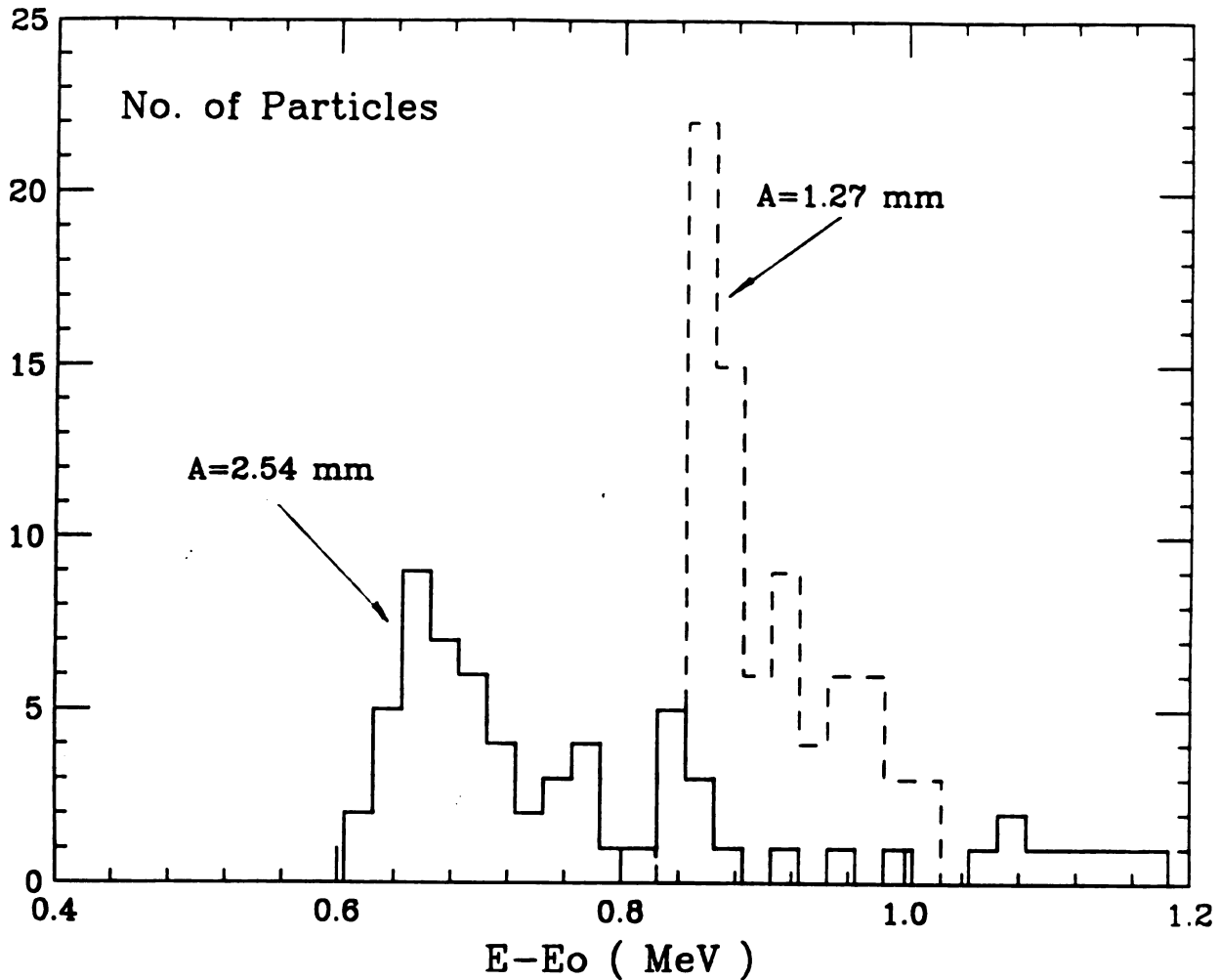


Fig. 3-17 -- Distribution of final energies for the orbits started at 254.5 MeV with initial radial displacement and vertical amplitude less than 3 mm. The histograms show the number of extracted orbits vs. $(E - E_0)$ where $E_0 = 255$ MeV, with two separate curves for initial radial displacements of 1.27 and 2.54 mm. The final energy for the orbit without initial radial displacement is 256.04 MeV.

Chapter 4

Ion Source Experiment

4.1 Introduction

Studies of the extraction system in the preceding chapter show that good internal beam quality is required in order to achieve a good extraction efficiency. The required control of the internal beam quality depends ultimately on the design of the central region electrodes and, in particular, on whether a "closed" ion source (i.e., an ion source with an enclosed plasma and a well defined exit slit) plus puller can be accommodated within the limited space available in the central region.

Initial studies of central region orbits in the 250 MeV superconducting synchrocyclotron show that an enclosed ion source plus puller structure is possible provided the ion source chimney is about 0.1 in. in diameter and the gap between the chimney and the puller is about one to two mm, and with a dee voltage in the 10 to 20 kV range. With these requirements, a major experimental question then needs to be answered. Namely, can we extract enough ion current from an enclosed ion source with a 0.1 in. diameter chimney so as to

have adequate beam current surviving the beam losses in the capture and extraction processes?

In order to answer this question and to have a comparison vs. the Harper cyclotron [29] ion source under similar conditions, we did an experiment to measure the total ion current of the Harper cyclotron ion source and of a modified, small diameter chimney, version of this source. Our ion source experiment [30] consisted of two parts. In test #1, we measured the ion current of the Harper cyclotron ion source, using the 0.250 in. diameter chimney, which is currently used in the Harper cyclotron central region. In test #2, we measured the ion current from the same source, but using a 0.125 in. diameter chimney, which is the standard tubing nearest to the size of the chimney proposed for the 250 MeV superconducting synchrocyclotron central region. The Harper cyclotron has a central magnetic field of 46 kG which is smaller than the central magnetic field of 55.3 kG in the 250 MeV superconducting synchrocyclotron. However, since we will measure the total current from the ion source, the difference in the magnetic fields should not influence the experiment result. Deuterons were used as the test ion because of the existing Harper cyclotron gas supply system.

4.2 Ion Source Experiment Setup

In order to put in the pullers and the supporting system for the test, we took the spider, the part of the dee structure linking the three dees together in the center, out from the Harper cyclotron. The cylindrical copper pullers and the supporting connector are mounted on an insulator (Boron Nitride) which is fixed on one of the magnet hills. They are connected to an RG 213 /U cable, which goes through the Harper cyclotron target hole and a 15 kV vacuum adapter to a SPELLMAN RHR 15N120 high DC voltage power supply. The power supply can provide up to -15 kV peak DC high voltage. Figure 4-1 shows the schematic diagram of the experiment setup, and Figure 4-2 shows the cross section of the central region with puller and supporting system in place for the test. The gap from the source chimney to the puller for both tests is 1.5 mm in order to achieve maximum electric field up to 100 kV/cm. The different geometric parameters used in the tests are listed in table 4-1. Figure 4-3 shows the cross section views of the source chimneys used in the test.

4.3 Ion Source Experiment Result

(1) In test #1, we have measured the ion current of the Harper cyclotron ion source with respect to the extraction voltage V_{ext} , source current I_s and source gas flow Q , using

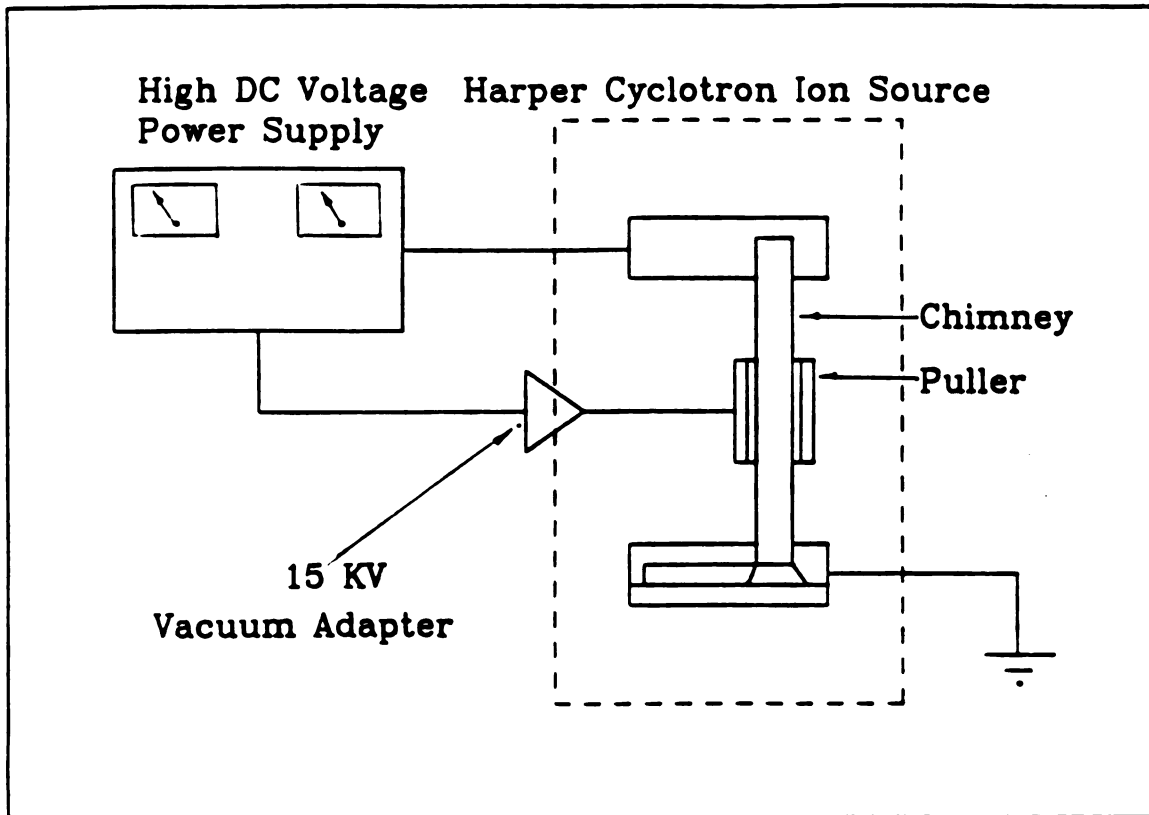


Fig. 4-1 -- Schematic diagram of ion source experiment setup. The Harper cyclotron ion source was used for the experiment.

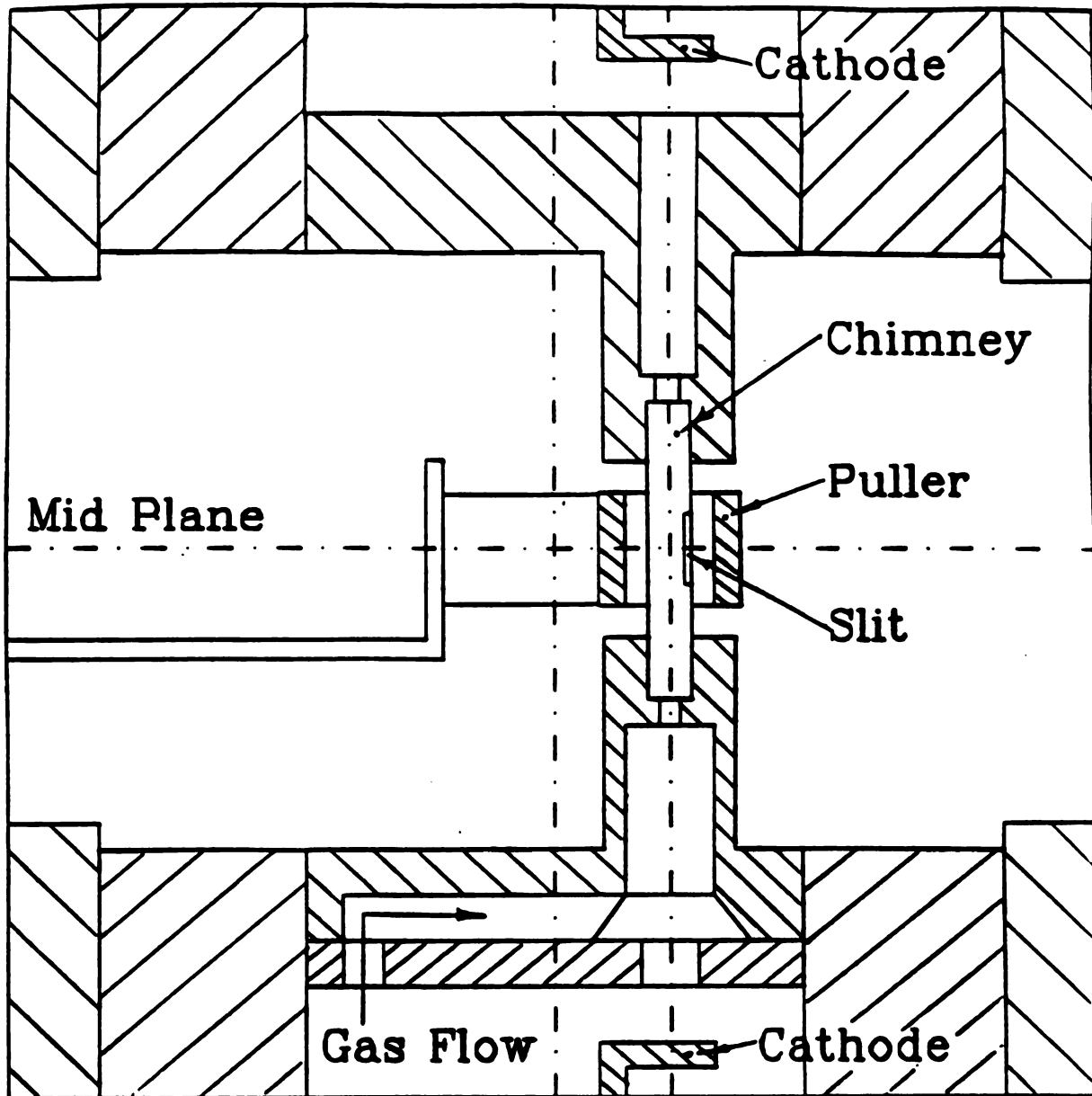


Fig. 4-2 -- Plot of the cross section of the central region with puller and supporting system in place for the experiment. The diameter of the chimney is 0.250 in. in test #1 and 0.125 in. in test #2.

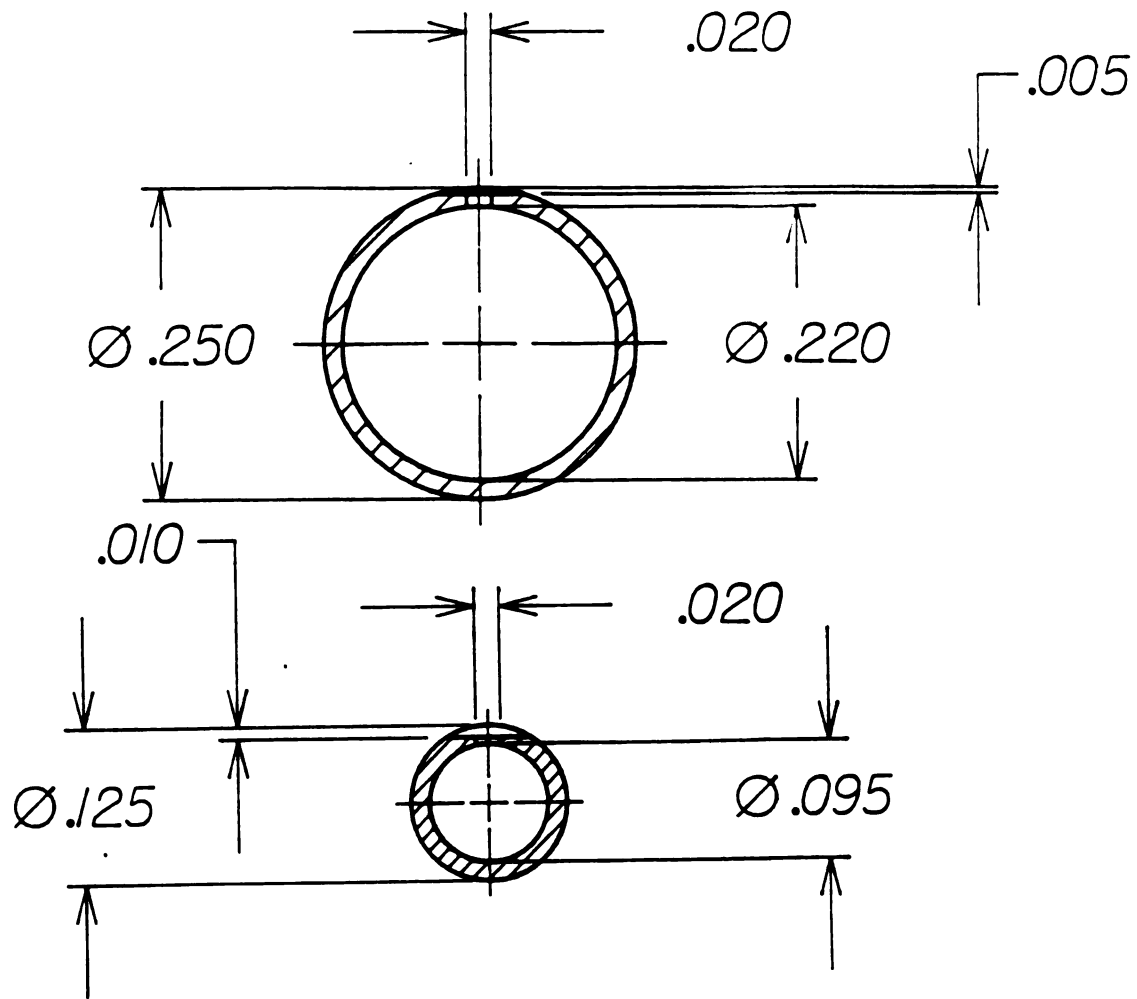


Fig. 4-3 -- The cross section views of the source chimney used in the tests. The scale is at 8:1.

Table 4-1

	Test #1	Test #2
Chimney I. D. (in.)	0.220	0.095
Chimney O. D. (in.)	0.250	0.125
Slit Width (in.)	0.020	0.020
Slit Length (in.)	0.220	0.160
Puller I. D. (in.)	0.369	0.243
Puller O. D. (in.)	0.539	0.394
Gap (mm)	1.500	1.500

a 0.250 in. diameter chimney (the size normally used in the Harper cyclotron central region. The vacuum in the vacuum chamber is 2.5×10^{-5} (Torr). Figures 4-4, 4-5 and 4-6 show the three different ion current measurements.

(2) In test #2, we have measured the ion current of the same ion source with respect to the extraction voltage V_{ext} , and source gas flow Q , using the 0.125 in. diameter chimney, which is very close in size with the chimney proposed to be used in the 250 MeV superconducting synchrocyclotron central region. The arc voltage in the source V_s is 3.10 kV and the vacuum of the vacuum chamber is at 9.0×10^{-5} (Torr). The differences of the background pressure due to the opening of the vacuum chamber to replace the source chimney and the higher gas flow in this test cause the higher pressure in

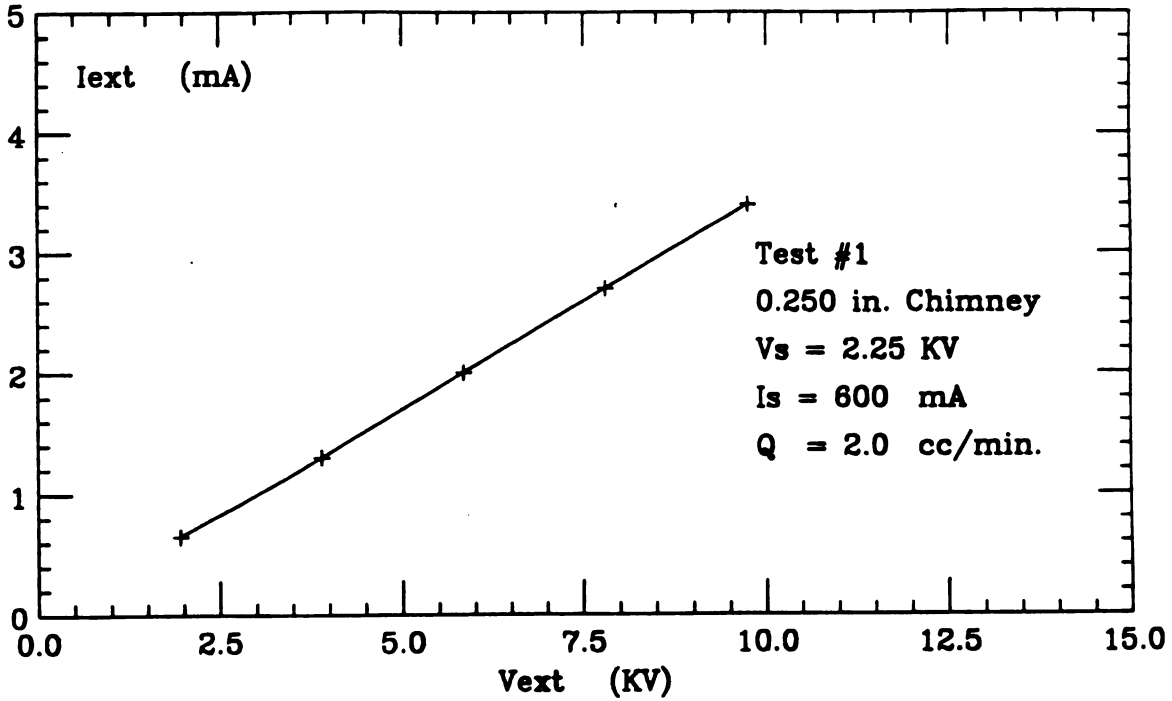


Fig. 4-4 -- Plot of ion current I_{ext} vs. extraction voltage

V_{ext} in test #1.

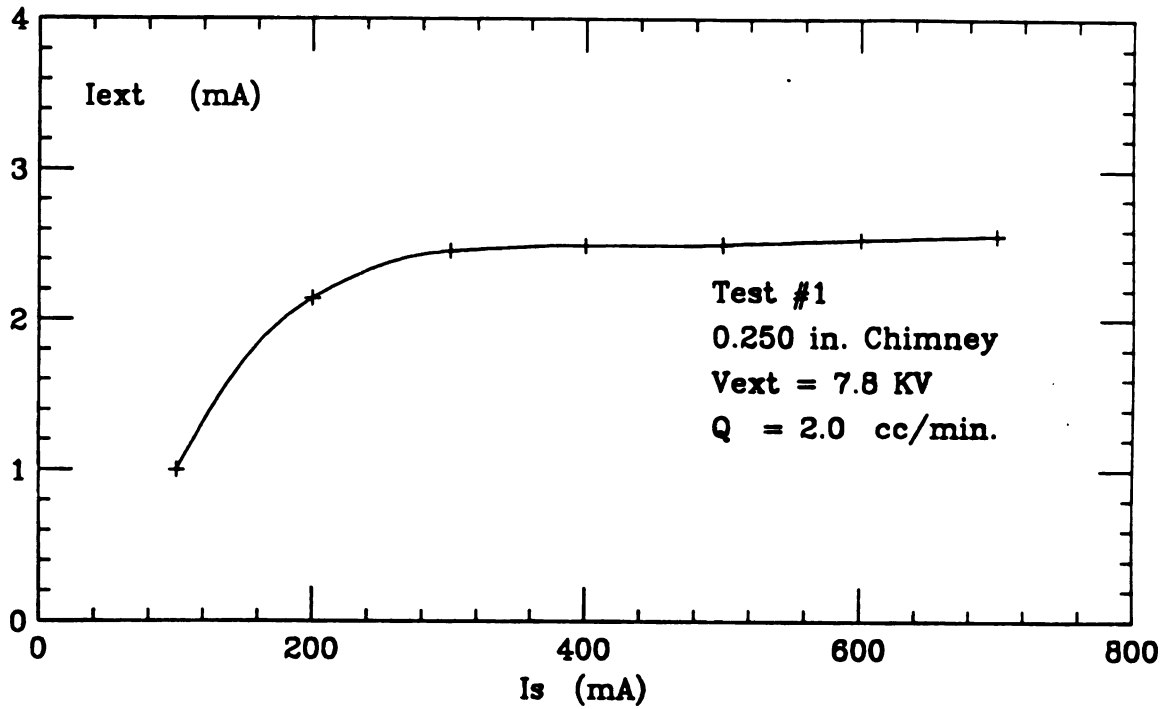


Fig. 4-5 -- Plot of ion current I_{ext} vs. source current I_s in test #1. With a constant extraction voltage $V_{ext} = 7.8 \text{ kV}$, the ion current I_{ext} saturated when source current I_s reached about 300 mA.

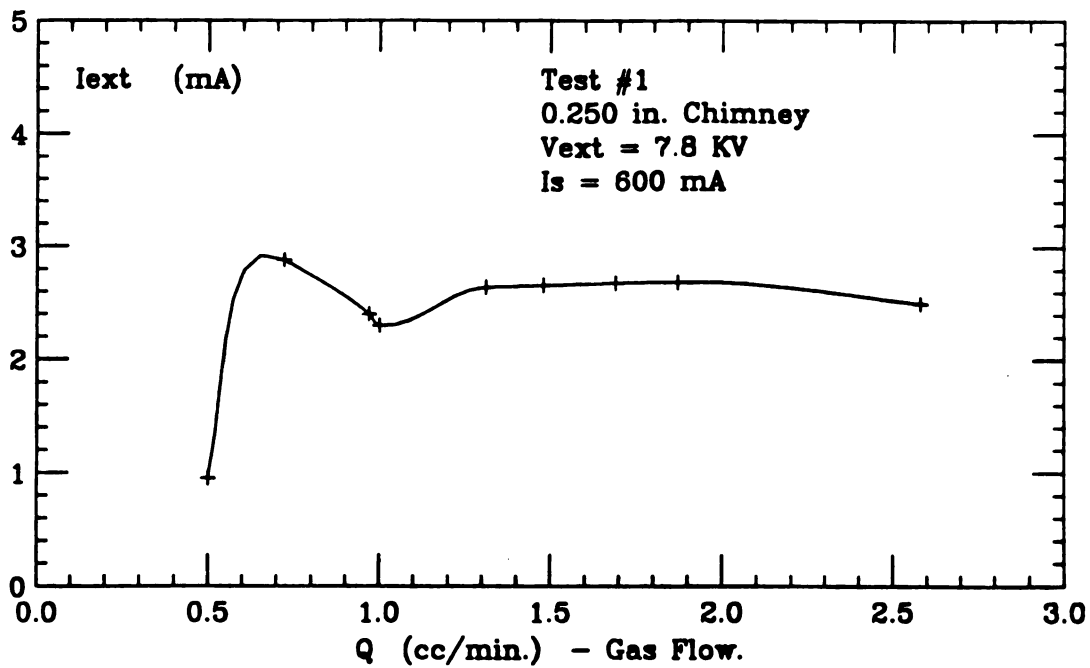


Fig. 4-6 -- Plot of ion current I_{ext} vs. gas flow Q in test #1. With a constant extraction voltage $V_{ext} = 7.8 \text{ kV}$, the ion current I_{ext} saturated when gas flow Q reached about 1.25 cc/min.

the vacuum chamber. Figures 4-7 and 4-8 show the two different ion current measurements.

The Child-Langmuir space-charge law

$$I_m = k \frac{V^{3/2}}{d^2}$$

gives the maximum current that can be drawn from an infinite plate diode with cathode-anode separation d and applied voltage V . For deuterons, the I_m is then given by

$$I_m = 1.218A(\text{cm}^2) \frac{V^{3/2}(\text{kV})}{d^2(\text{cm})} \quad (\text{mA}),$$

where A is the slit area of the source chimney. For test #1 with the extraction voltage $V_{\text{ext}} = 10$ kV, the result is $I_m = 47.11$ mA while the experiment result is $I_{\text{ext}} = 3.4$ mA. For test #2 with the extraction voltage $V_{\text{ext}} = 13.75$ kV, the result is $I_m = 55.21$ mA while the experiment result is $I_{\text{ext}} = 1.8$ mA. The calculated currents are more than one order of magnitude larger than the experiment results possibly due to the difference in the assumptions of infinite supply of ions in the Child-Langmuir space-charge law and the limited ion supply in our actual experiment conditions.

4.4 Result Analysis and Conclusion

We used TRIUMF's RELAX3D code [31] to calculate the

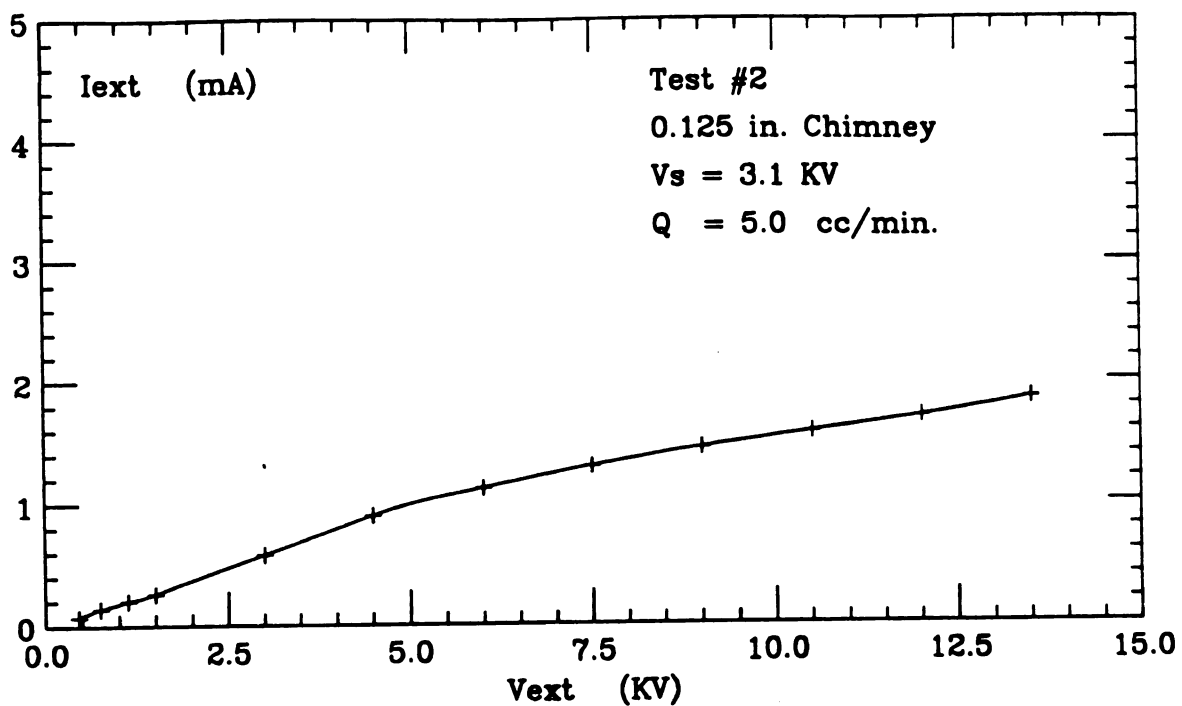


Fig. 4-7 -- Plot of ion current I_{ext} vs. extraction voltage V_{ext} in test #2.

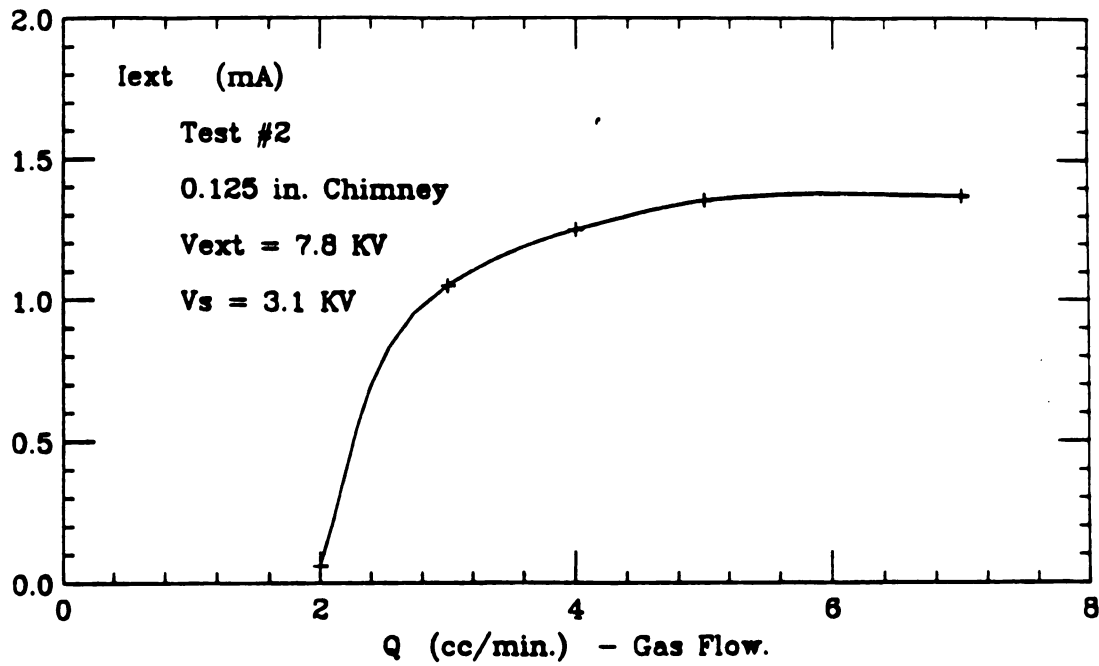


Fig. 4-8 -- Plot of ion current I_{ext} vs. gas flow Q in test #2. With a constant extraction voltage $V_{ext} = 7.8$ kV, the extracted ion current I_{ext} saturated when gas flow Q reached about 4.0 cc/min.

electric fields between the chimney and the puller region for both test #1 and #2 geometries. Figures 4-9, and 4-10 show the electrical potential contour maps with no conducting plasma in the chimney for the two tests respectively. The chimney and the puller boundaries are also shown in the figures. Using these contour maps, we get the electric field distributions along the center line of the chimney slit, as shown in Fig. 4-11 for both test #1 and #2 with different extraction voltages. The results show how the electric field penetrates into an empty chimney with different extraction voltages. The wall thickness of the chimney along the center axis of the slit is 0.010 in. for test #1 chimney and 0.005 in. for test #2 chimney. These are also shown in Fig. 4-11. Line A and Line C show the inside and outside boundary of the 0.250 in. diameter chimney, and line B and line C are those of the 0.125 in. diameter chimney. From Fig. 4-11, one can see that the electric fields in the region close to the chimney slit are mainly decided by the extraction voltage and do not depend much on the chimney sizes since the chimney slit is the dominant factor here. However, the electric fields on the surface of the plasma are quite different for the two cases because the wall thickness of the chimney in test #1 is twice as big as that of the chimney in test #2, and we assume the chimney inside boundary as the surface of the

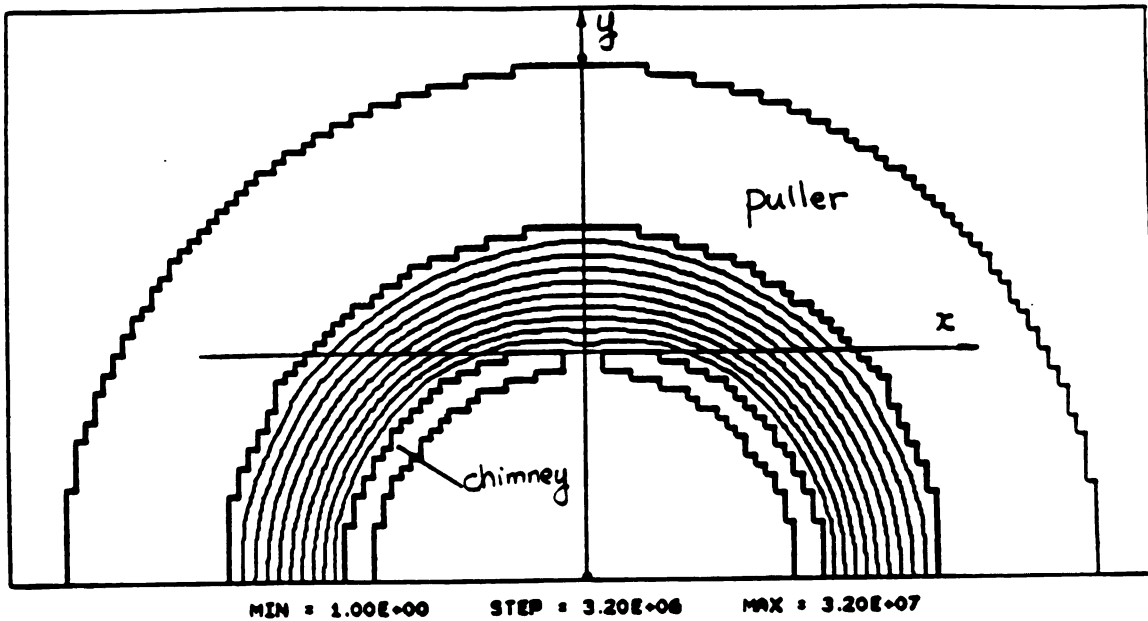


Fig. 4-9 -- The potential contour map of electric field between chimney and puller in test #1. The diameter of the chimney is 0.250 in. Also shown here are X and Y-axis along which the electric field distribution is calculated. No conducting plasma is assumed in the source chimney.

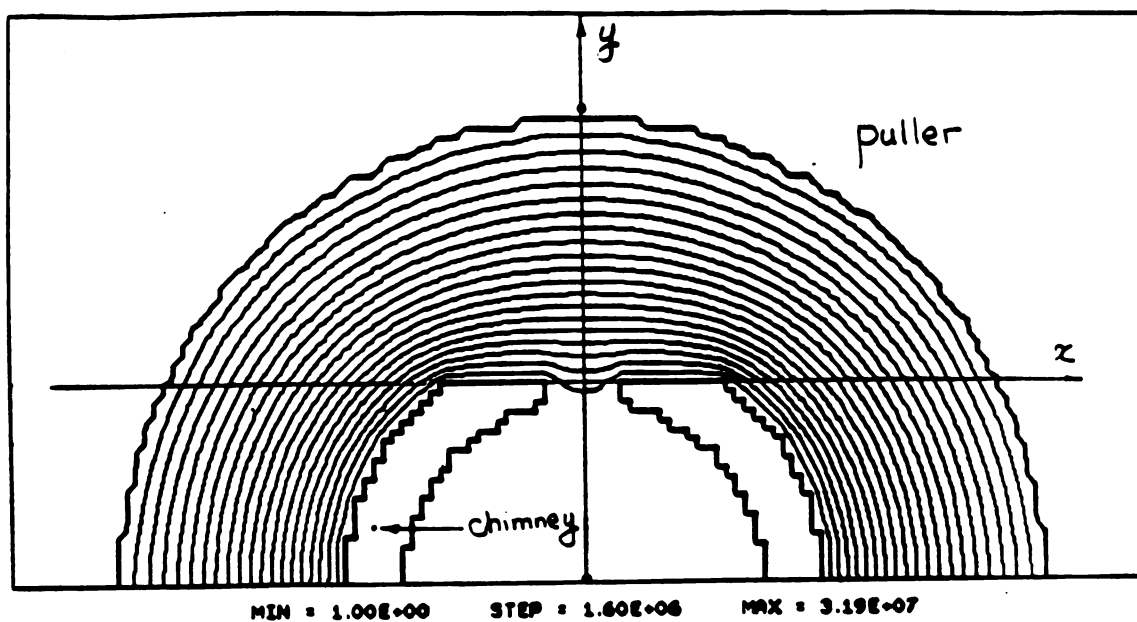


Fig. 4-10 -- The potential contour map of electric field between chimney and puller in test #2. The diameter of the chimney is 0.125 in. Also shown here are X and Y-axis along which the electric field distribution is calculated. No conducting plasma is assumed in the source chimney.

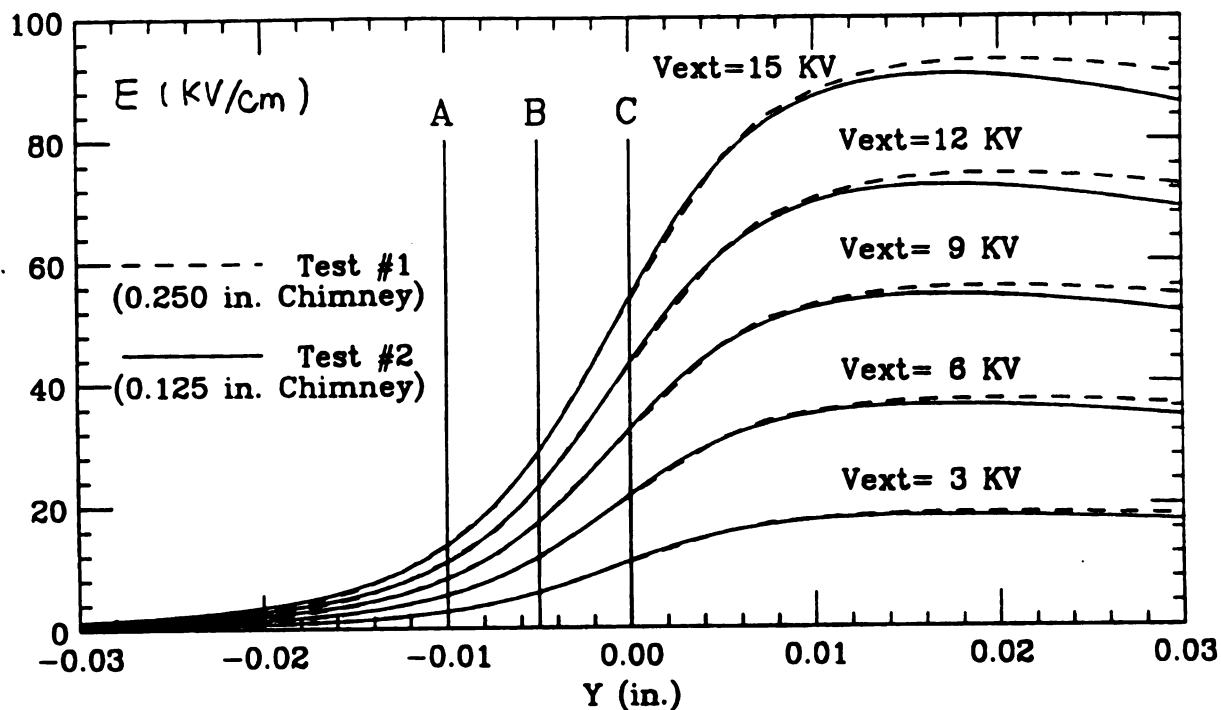


Fig. 4-11 -- Plots of electric field along the Y-axis in test #1 and #2 with different extraction voltage. Line A and line C are the inside and outside boundary of 0.250 in. diameter chimney wall along the center axis of the slit, and line B and line C are those of 0.125 in. diameter chimney. No conducting plasma is assumed in the source chimney. (Different gaps used in the calculations caused differences between the electric fields of the two cases with same extraction voltage in the region away from the chimney.)

plasma. The results show that we could get a higher output ion current by using a thin wall ion source chimney. These electric fields are calculated with assumption of no conducting plasma in the chimney. Plasma in the chimney will of course modify these results but major trends should be the same.

The extracted ion current I_{ext} might be expected to be proportional to the cross section of the chimney and the electric field on the surface of the plasma. The cross section of the chimney in test #1 (0.220 in. inside diameter) is about four times that in test #2 (0.095 in. inside diameter). The strength of the electric field at the inside diameter of the chimney in test #1, E_A , is only half of that in test #2, E_B , as is shown in Fig. 4-11. Combining these two factors, we should have $I_{ext1} = 2I_{ext2}$. Figure 4-12 shows I_{ext} in test #1 and $2I_{ext}$ in test #2 as a function of extraction voltage, and we can see they agree with the argument quite well.

We find that the extracted ion current I_{ext} quickly increased as gas flow was increased, saturating very quickly with a constant extraction voltage in both tests. This agrees with the other source experiment results. Again the saturated ion current I_{ext} in test #1 should be twice that

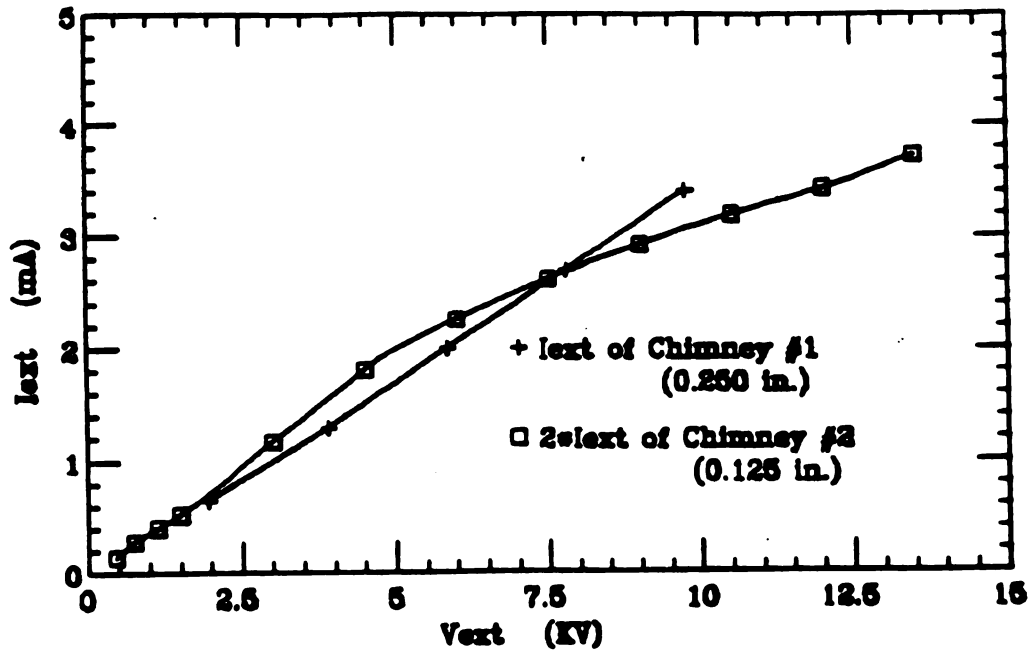


Fig. 4-12 -- Plots of I_{ext} in test #1 (0.250 in. diameter chimney) and $2I_{ext}$ in test #2 (0.125 in. diameter chimney) vs. the extraction voltage V_{ext} .

in test #2, since the same argument also applied here. I_{ext} in test #1 and $2I_{\text{ext}}$ in test #2 are plotted vs. the gas flow in Fig. 4-13. Again we can see they agree with the argument well, although the required gas flow is quite different in two different cases.

The peak ion current obtained with the 0.125 in. diameter chimney and a rectangular slit is about 1.85 mA when the extraction voltage was 13.5 kV. The average electric field used here is only 90 kV/cm. In the final design of the 250 MeV superconducting synchrocyclotron, we will use dee voltage of 20 kV with the gap from source to puller of 1.5 mm and a 0.125 in. diameter chimney with a circular slit (opening angle 120°). The average electric field will be about 133 kV/cm. The stronger average electric field between the source and puller will certainly increase the output ion current. Based on the operating experience of the Harper cyclotron ion source, a circular slit with an opening angle will also help the electric field penetrate into the plasma therefore increasing the output of the ion source current as well. Although there are certainly some differences between our ion source experiment and the proposed 250 MeV superconducting synchrocyclotron ion source, this result nevertheless indicates that it is possible to obtain enough ion current from a central region

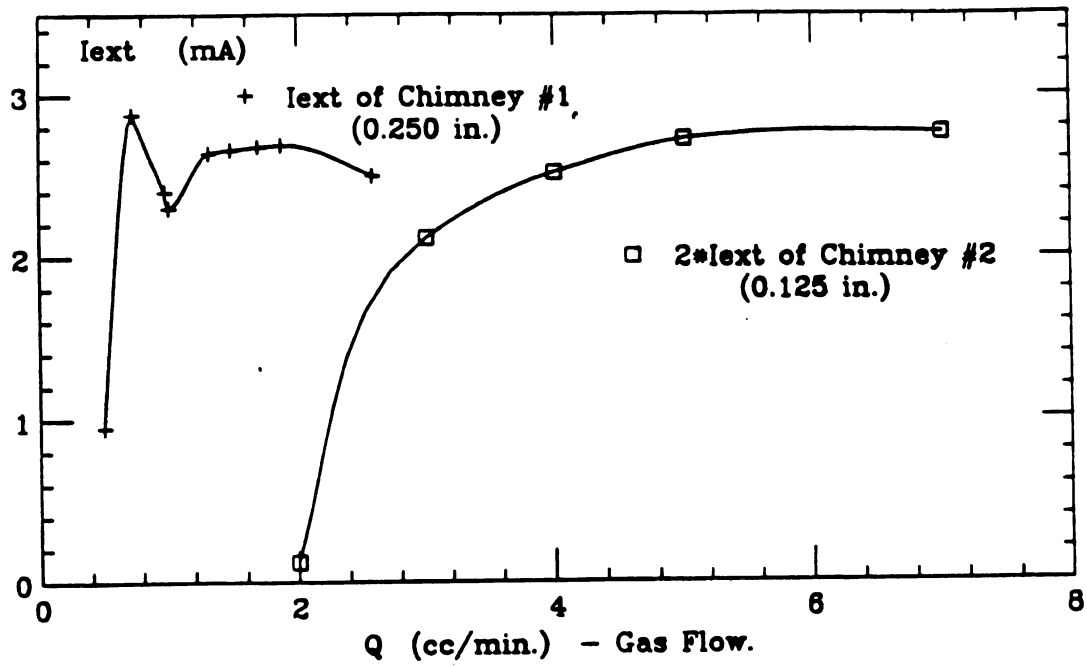


Fig. 4-13 -- Plots of I_{ext} in test #1 (0.250 in. diameter chimney) and $2I_{ext}$ in test #2 (0.125 in. diameter chimney) vs. the gas flow.

design for the 250 MeV superconducting synchrocyclotron having an enclosed ion source with a very small diameter chimney, about 0.1 in., plus a puller. The ion source for the 250 MeV superconducting synchrocyclotron could be similar to the current Harper cyclotron ion source. The experiment result answers our original question.

Chapter 5

Central Region Design

5.1 Introduction

The ion source experiment results show that a closed ion source similar to the Harper cyclotron ion source with a small diameter chimney can provide enough output ion current for the 250 MeV superconducting synchrocyclotron. Because of the strong magnetic field used in this cyclotron, there is limited space in the center for the ion source and central region electrodes. This causes difficult problems in designing a successful central region with a closed ion source. Such an ion source design is essential to provide the necessary control of the internal beam to obtain good extraction efficiency. We have obtained solutions to the central region design problems and performed the necessary orbit calculations to show the results of such a design as it affects the internal beam behavior.

Generally speaking, a successful central region design needs to meet these requirements:

(a) It should provide the maximum orbit phase acceptance. Orbits with the widest possible range of starting times should clear all the electrodes that

penetrate the median plane and the back of the source chimney.

(b) It should also provide adequate electric focusing for all of the orbits for the first few turns to avoid initial vertical beam loss, since the magnetic vertical focusing force is very weak in that region.

(c) All of the particle orbits should end up well centered after emerging from the central region, and with radial oscillation amplitudes within acceptable limits.

(d) It must allow as many particles as possible to be captured into phase-stable orbits for further acceleration out to extraction.

The procedure for determining the optimum geometry for a set of electrodes involves a converging sequence of tentative design steps, each of which is tested and improved through a combination of electric potential calculations and orbit computations. These calculations were performed to determine whether the proton orbits clear the obstacles successfully, gain energy sufficiently in the central region, receive adequate vertical focusing, and finally emerge from the central region properly centered.

5.2 Central Region Design

The overall design of our central region geometry was influenced by the central region design of the CERN 600 MeV

synchrocyclotron [32, 33]. Since our central magnetic field is about three times stronger than the CERN machine, we have a three times smaller space to use for the central region electrodes. There is one dee and dummy-dee, and we assumed a dee voltage of 20 kV. The main components of our central region design [34] are two semi-cylindrical electrodes going through the median plane in contact with the dee and dummy-dee, respectively, that define the electric field. As is shown in Fig. 5-1, the puller is fixed to the dee side electrode facing the source chimney and is inclined by 30° to the acceleration gap to provide a phase shift to the injected protons. The source chimney has outer and inner diameter of 0.125 in. and 0.095 in. The equipotentials of the electric field are also shown in Fig. 5-1.

The acceleration gap between the dee and dummy-dee provides the important electric vertical focusing force on the protons in the central region. As shown in Fig. 2-8, because the magnetic field index n is almost zero in the first few turns of the proton orbits, and the magnetic focusing force is proportional to n , the magnetic field focusing is very weak. In the initial design, the vertical dee and dummy-dee apertures were 0.6 inches, and hence symmetric about the center of the gap. However, our preliminary orbit calculations indicated that the vertical

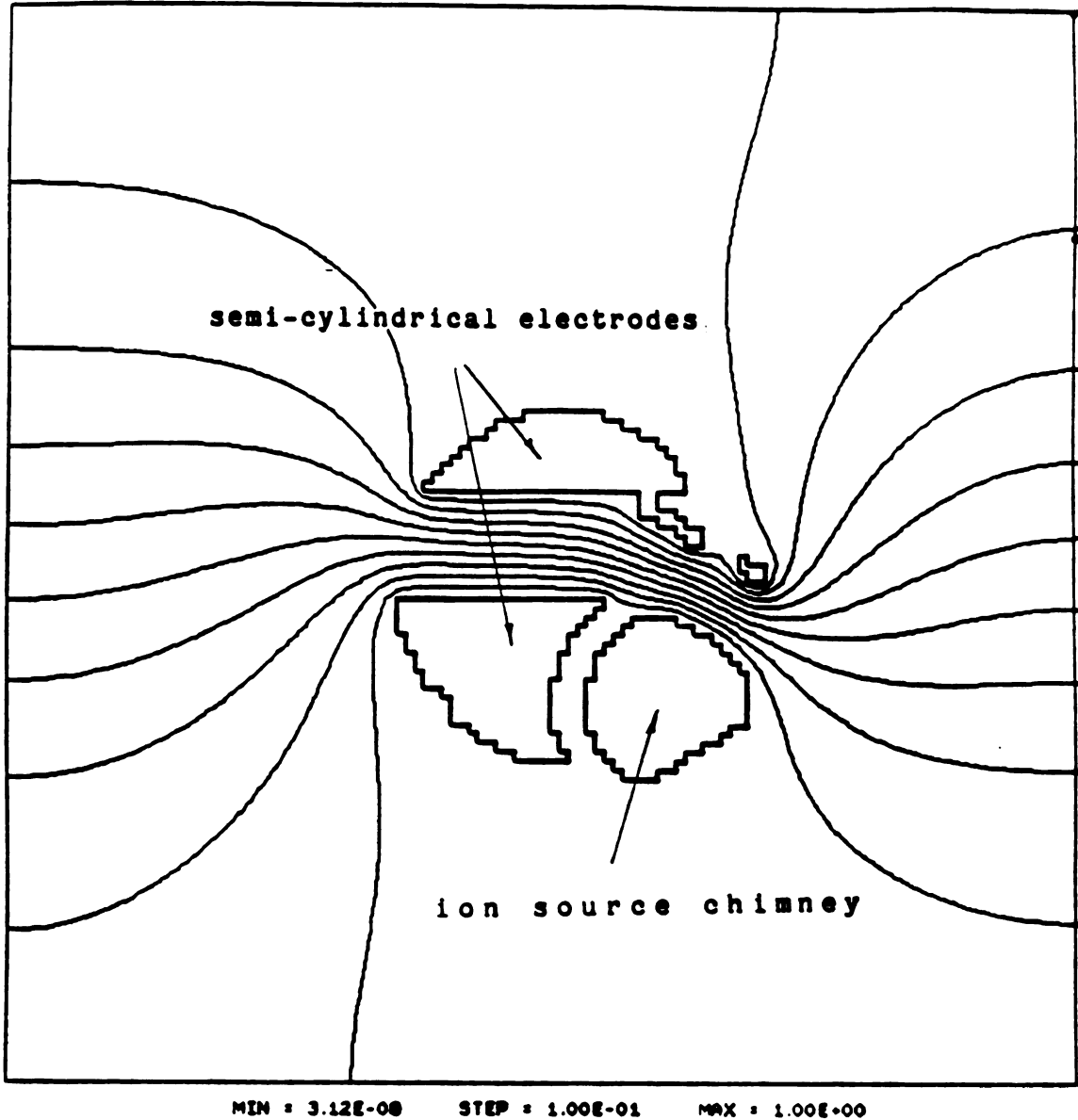


Fig. 5-1 Central region electrodes in the median plane showing the two semi-cylindrical electrodes, the puller and the ion source chimney. Also shown here are the equipotentials of the electric field produced by the central region.

focusing was not strong enough in this case, specially for the protons with early starting times τ_0 . In order to get some extra vertical focusing force, we therefore used different entrance and exit apertures of the dee and dummy-dee. As a result, the entrance aperture of the dee or dummy-dee is 0.825 in. and the exit aperture is 0.525 in. Figure 5-2 shows the acceleration gap with symmetric and unsymmetric dee and dummy-dee apertures. The unsymmetric gap design increases the vertical component of the electric field E_z in the first half of the gap (vertical focusing) and reduces it in the second half of the gap (vertical defocusing). Figures 5-3 and 5-4 show the vertical motions for protons starting at $\tau_0 = 200^\circ$ with symmetric and unsymmetric gaps. One can see from these figures the improvement of the vertical motion of the protons with the unsymmetric acceleration gap. Finally, the magnetic vertical focusing force increases rapidly with increasing radius, so the unsymmetric gap is only needed in the central region.

The gap from the source chimney to the puller and the shape of the chimney slit will greatly influence the output ion current from the source, since they determine the electric field on the surface of the plasma. Because the extracted ion current from the source is proportional to this electric field applied on the plasma surface, a high

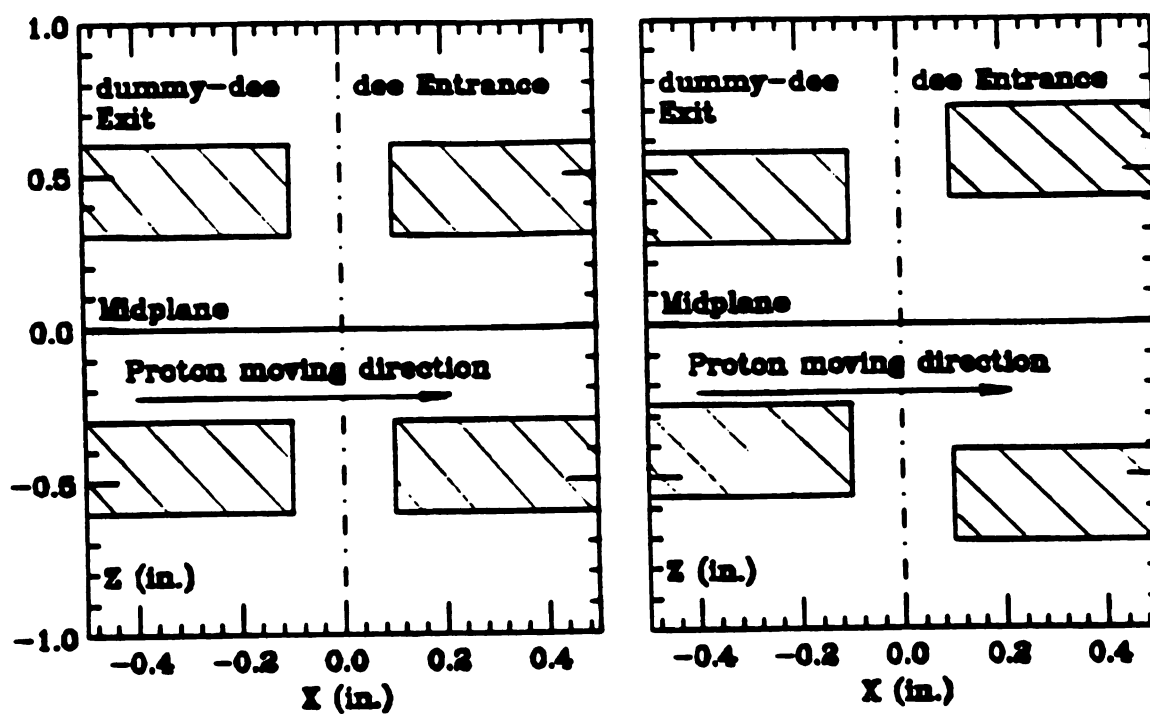


Fig. 5-2 -- Plot of cross sections of the acceleration gaps with the symmetric and unsymmetric dee and dummy-dee vertical apertures. The unsymmetric gap is only needed in the central region to provide extra vertical focusing.

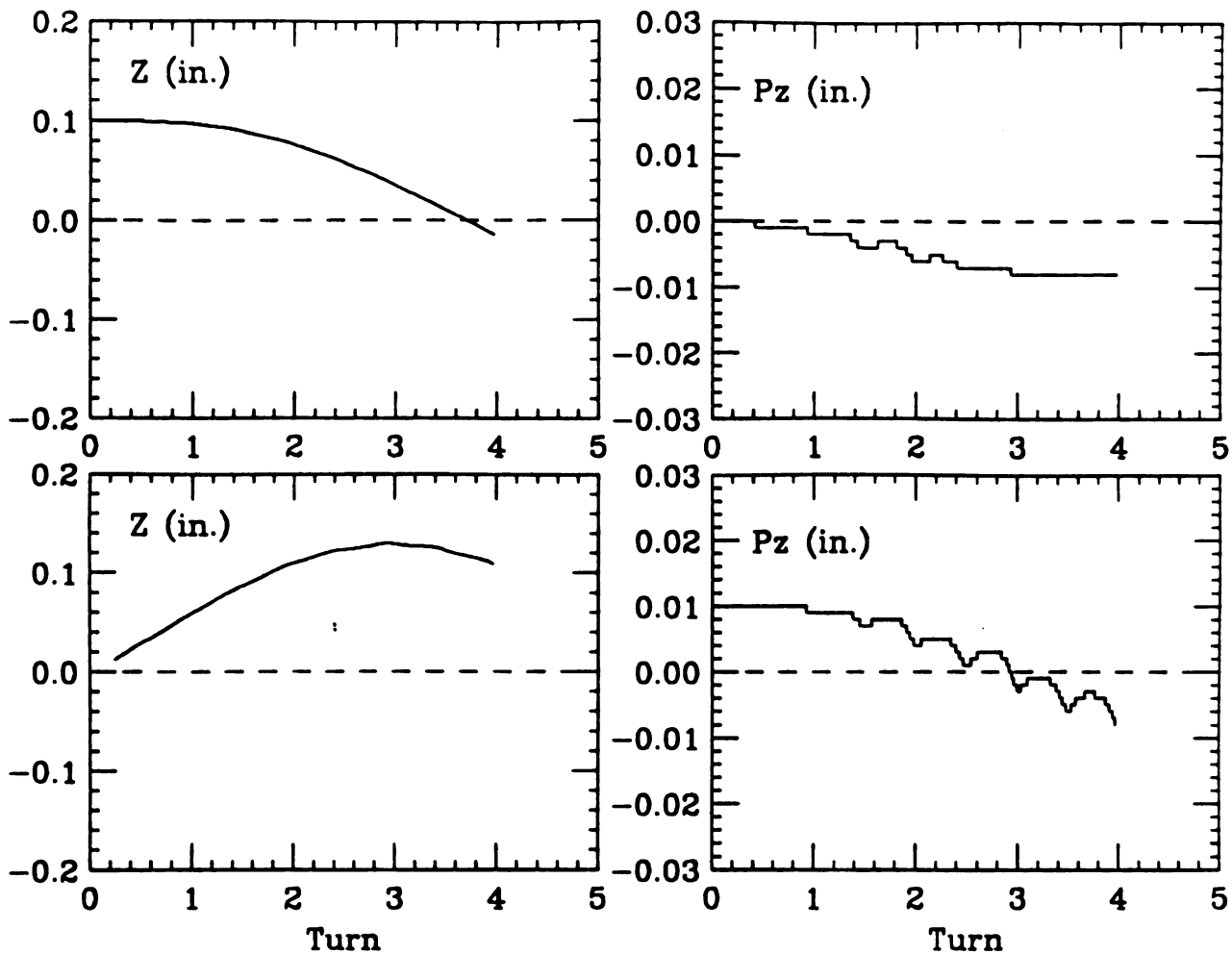


Fig. 5-3 -- Plots of z and p_z vs. Turns for the starting condition $(z, p_z) = (0.1, 0.0)$ in. at the top, and for $(z, p_z) = (0.0, 0.01)$ in. at the bottom with protons starting at $\tau_0 = 200^\circ$ at the source with symmetric acceleration gap.

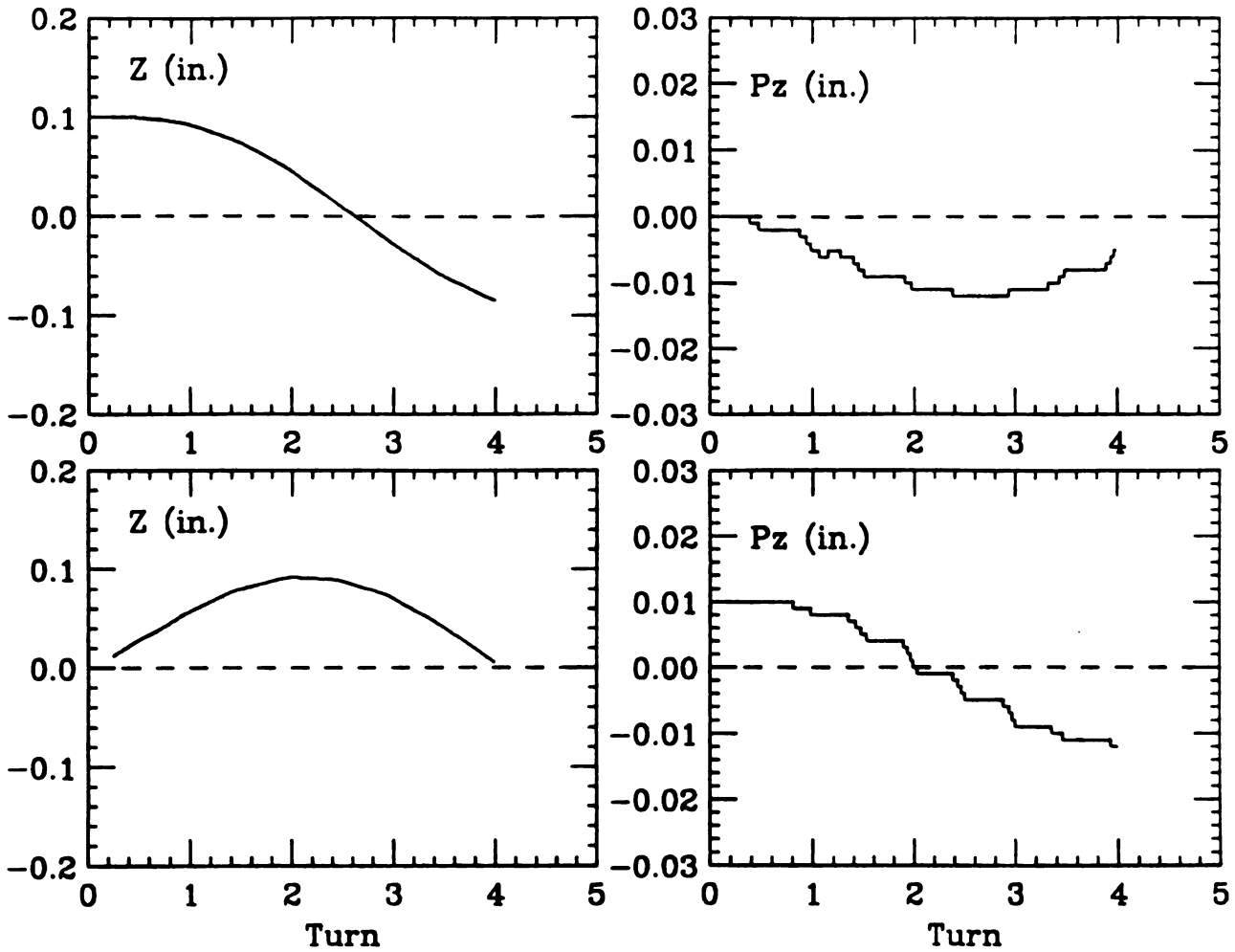


Fig. 5-4 -- Plots of z and p_z vs. Turns for the starting condition $(z, p_z) = (0.1, 0.0)$ in. at the top, and for $(z, p_z) = (0.0, 0.01)$ in. at the bottom with protons starting at $\tau_0 = 200^\circ$ at the source with unsymmetric acceleration gap. Compare with Fig. 5-3.

value of this field is desirable. One way to increase the electric field is to reduce the gap from the source to puller. The usual limit for the peak field is 100 kV/cm, and we therefore chose initially a 2 mm gap from the source to the puller which keeps the average peak electric field of 100 kV/cm with the dee voltage of 20 kV. Based on the results from the Harper cyclotron as well as other cyclotrons, the average peak electric field could reach as high as 150 kV/cm, and, moreover, a circular hole in the chimney will give a much higher output ion current than a rectangular slit, because it helps the electric field penetration into the plasma surface. We therefore reduced the gap between the source chimney and the puller from 2 mm to 1.5 mm and still kept the 2 mm gap between dee and dummy-dee. We also changed from a rectangular slit in the chimney to a circular hole with a diameter of 0.75 mm and an opening angle of 120°. Figure 5-5 and Figure 5-6 show two different designs of the source-puller region and the equipotentials of the electric fields they produced. The resultant electric field distribution along the center line of the slit before and after the change are shown in Figure 5-7. The peak electric field on the plasma surface is increased from about 63 kV/cm to 103 kV/cm. In addition, using a smaller gap also decreases the injected protons' transit time in the source to puller region.

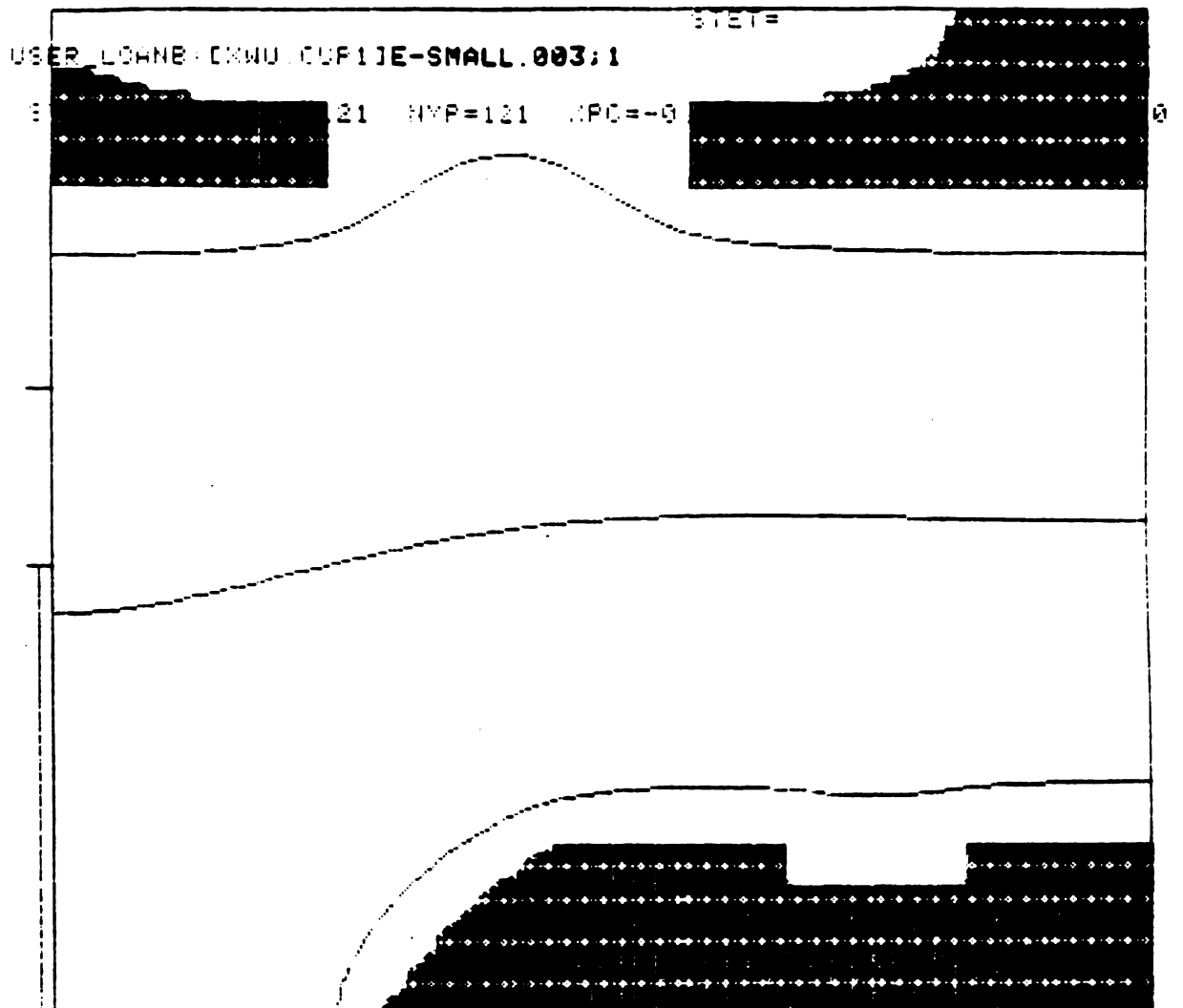


Fig. 5-5 -- Plots of the source chimney and puller electrodes in the median plane and equipotentials of the electric fields in the source-to-puller region. The gap from the chimney to the puller is 2 mm, and a 4.0 by 0.5 mm² rectangular slit was used in this case.

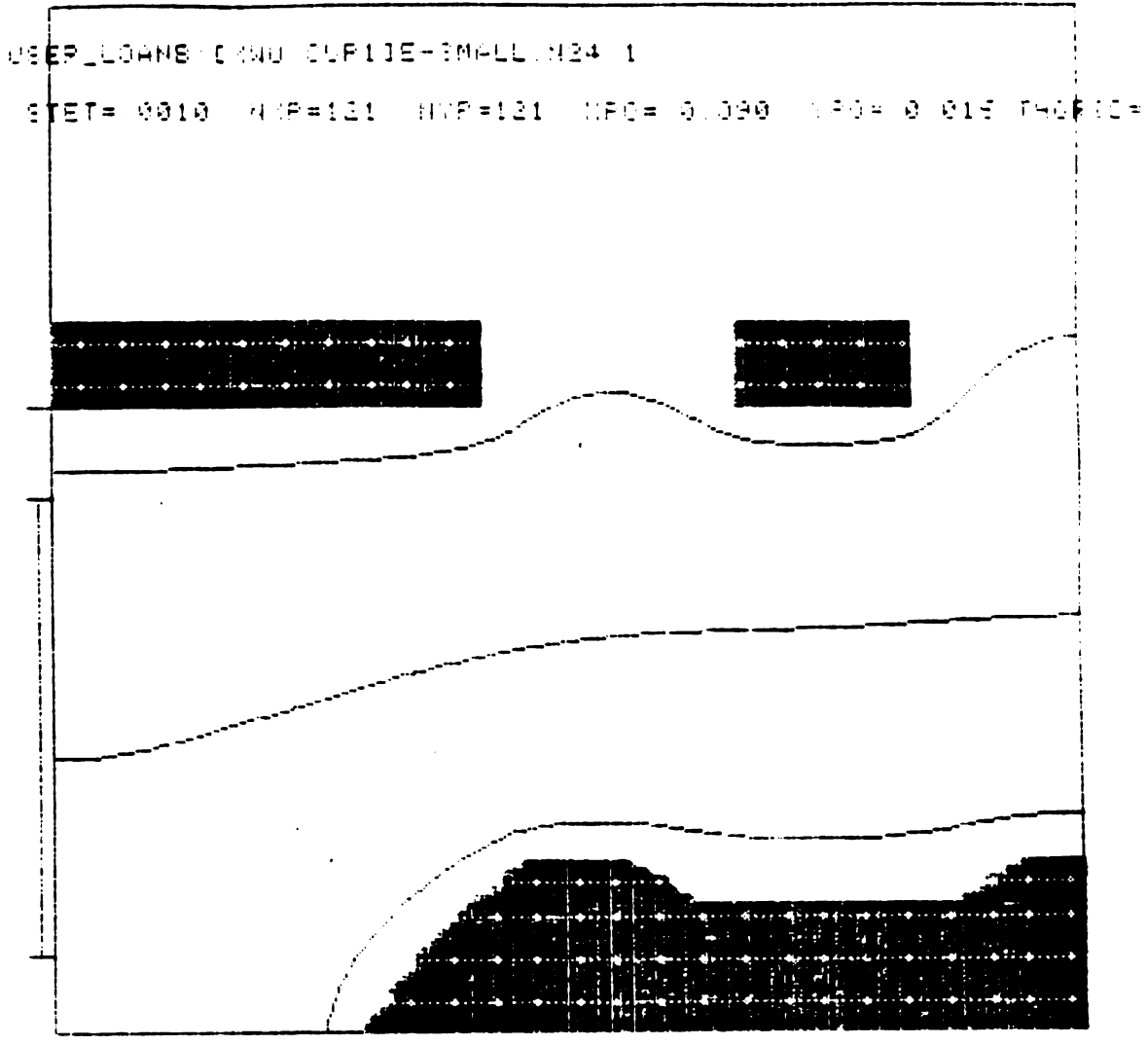


Fig. 5-6 -- Plots of the source chimney and puller electrodes in the median plane and equipotentials of the electric fields in the source-to-puller region. The gap from the chimney to the puller is 1.5 mm, and a 0.75 mm diameter circular slit with an opening angle of 120° has been used in this case.

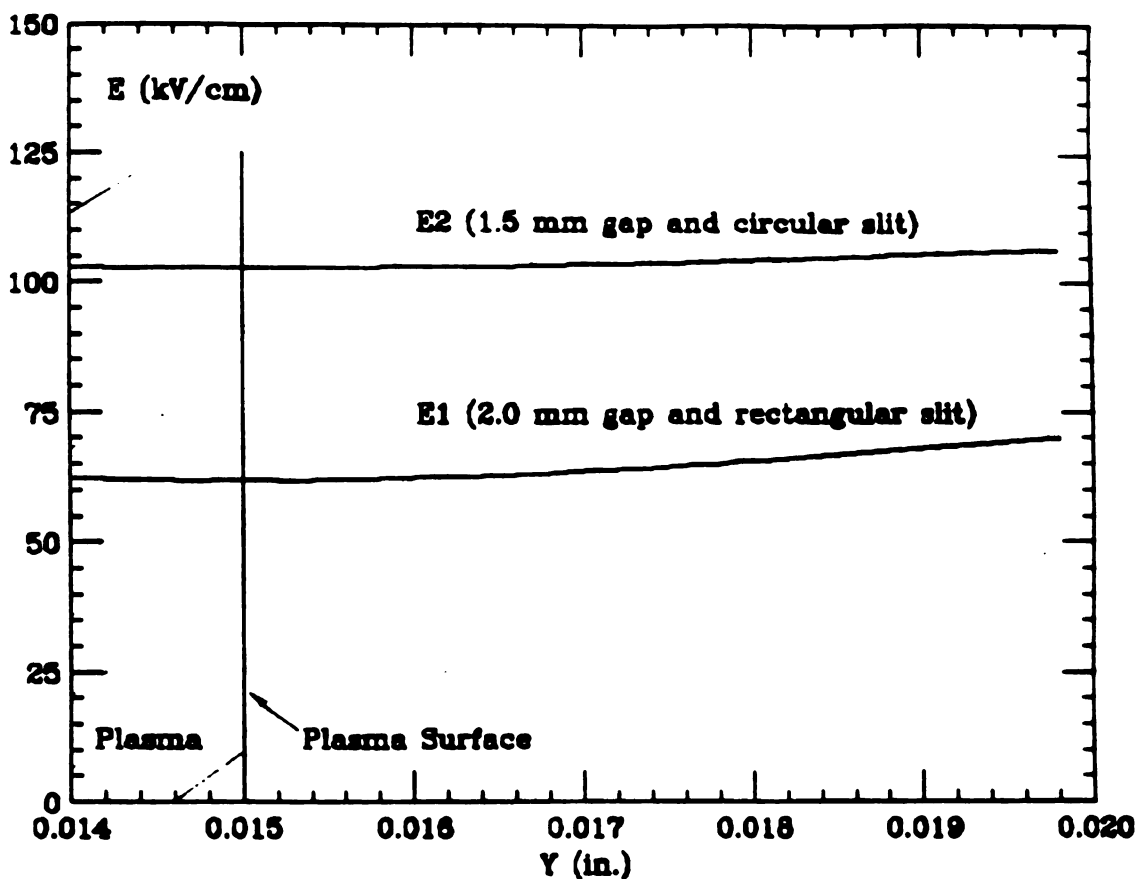


Fig. 5-7 -- Plot of the electric field distribution near the center of the chimney slit for two different cases shown in Figs. 5-5 and 5-6, one with a 2 mm source-to-puller gap and a 4 by 0.5 mm² rectangular slit, and the other with a 1.5 mm gap and a circular hole with diameter of 0.75 mm and an opening angle of 120°. The voltage is 20 kV.

5.3 Field and Orbit Calculations

Our 3-D CYCLONE orbit code [35] was used to design the electrode structures in the central region of the 250 MeV superconducting synchrocyclotron and perform the orbit calculations, tracking ion orbits starting from the ion source and going out about 20 turns. This code calculates the real z motion in the central region. Since this code assumes a constant RF frequency, we used only the first two parts.

Part I takes the ion from the source slit out to just beyond the puller. The electric field in the source-to-puller region is derived from a potential $V(x,y,t) = U_0(x,y)\sin\omega_{rf}t$, where the $U_0(x,y)$ map is prepared with the TRIUMF RELAX3D4 Code and ω_{rf} is the constant RF frequency. The grids used in the TRIUMF's RELAX3D4 code for this small electric field are 121 by 121 points with a square mesh size of 0.001 in. The orbit computations in this part of the program are carried out by integrating the equation of motion in Cartesian coordinates with time t as the independent variable. Part I do not include z motion.

Part II continues the orbit for a few turns until it reaches $r \approx 0.9$ inches. The large electric field here is derived from $V(x,y,z,t) = U_1(x,y,z)\sin\omega_{rf}t$, where the $U_1(x,y,z)$ map is also prepared with the same RELAX3D4 Code.

The grids used in the RELAX3D4 code for this large electric field are 121 by 121 by 12 points, and two different mesh sizes of 0.0066 in. and 0.015 in. are used with planes parallel to the median plane 0.0375 inches apart. The orbit computations in part II of the program use θ as the independent variable so that r , p_r , z , p_z , t and energy E are the particle coordinates. The code also includes the real z motion calculations since it uses a 3-D electric field in this part.

All parts of the CYCLONE code use the same median plane magnetic field $B(r,\theta)$ which is stored in a polar mesh with $\Delta\theta = 1.0$ degree, and $\Delta r = 0.25$ in. The magnetic field design was discussed in chapter 2 and chapter 3 of this dissertation. It provides an absolute reference frame for positioning all of the electrodes and the resultant electric fields used in the 3-D CYCLONE code.

The first part of the orbit calculations was performed using Parts I and II of the CYCLONE code. Since the initial energy of the protons extracted from the internal ion source is very small, the space-charge effects are dominant in the source-to-puller region. Moreover, CYCLONE is a single particle orbit tracking code and do not include z motion in its first part. We therefore performed the median plane orbit calculations in the source-to-puller region and added

z motion after protons passing the puller assuming proton beam having a certain vertical size. However, M. Mallory and H. Blosser [42] have studied radial and vertical emittances from the ion source and the effects of the plasma boundary and space-charge. Their results show the assumption made here for the initial z ellipse is reasonably good, giving results that agree with the experimental measurement. Since the RF frequency changes with time in synchrocyclotrons, a transfer matrix code has been developed and used to continue the orbit computations after the first few turns. This transfer matrix code is described in section 5.5.1 and the equations used in this code is described in Appendix C.

5.4 Orbit Properties and Discussion

The central ray starting time $\tau_0 = 230^\circ$ has the maximum energy gain in the acceleration from source-to-puller while the peak electric field is reached at $\omega_{rf}t = 270^\circ$ where ω_{rf} is the constant RF frequency. In Figure 5-8, we have plotted eight orbits for protons starting at $\tau_0 = 200^\circ$ to 265° in the small electric field of the source-puller region. In Fig. 5-9, we have a similar plot in the large electric field for the first few turns. All the orbits plotted clear the puller electrode and gain enough energy after the first two gaps to clear the posts and the back of

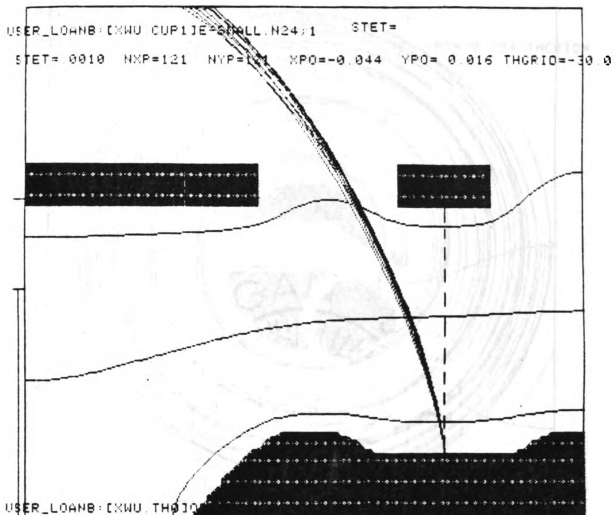


Fig. 5-8 -- Source chimney and puller electrodes, and median plane equipotentials for the small electric field. Eight orbits are plotted, corresponding to starting time $\tau_0 = 200^\circ$ to 265° . The peak electric field between source and puller is achieved at $\tau = \omega_{rf} t = 270^\circ$. The central ray starting time is $\tau_0 = 230^\circ$.

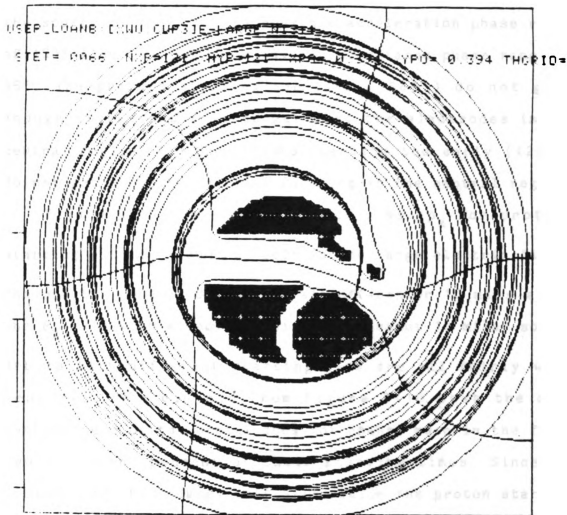


Fig. 5-9 -- Central region electrodes and median plane equipotentials for the large electric field. Eight orbits are plotted, corresponding to starting time $\tau_0 = 200^\circ$ to 265° . The orbit closest to the lower right electrode is starting at $\tau_0 = 265^\circ$ and the one far away from the electrode is starting at $\tau_0 = 230^\circ$, the starting time which gives the maximum energy gain in the source-to-puller gap.

the source chimney. Of the possible acceleration phase range of 180° (180° to 360°), we have an acceptance phase range of 65° . The protons starting too late ($>265^\circ$) do not gain enough energy and fail to get past the electrodes in the central region, and the protons starting too early ($<200^\circ$) do not get adequate vertical focusing in the central region.

Figure 5-10 shows the plots of x vs. p_x for protons starting with $\tau_0 = 200^\circ$ to 260° in the large electric field. The orbits here at $\theta = 0^\circ$ are all off-center 10 mils along the P_x axis with a radial amplitude of about 10 mils, so the orbits with different starting time are all fairly well centered. One can see from Figure 5-10 that the off-centeredness of the orbits does not change much in the first few turns independent of their starting times. Since the location of the chimney slit will decide the proton starting positions, and hence the initial centering error, it has a strong influence on the final centering error at extraction. The central region electrodes must therefore be accurately positioned.

Figure 5-11 shows the average phases ϕ_{av} for the first 20 turns for protons starting at $\tau_0 = 200^\circ$ to 265° , where

$$\phi_{av} = \phi + \left(\frac{360^\circ}{2\pi}\right)\frac{P}{P}x \quad \text{and } \phi \text{ is phase of the protons to deal}$$

with the coupling between the radial and longitudinal

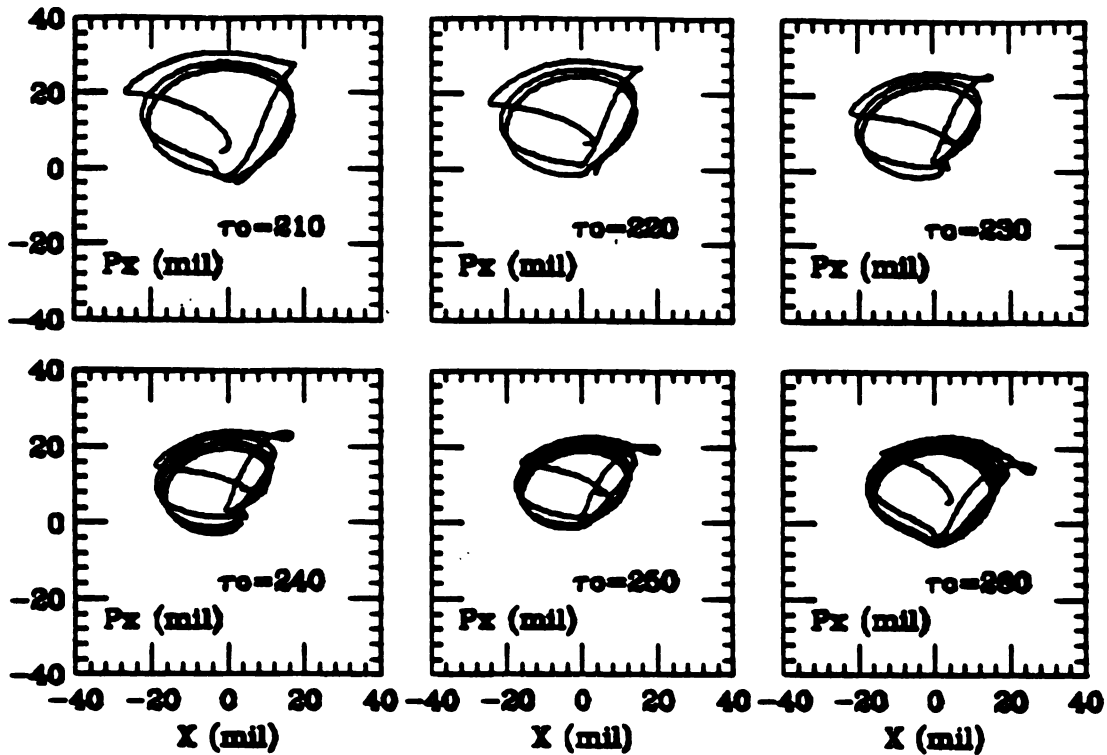


Fig. 5-10 -- Plots of x vs. p_x for protons starting at $\tau_0 = 200^\circ$ to 260° in the large electric field. The orbits all deviate from the equilibrium orbit by 10 mils along the P_x axis with a radial amplitude of about 10 mils, so the orbits with different starting time are all well centered.

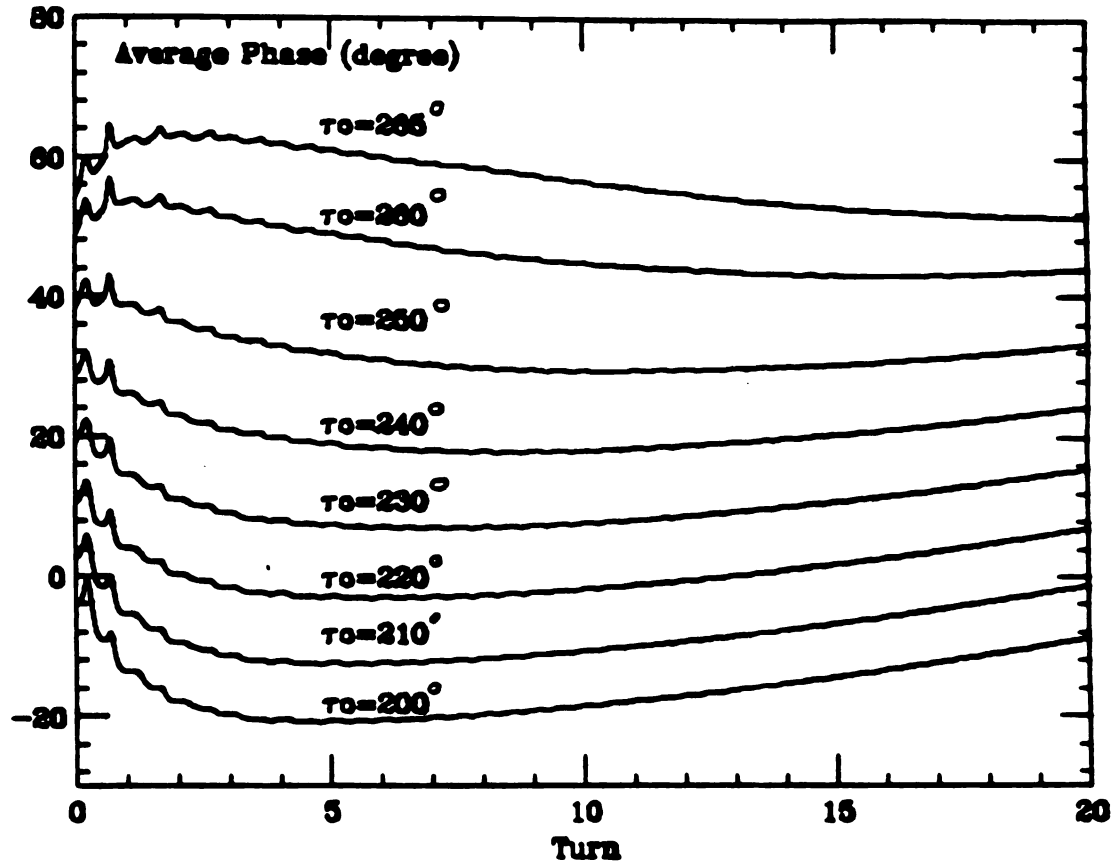


Fig. 5-11 -- Plot of average phase ϕ_{av} vs. Turns for protons starting at $\tau_0 = 200^\circ$ to 265° for the first 20 turns. They depends strongly on the proton starting time τ_0 .

motion [41]. The average phase curve depends strongly on the starting time τ_0 . Since the average electric focusing force is proportional to $\sin(\phi)$, the vertical motion of the protons also depends strongly on the starting time τ_0 .

Figures 5-12 shows the vertical motions for the starting condition $(z, p_z) = (0.1, 0.0)$ at the top, and for $(z, p_z) = (0.0, 0.01)$ at the bottom for protons starting at $\tau_0 = 200^\circ$. In Figs. 5-13 and 5-14, we have similar plots for protons starting at $\tau_0 = 230^\circ$ and 260° . We observe from these plots the strong dependence of the vertical focusing frequency on the protons' starting time τ_0 . The vertical oscillation amplitude for all three orbits does not increase significantly for the first 20 turns. Since the electric focusing is only important for the first few turns of the orbits and magnetic focusing becomes dominant afterwards, the vertical focusing requirement is satisfied for these cases.

The above calculations were carried out for an RF frequency $\omega_{rf} = \omega_0 = \frac{eB(0)}{m}$, where $B(0)$ is the field at $r=0$. However, the RF frequency decreases with time in synchrocyclotrons, and protons start from the source on every RF cycle. To allow for this, the CYCLONE program input

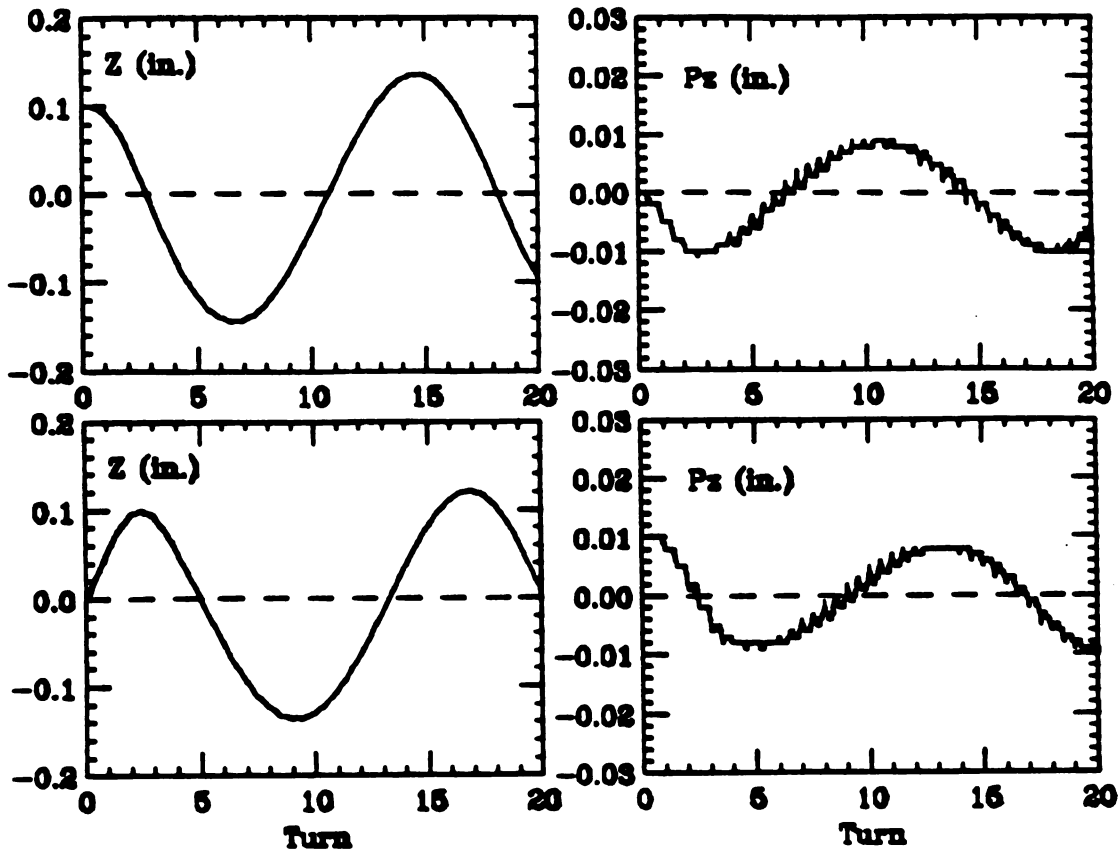


Fig. 5-12 -- Plots of z and p_z vs. Turns for the starting condition $(z, p_z) = (0.1, 0.0)$ in. at the top, and for $(z, p_z) = (0.0, 0.01)$ in. at the bottom with protons starting at $\tau_0 = 200^\circ$ at the source.

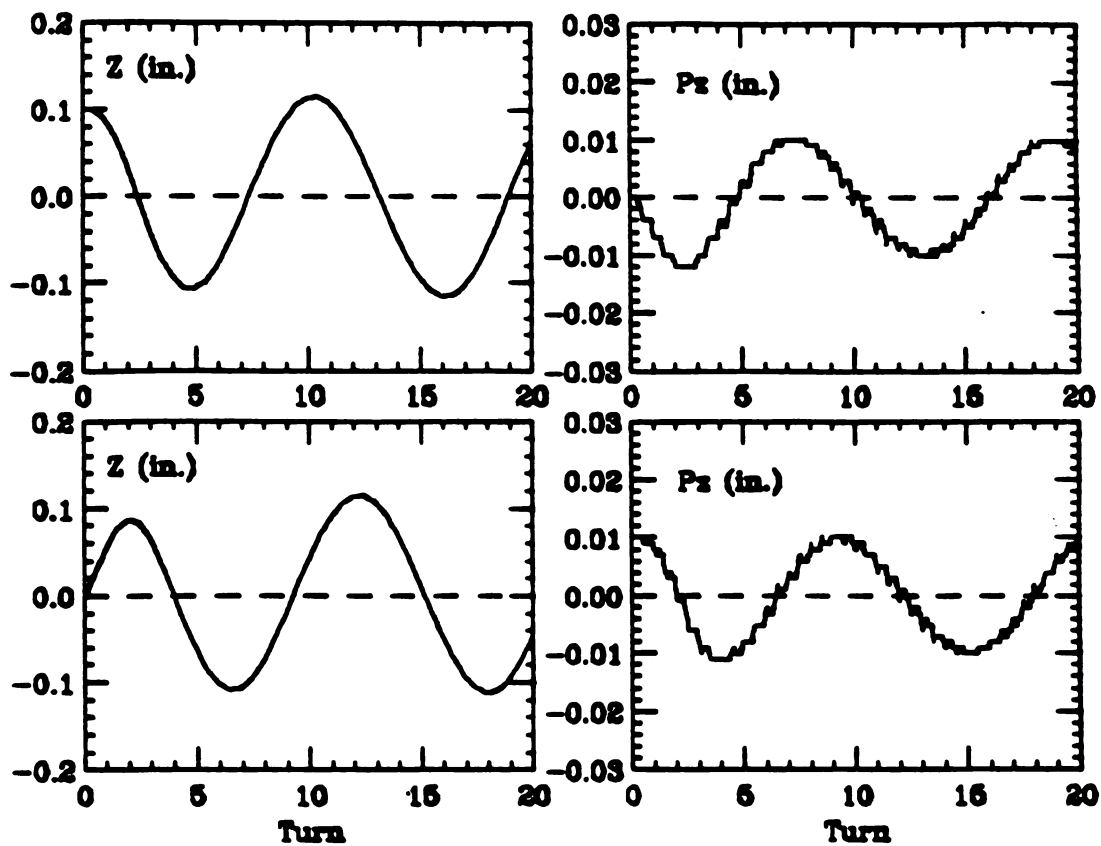


Fig. 5-13 -- Plots of z and p_z vs. Turns for the starting condition $(z, p_z) = (0.1, 0.0)$ in. at the top, and for $(z, p_z) = (0.0, 0.01)$ in. at the bottom with protons starting at $\tau_0 = 230^\circ$ at the source. Compare with Fig. 5-12.

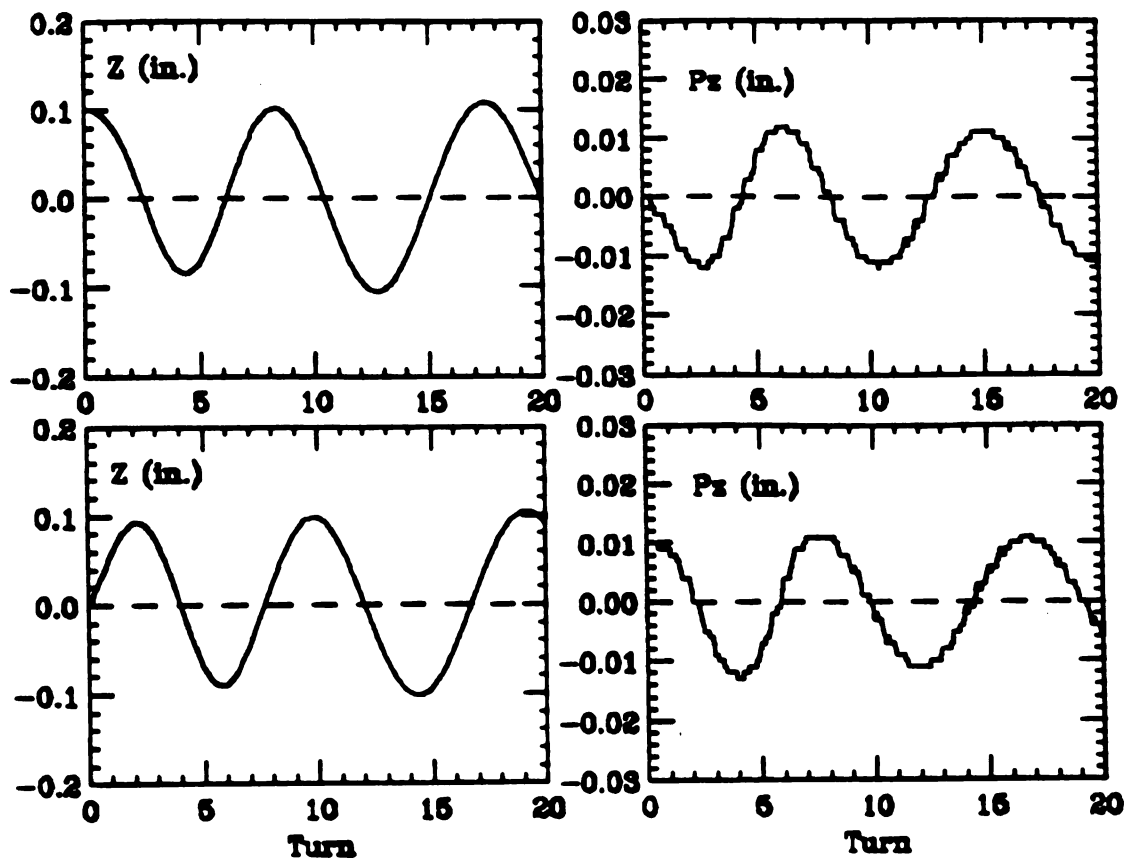


Fig. 5-14 -- Plots of z and p_z vs. Turns for the starting condition $(z, p_z) = (0.1, 0.0)$ in. at the top, and for $(z, p_z) = (0.0, 0.01)$ in. at the bottom with protons starting at $\tau_0 = 260^\circ$ at the source. Compare with Fig. 5-12 for $\tau_0 = 200^\circ$ and with Fig. 5-13 for $\tau_0 = 230^\circ$.

sets $\omega_{rf} = \omega_0(1+\epsilon)$, where ϵ is a parameter. The capture-time calculations described below lead to an optimum value for the initial frequency time derivative that restricts the values of ϵ between zero and $\epsilon = -0.007$.

The orbit computations described above were therefore repeated with $\epsilon = -0.007$, the lower boundary for the initial frequency parameter. As expected, the results obtained on clearing electrode structures during the first turn do not change. Also, the results regarding orbit centering during the first 20 turns are pretty much the same. However, values of the average phase and the resultant vertical focusing change significantly. That is, for starting times τ_0 below 215° , the vertical focusing is inadequate. Considering these results, the overall phase acceptance range is decreased to about 50° , corresponding to τ_0 values from 215° to 265° . Of course, these calculations neglect the defocusing effect of the space-charge forces which are important at low energies.

5.5 Capture Time Calculations

As defined by Bohm and Foldy [36], the capture time Δt for a given starting time τ_0 is given by

$$\Delta t(\tau_0) = \frac{\Delta\omega(\tau_0)}{-\left(\frac{d\omega}{dt}\right)_i},$$

where $\Delta\omega(\tau_0)$ gives the range of initial frequency values leading to the eventual capture into phase stable orbits of protons with starting time τ_0 which do not return to the center during the first phase oscillation, and $-(\frac{d\omega}{dt})_i$ is the initial RF frequency time derivative assumed in the calculation. With a frequency modulation rate f_m , the corresponding synchrocyclotron beam current [37, 38] is then given by

$$I = I_c f_m \Delta t ,$$

where I_c is the corresponding cyclotron beam current and Δt is the over-all capture time. The transfer matrix program was used to continue the orbit calculations described above beyond the first five turns and hence to determine the capture time for each value of $-(\frac{d\omega}{dt})_i$.

5.5.1 Transfer Matrix Program

As noted above, the transfer matrix code is described in the Appendix C. It starts with the output of part II of the CYCLONE code and carries the orbits through enough turns to determine whether they successfully execute phase oscillations and do not return to the ion source vicinity. It enables one to find the value of the initial frequency time derivative that leads to the maximum capture time.

Assuming a linear variation of the RF frequency, we can write:

$$\begin{aligned}\omega_{rf} &= (1+\epsilon)\omega_0 + 2\pi\left(\frac{df}{dt}\right)t \\ &= (1+\epsilon-\lambda f_0 t)\omega_0 ,\end{aligned}$$

where $\lambda = -\frac{1}{f_0^2}\left(\frac{df}{dt}\right)$ and $\omega_0 = 2\pi f_0 = \frac{e}{m}B(0)$ is the reference frequency.

For each value of the parameter λ used, one can then run the Transfer Matrix code to find the range of ϵ values that produce phase stable particles for each starting time τ_0 which do not return to the center during the first synchrotron phase oscillation,

$$\Delta\epsilon(\tau_0) = \epsilon_1 - \epsilon_2$$

where ϵ_1 and ϵ_2 are the ϵ range boundaries. Therefore, the corresponding range of starting frequency values will be:

$$\Delta\omega(\tau_0) = \Delta\epsilon(\tau_0)\omega_0.$$

We can then calculate the corresponding capture time,

$$\Delta t(\tau_0) = \frac{\Delta\omega(\tau_0)}{-\left(\frac{d\omega}{dt}\right)_i} = \frac{\Delta\epsilon(\tau_0)\omega_0}{-\left(\frac{d\omega}{dt}\right)_i}$$

so

$$\begin{aligned}\Delta t(\tau_0) &= \frac{\Delta\epsilon(\tau_0)}{f_0\lambda} = \left(-\frac{\epsilon_2}{f_0\lambda}\right) - \left(-\frac{\epsilon_1}{f_0\lambda}\right) \\ &= T_2 - T_1\end{aligned}$$

where $T_1 = -\frac{\epsilon_1}{f_0 \lambda}$ and $T_2 = -\frac{\epsilon_2}{f_0 \lambda}$ are the time boundaries for capture of phase stable particles of starting time τ_0 which will not return to the center during the first synchrotron phase oscillation.

To determine the corresponding synchronous phase ϕ_s for a given λ value, we use the simple theory of phase oscillations [58] which leads to the formula:

$$\lambda = K \left(\frac{\omega}{\omega_0} \right)^2 \left(\frac{2eV_d}{E} \right) \cos \phi_s$$

where
$$K = -\frac{E}{\omega} \left(\frac{d\omega}{dE} \right) = 1 + \frac{n}{B^2(1-n)}$$

with
$$n = -\frac{r}{B} \left(\frac{dB}{dr} \right),$$

being the magnetic field index. Also, V_d is the dee voltage so that $2eV_d$ is the peak energy-gain per turn.

5.5.2 Capture Time Calculation Results

The transfer matrix program was used to continue the orbits for the first 1000 turns with starting times τ_0 from 210° to 265° and an interval $\Delta\tau_0 = 5^\circ$. Values of the initial frequency time derivative $\left(-\frac{df}{dt}\right)_i$ ranging from 20 MHz/ms to 150 MHz/ms were used in the calculations in order to find

the maximum over-all capture time. For a successfully captured orbit, the energy will show an oscillation superimposed on a steady increase and, moreover, the energy will never fall below a given critical value E_c , which corresponds to an orbit radius of 0.3 in.

Figures 5-15 and 5-16 show the distributions of T values defined above vs. proton starting time τ_0 obtained for different initial RF frequency time derivative values. As can be seen, more orbits with late starting times τ_0 are captured than those with early starting times. This effect is much more obvious if a smaller initial frequency time derivative $(-\frac{df}{dt})_1$ is used. Since the initial electric field between the ion source and the puller is proportional to $\sin(\tau_0)$, the source output current is proportional to $\sin(\tau_0)$ as well. The average capture time for all available starting times τ_0 is finally determined by:

$$\Delta t_{av} = \frac{\sum \Delta t(\tau_{0j}) |\sin(\tau_{0j})|}{\sum |\sin(\tau_{0j})|} .$$

As defined by Bohm and Foldy [36], the capture efficiency ϵ_c is

$$\epsilon_c = f_m \Delta t_{av}$$

where f_m is the modulation frequency.

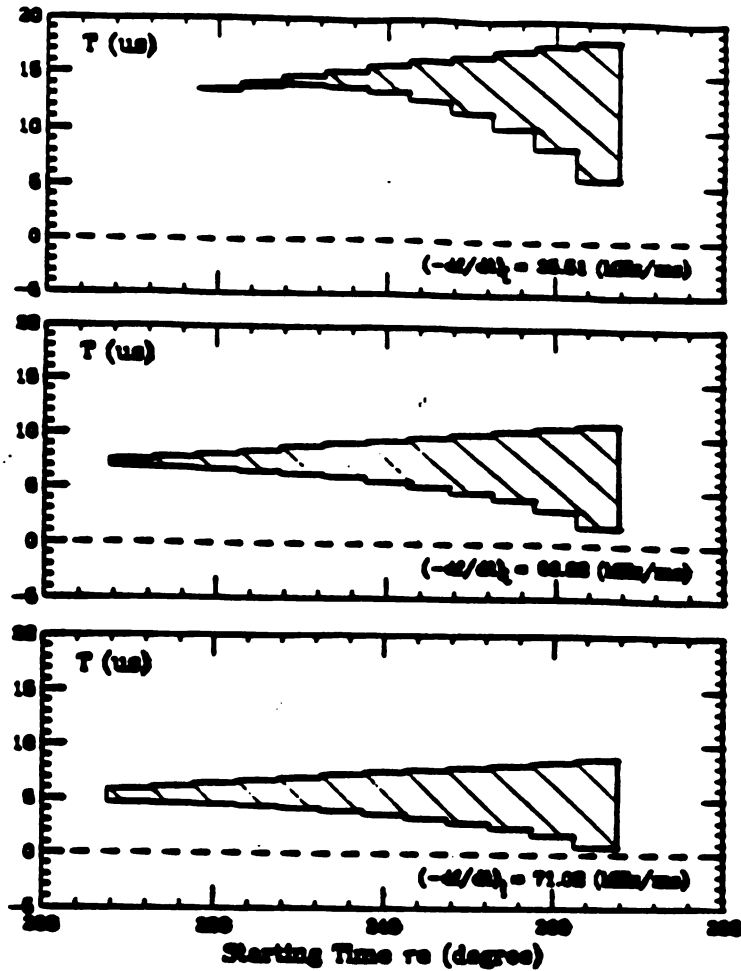


Fig. 5-15 -- Plots of the distributions of T values vs. proton starting time τ_0 with initial $(-\frac{df}{dt})_1$ of 35.51, 56.62 and 71.02 MHz/ms. Only the proton orbits inside the shaded area in the plots will be captured and accelerated to extraction.

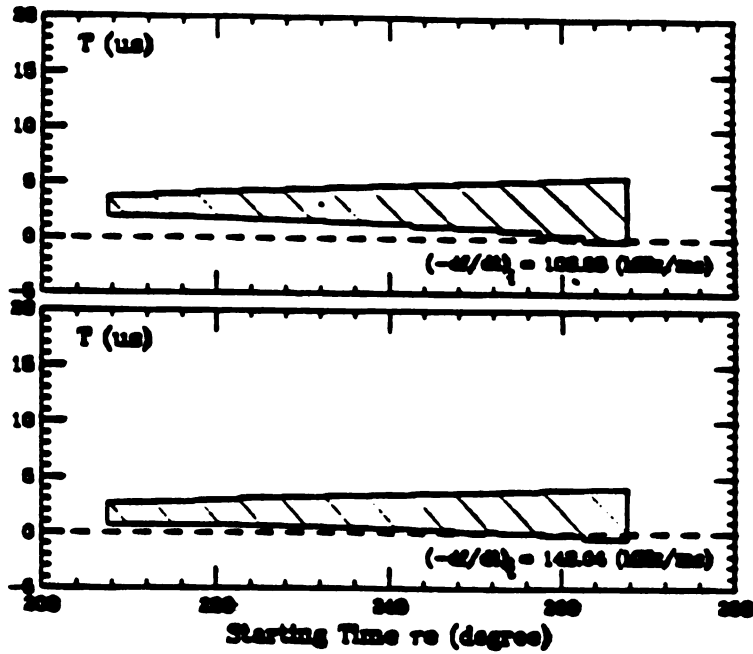


Fig. 5-16 -- Plots of the distributions of T values vs. proton starting time τ_0 with initial $(-\frac{df}{dt})_1$ of 106.53 and 142.04 MHz/ms. Only the proton orbits inside the shaded area in the plots will be captured and accelerated to extraction. Compare with Fig. 5-15.

Table 5-1 shows the capture time and capture efficiency calculation results. Of course, high modulation frequencies result in better capture efficiencies, but the values are limited by practical considerations. For application to proton cancer therapy, the proposed RF modulation frequency f_m is 1 kHz. This high value can not be achieved using traditional methods such as vibrating plates or rotating capacitors. A new RF system using electronic tuning has to be designed to provide 1 kHz modulation frequency with an RF frequency range of 61.75 MHz to 84.27 MHz.

Table 5-1

$\lambda_i (10^{-6})$	$(-\frac{df}{dt})_i$ (MHz/ms)	$\cos\phi_{si}$	Δt_{av} (μ s)	ϵ_c (%)
5.0	35.510	0.0523	4.212	0.42
6.0	42.612	0.0628	4.401	0.44
7.0	49.714	0.0733	4.489	0.45
8.0	56.816	0.0837	4.481	0.45
9.0	63.917	0.0942	4.423	0.44
10.0	71.019	0.1047	4.324	0.43
15.0	106.529	0.1570	3.734	0.37
20.0	142.039	0.2093	3.189	0.32

Figure 5-17 shows the average capture time as a function of initial frequency time derivative $(-\frac{df}{dt})_i$ and the initial value of $\cos\phi_s$. The average capture time reaches its maximum value of 4.5 μ s at $(-\frac{df}{dt})_i$ of 49.71 MHz/ms and $\cos\phi_{s1} = 0.073$, but the maximum is fairly flat. Since the initial energy gain of the protons is proportional to $\cos\phi_{s1}$, a larger $\cos\phi_{s1}$ is desired to get a better initial energy gain. One can see from Fig. 5-17 and Table 5-1 that we can obtain a good initial energy gain and still have an average capture time of 4.3 μ s, which is close to the peak value, with $\cos\phi_{s1} = 0.105$.

Several different magnetic fields have been used to perform the capture time calculations in order to check the magnetic field influence on the capture time and hence find the optimum magnetic field shape which leads to the maximum capture time. The results show that the capture time depends strongly on the magnetic field shape in the center. Larger $K = (-\frac{Ed\omega}{\omega dE})$ values in the center result in higher capture times, which agrees with the results found at CERN [32, 33, 39]. In the ion source experiment described in chapter 4, we found a peak DC current of about 1.8 mA from the ion source. Since the charge injected during each RF cycle occupies

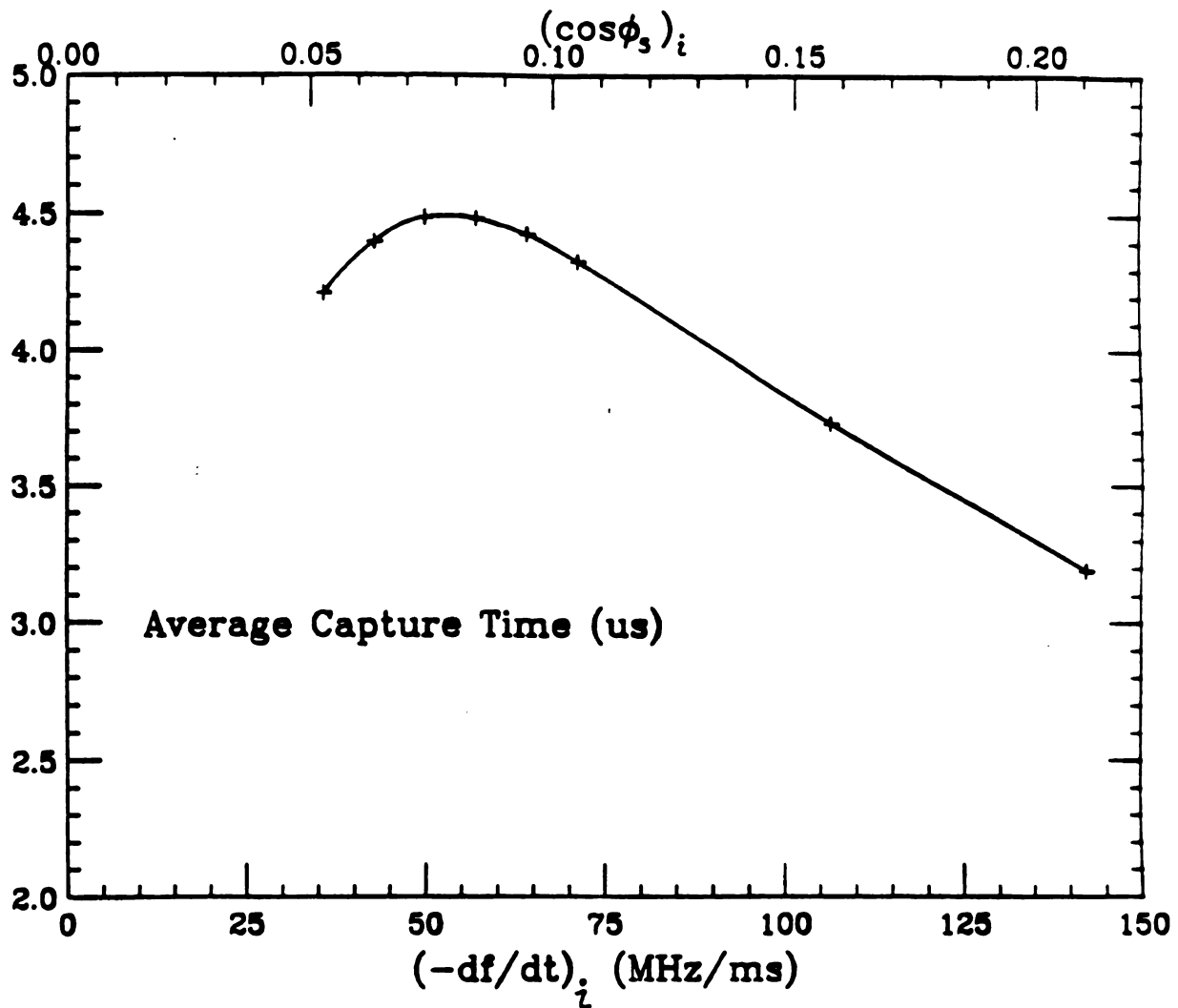


Fig. 5-17 -- Plot of average capture time Δt_{av} vs. initial frequency time derivative $(-df/dt)_i$ together with the corresponding value of $\cos \phi_{s1}$ where ϕ_{s1} is the initial synchronous phase.

about 50° in phase, the corresponding current for a fixed frequency cyclotron would be

$$I_c = I_o \left(\frac{50}{360} \right) = (1800 \mu\text{A}) \left(\frac{50}{360} \right) = 250 \mu\text{A}.$$

Assuming the capture efficiency $\epsilon_c = 0.43\%$ from Table 5-1, we find the corresponding synchrocyclotron beam current to be

$$I_{sc} = I_c f_m \Delta t_{av} = I_c \epsilon_c = 1.1 \mu\text{A}.$$

Since only $0.1 \mu\text{A}$ of extracted beam current is required, this $1.1 \mu\text{A}$ seems quite adequate to withstand subsequent losses and yield enough output current.

Chapter 6

RF Frequency Program

6.1 Introduction

Once a proton orbit is successfully captured in the central region, it will stay inside the phase stability region and be accelerated all the way to the extraction system unless the stability region becomes smaller during the acceleration, and the phase oscillation amplitude of the orbit is too large to fit in the new stability region. Since the phase space volume occupied by the protons does not change, it is necessary to keep a constant stability region during the acceleration in order to avoid the loss of protons. This requirement can be fulfilled by changing the frequency time derivative during the acceleration. Two possible RF frequency programs to meet this requirement have been explored: one keeps the dee voltage V_d constant, the other keeps the average energy-gain per turn constant for protons at large radii. Our analysis here follows closely that presented by Kullander [33,37].

The longitudinal phase space variables are the phase ϕ of the particle and its energy displacement from the

synchronous particle, $\Delta E = E - E_s$. This phase space is characterized by a closed stable and an open unstable region separated by the separatrix. Along this separatrix, the value of ΔE is given by

$$\Delta E = \left(\frac{2eV_d E_s}{\pi K} \right)^{1/2} F^{1/2}(\phi, \phi_s),$$

where $F(\phi, \phi_s) = \sin\phi + \sin\phi_s - (\phi + \phi_s)\cos\phi_s$, and $K = -\frac{E}{\omega} \left(\frac{d\omega}{dE} \right)$, as before.

Figure 6-1 shows the three phase space separatrices corresponding to $\cos\phi_s$ of 0.05, 0.1 and 0.3. The "bucket" areas inside the separatrices are the particle phase stable regions for these cases. A small $\cos\phi_s$ value leads to a larger stable bucket area, but a slower acceleration rate.

The normalized bucket area A is defined by

$$A = \int F^{1/2}(\phi, \phi_s) d\phi$$

and is a unique function of the synchronous phase ϕ_s . Figure 6-2 shows the plot of the normalized bucket area A vs. $\cos\phi_s$.

Since the real stable bucket area S in the $(\Delta E, t)$ phase space is

$$S = \int \Delta E dt = \int \Delta E \frac{d\phi}{\omega_s},$$

substitution of ΔE given above leads to

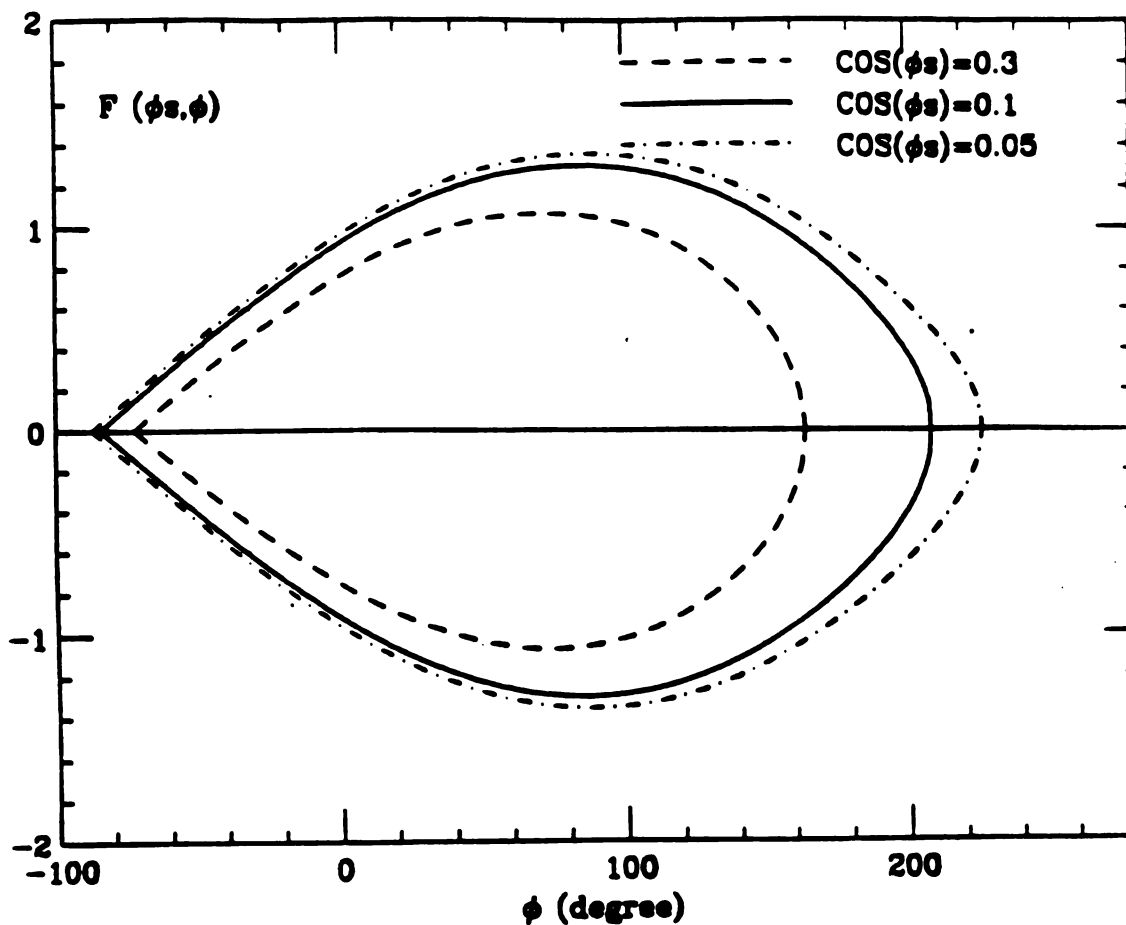


Fig. 6-1 -- Three Phase space separatrices corresponding to $\cos\phi_s$ of 0.05, 0.1 and 0.3. The "bucket" areas inside the separatrices are the particle phase stable regions. A small $\cos\phi_s$ value leads to a larger stable bucket area.

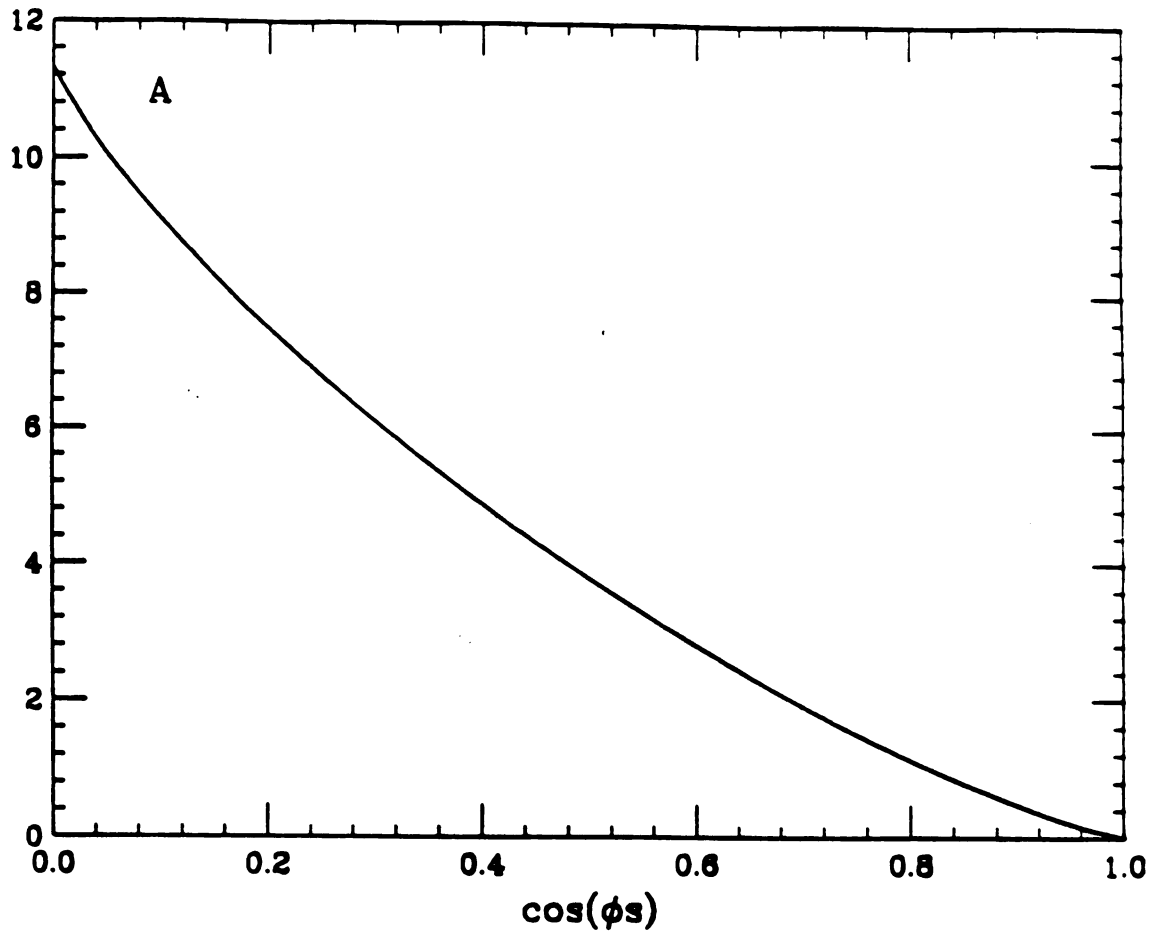


Fig. 6-2 -- Plot of the normalized bucket area A vs. the synchronous phase $\cos\phi_s$. $A = \int F^{1/2}(\phi, \phi_s) d\phi$.

$$S = \frac{1}{\omega_s} \left(\frac{2eV_d E_s}{\pi K} \right)^{1/2} \int F^{1/2}(\phi, \phi_s) d\phi.$$

Therefore the true constant bucket area condition is

$$S = \frac{1}{\omega_s} \left(\frac{2eV_d E_s}{\pi K} \right)^{1/2} A = \text{constant},$$

where A is the normalized bucket area given above. Thus this condition relates V_d and $\cos\phi_s$ at each energy value. The value of S is determined by the initial conditions in the central region, and we have already assumed that $V_d = 20$ kV there. This leaves the initial value of $\cos\phi_s$ which is determined by the value chosen for $-(\frac{df}{dt})_1$.

The results given in chapter 5 show that the average capture time reaches its peak value of $4.5 \mu\text{s}$ at $(-\frac{df}{dt})_1 = 49.71 \text{ MHz/ms}$, which corresponds to $\cos\phi_{s1} = 0.073$. As is shown in Fig. 2-8, because of the magnet shimming in the central region, the resultant K value increases from 2.2 in the center to 3.2 at a radius of 0.5 inches. With a constant S, the resultant $\cos\phi_s$ (and hence energy gain) drops to a value that is too small for protons to gain adequate energy in this region. Using a large $\cos\phi_{s1}$ will improve the initial energy gain but lead to a smaller stability area and average capture time, as one can see from Fig. 6-2 and Fig.

5-14. This would then reduce the captured beam current. On balance, these considerations lead to the choice $\cos\phi_{si} = 0.105$ which corresponds to the initial frequency time derivative $(-\frac{df}{dt})_i = 71.02$ MHz/ms. As a result, we obtain a good proton initial energy gain and an average capture time of 4.3 μ s which is close to the peak value.

6.2 Fixed Dee Voltage

Given the initial synchronous phase $\cos\phi_{si}$ and dee voltage V_d , the initial bucket area is obtained from:

$$S_i = \frac{1}{\omega_o} \left(\frac{2eV_d E_o}{\pi K_o} \right)^{1/2} A(\cos\phi_{si})$$

where E_o is the rest energy of the proton, and K_o and ω_o are the K value and proton angular frequency in the center respectively. Since the equilibrium orbit code determines the K and ω_s as functions of the energy, then assuming $V_d = 20$ kV remains fixed during the acceleration, the constant bucket area condition:

$$S = \frac{1}{\omega_s} \left(\frac{2eV_d E_s}{\pi K} \right)^{1/2} A(\cos\phi_s) = S_i$$

gives $\cos\phi_s$ as a unique function of the synchronous particle energy. The required frequency time derivative $(-\frac{df}{dt})$ of the RF system is then determined from:

$$\left(-\frac{df}{dt}\right) = K\left(\frac{\omega_s}{2\pi}\right)^2 \left(\frac{2eV_d}{E_s}\right)\cos\phi_s.$$

Figures 6-3 and 6-4 show plots of the resultant $\cos\phi_s$ value and the required frequency time derivative $(-\frac{df}{dt})$ vs. energy, respectively.

6.3 Fixed Synchronous Proton Energy Gain per Turn

As shown in Fig. 6-3, using an RF frequency program with a fixed dee voltage $V_d = 20$ kV, leads to values of $\cos\phi_s$ that increase with energy rapidly and reach over 0.4 between 175 MeV and 250 MeV. However, the extraction calculations described in chapter 3 are based on an energy gain per turn of 10 keV which corresponds to $\cos\phi_s = 0.25$. Moreover, since one can economize on RF power by having V_d decrease during the FM cycle, we next explored the option of restricting the maximum value of the synchronous proton energy gain per turn ($E_{\text{turn}} = 2eV_d\cos\phi_s$) to 10 keV.

The fixed dee voltage of 20 kV is still used in the small energy region where the synchronous phase $\cos\phi_s$ is

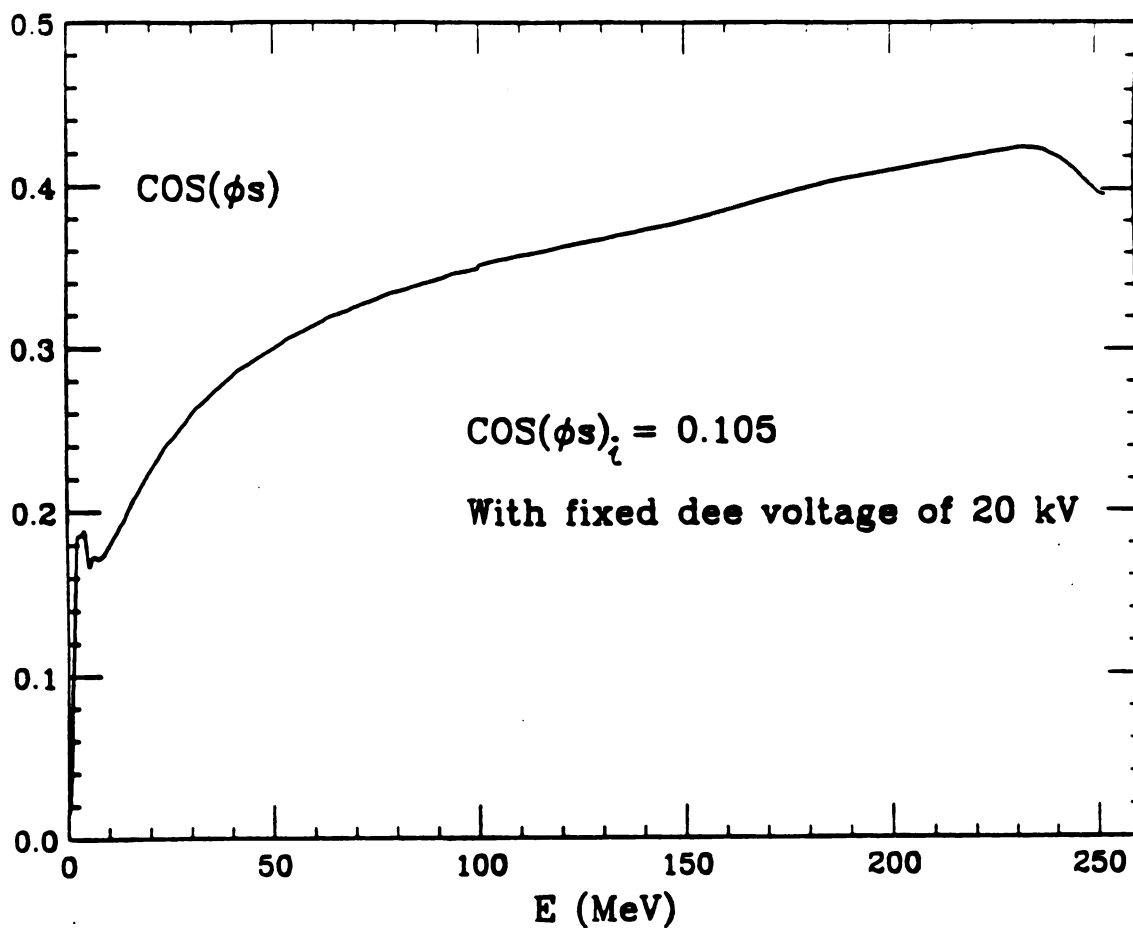


Fig. 6-3 -- Plot of the resultant synchronous phase $\cos\phi_s$ vs. energy with a fixed dee voltage $V_d = 20$ kV.

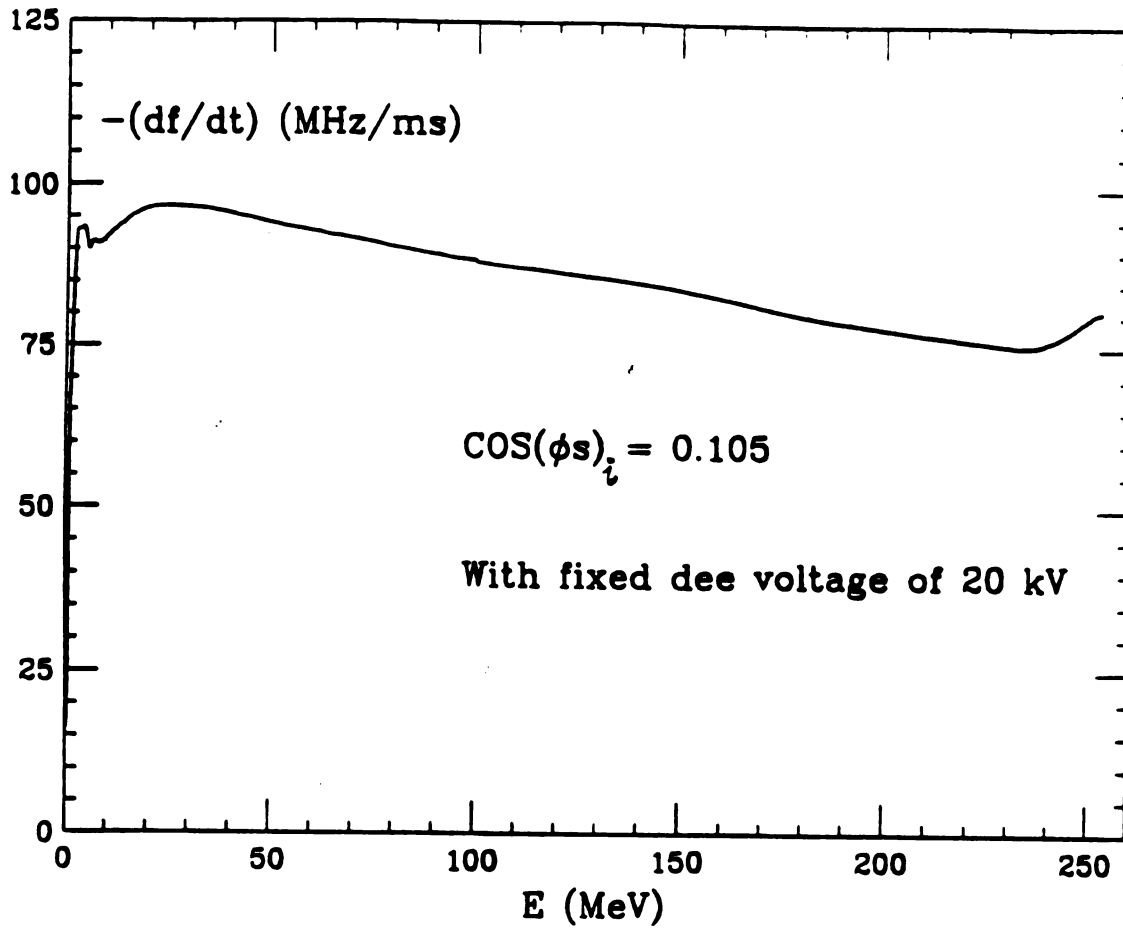


Fig. 6-4 -- Plot of the required frequency time derivative $(-\frac{df}{dt})$ vs. energy with a fixed dee voltage $V_d = 20$ kV.

smaller than 0.25. Once $\cos\phi_s$ reaches 0.25, which leads to an synchronous proton energy gain per turn of 10 keV, the dee voltage is reduced to keep the synchronous proton energy gain per turn fixed at 10 keV.

The constant bucket area condition given above can be rewritten as follows:

$$S = \frac{1}{\omega_s} \left(\frac{E_{\text{turn}} E_s}{\pi K \cos\phi_s} \right)^{1/2} A = S_i$$

or,

$$S = \frac{1}{\omega_s} \left(\frac{E_{\text{turn}} E_s}{\pi K} \right)^{1/2} A' = S_i$$

where $E_{\text{turn}} = 2eV_d \cos\phi_s$ is fixed and $A' = \frac{A}{(\cos\phi_s)^{1/2}}$ is a

new unique function of $\cos\phi_s$. This A' is plotted in Figure 6-5.

Using the new constant bucket area condition and the known values of ω_s and K , one can then find $\cos\phi_s$ as a function of the synchronous energy E_s . The required frequency time derivative $(-\frac{df}{dt})$ and the dee voltage of the RF system can then be calculated from:

$$\left(-\frac{df}{dt}\right) = K \left(\frac{\omega_s}{2\pi}\right)^2 \left(\frac{E_{\text{turn}}}{E_s}\right)$$

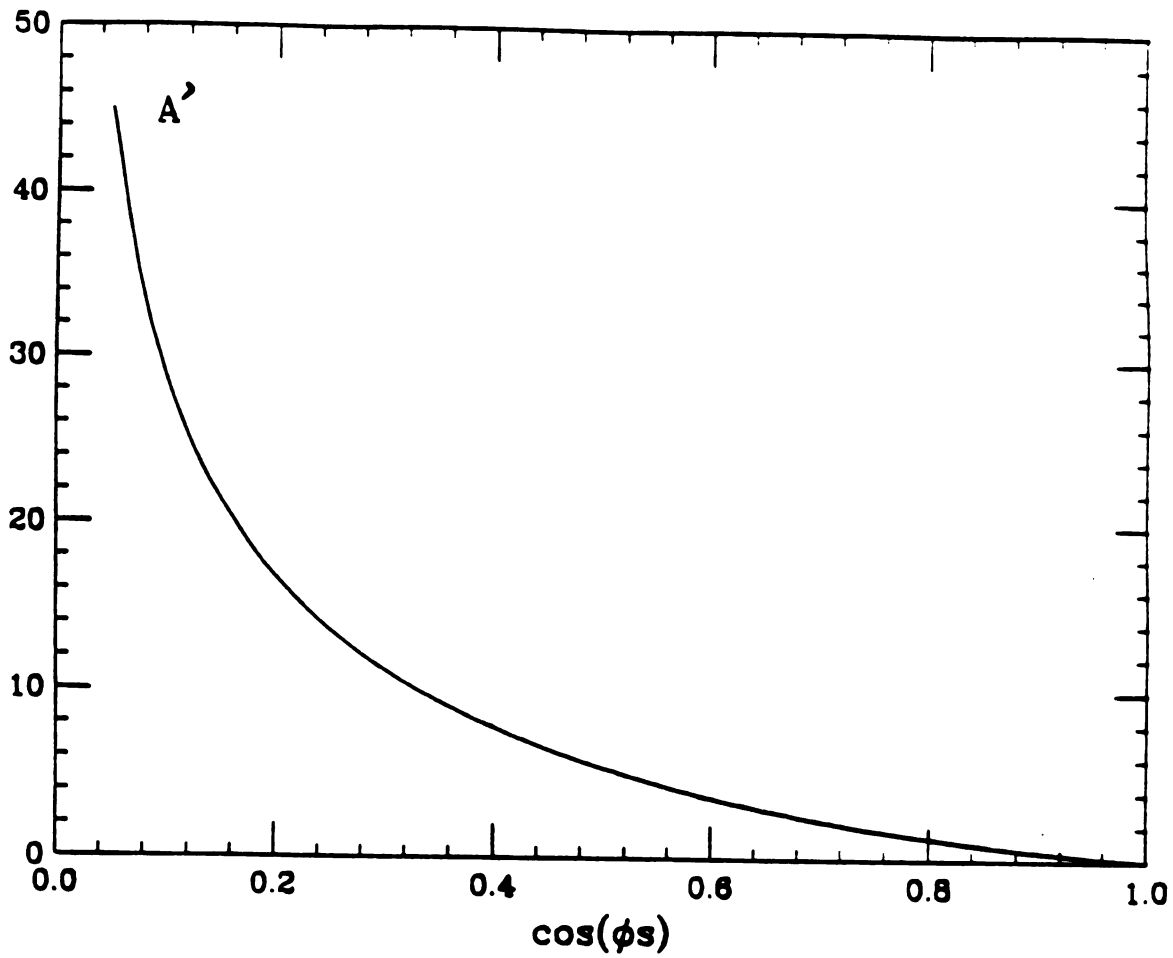


Fig. 6-5 -- Plot of A' vs. synchronous phase $\cos\phi_s$.

$$A' = \frac{A}{(\cos\phi_s)^{1/2}} .$$

and
$$V_d = \frac{E_{\text{turn}}}{2e \cos \phi_s}.$$

Figure 6-6 shows a plot of the new values of $\cos \phi_s$ vs. energy. This $\cos \phi_s$ crosses 0.25 at 27.5 MeV which is the switching point from a fixed dee voltage of 20 kV to a fixed synchronous proton energy gain of 10 KeV/turn. The required frequency time derivative ($-\frac{df}{dt}$) and the dee voltage of the RF system V_d are plotted in Fig. 6-7 and Fig. 6-8, respectively. As can be seen, V_d drops to a minimum value of 13.8 kV at 235 MeV and rises to a final value near 15 kV.

6.4 Acceleration Time

From the average energy gain per turn, $2eV_d \cos \phi_s$, the following expression for the acceleration time T is obtained:

$$T = \int \frac{\pi dE_k}{\omega e V_d \cos \phi_s},$$

where the integral over kinetic energy E_k ranges from zero to $E_k = 250$ MeV. The integration can be performed using the equilibrium orbit code results for ω and the energy dependence of V_d and $\cos \phi_s$ found above. For the case with fixed dee voltage $V_d = 20$ kV, the result is $T = 0.275$ ms,

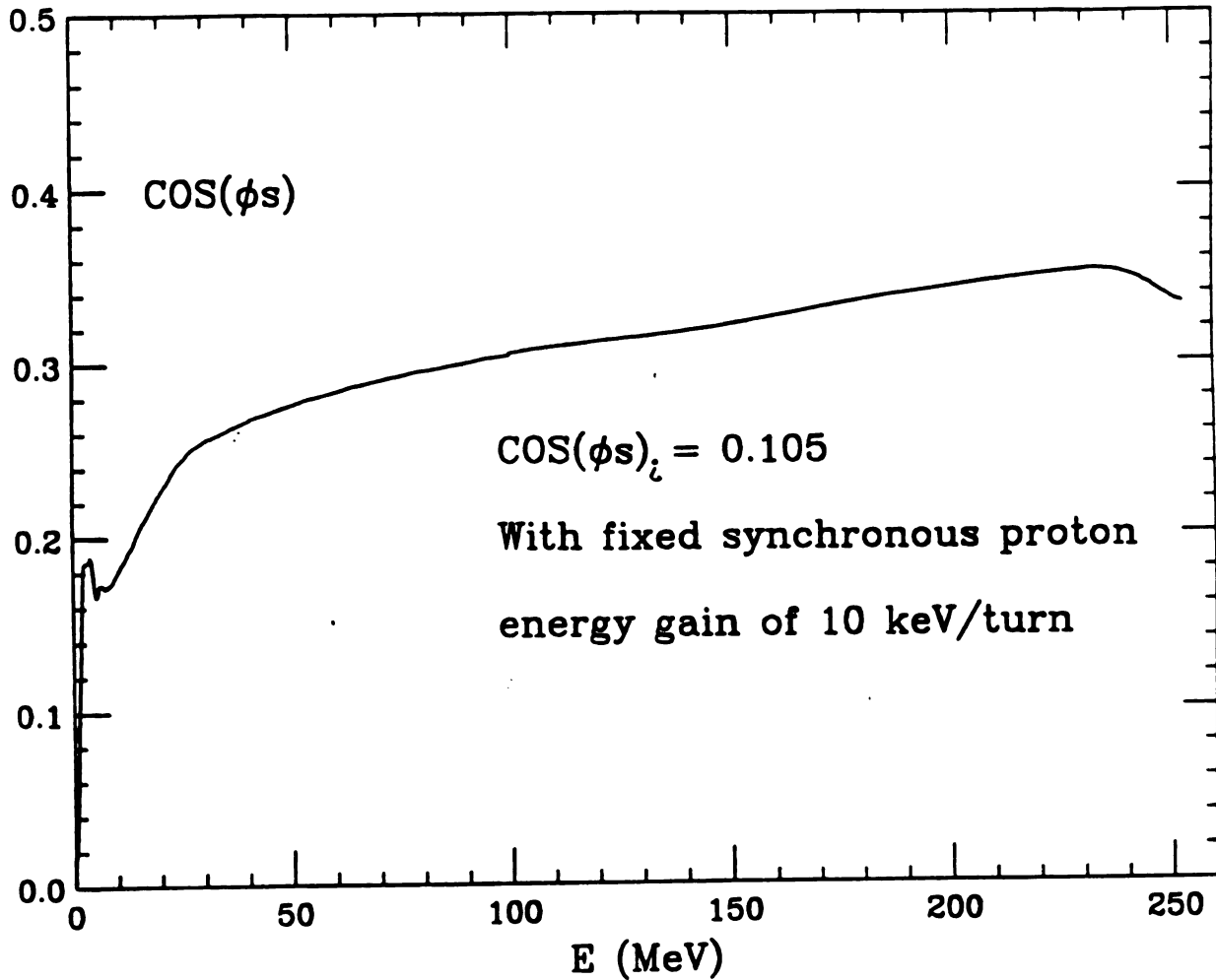


Fig. 6-6 -- Plot of the resultant $\cos\phi_s$ vs. energy with fixed synchronous proton energy gain of 10 keV/turn at large energies. This $\cos\phi_s$ crosses 0.25 at 27.5 MeV which is the switching point from a fixed dee voltage of 20 kV to a fixed synchronous proton energy gain of 10 KeV/turn.

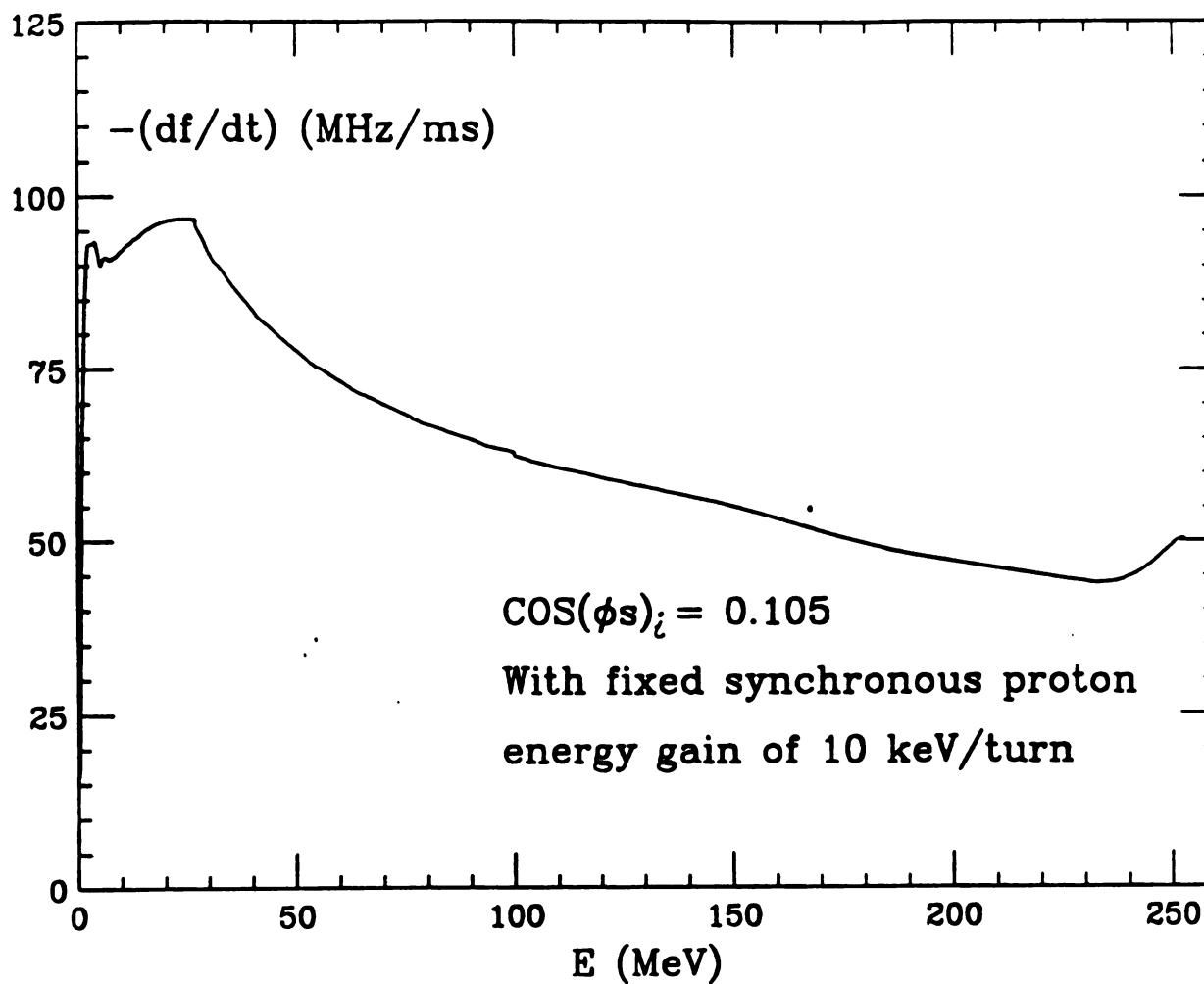


Fig. 6-7 -- Plot of the required frequency time derivative $(-\frac{df}{dt})$ vs. energy with fixed synchronous proton energy gain of 10 keV/turn at large energies. The $\text{cos}\phi_s$ crosses 0.25 at 27.5 MeV which is the switching point from a fixed dee voltage of 20 kV to a fixed synchronous proton energy gain of 10 KeV/turn.

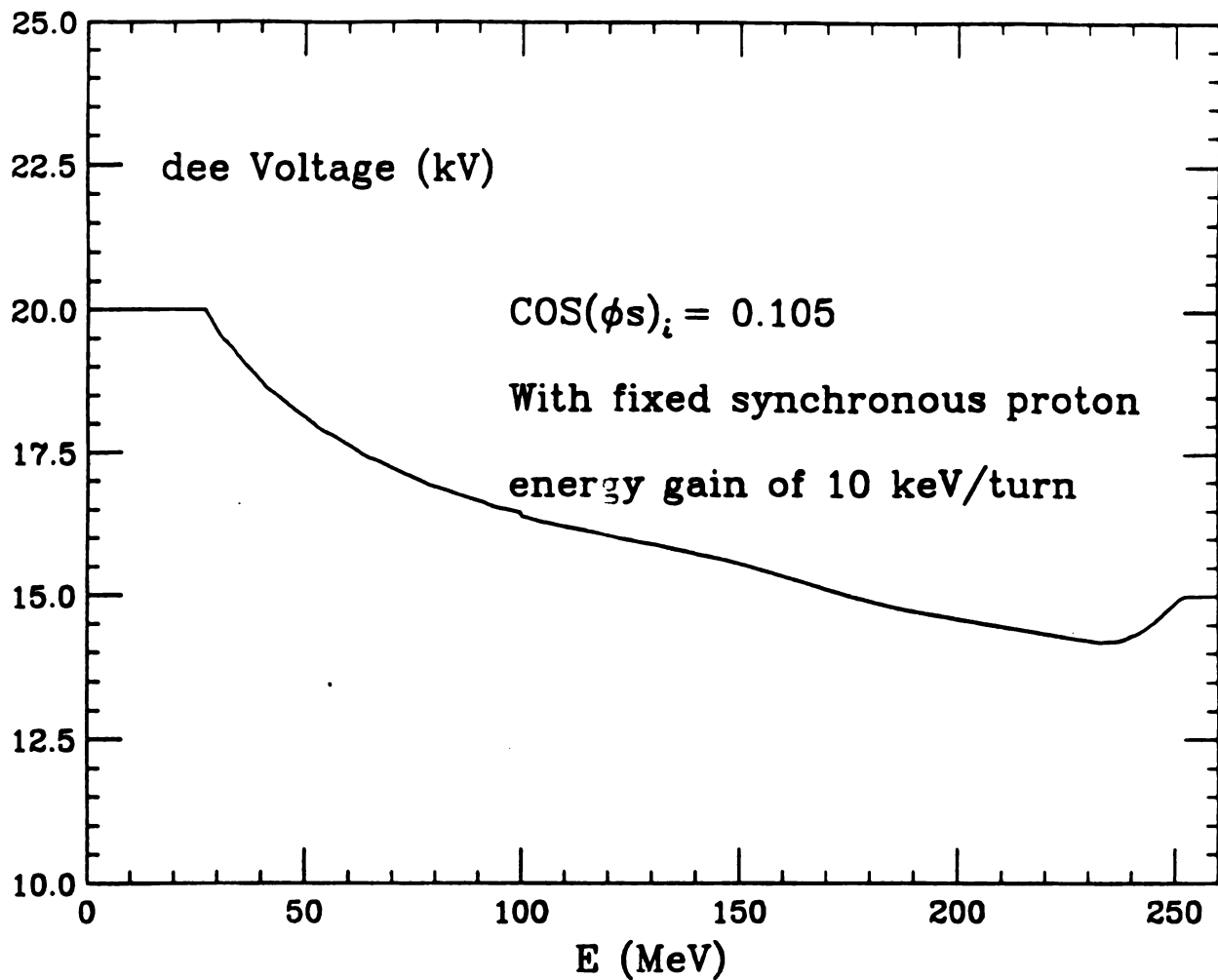


Fig. 6-8 -- Plot of the required dee voltage of RF system vs. energy with a fixed synchronous proton energy gain of 10 KeV/turn at large energies. The $\text{cos}\phi_s$ crosses 0.25 at 27.5 MeV which is the switching point from a fixed dee voltage of 20 kV to a fixed synchronous proton energy gain of 10 KeV/turn.

while for the case with fixed synchronous proton energy gain per turn $E_{\text{turn}} = 10 \text{ keV}$, the value is $T = 0.378 \text{ ms}$. These times are significantly shorter than the 1.0 ms FM period that corresponds to an assumed repetition rate of 1.0 kHz.

Finally, the required parameters of the RF system for the 250 MeV superconducting synchrocyclotron are listed in Table 6-1.

Table 6-1

<u>Parameter</u>	<u>RF system with fixed dee voltage</u>	<u>RF system with fixed energy gain</u>
Initial dee voltage	20.00 kV	20.00 kV
Final dee voltage	20.00 kV	15.00 kV
Acceleration time	0.275 ms	0.378 ms
Modulation frequency	1 kHz	1 kHz
Initial frequency	84.27 MHz	84.27 MHz
Final frequency	61.75 MHz	61.75 MHz
Initial frequency time derivative	71.02 MHz/ms	71.02 MHz/ms
Final frequency time derivative	80.82 MHz/ms	50.40 MHz/ms

Chapter 7

Summary and Conclusions

This thesis describes a conceptual design and the orbit dynamics of a 250 MeV superconducting synchrocyclotron for use in proton cancer therapy. The goal was to explore possible solutions to problems in the magnet, extraction system and central region design with the aim of demonstrating the feasibility of such a machine.

This superconducting synchrocyclotron has an output proton energy of 250 MeV, which is sufficient for irradiation of most patients since it corresponds to a range in tissue of 37 cm. This machine should have a beam current of 20 - 100 nA as required for its purpose. The calculated space-charge limited current is about 2.8 μ A with dee voltage of 20 kV, modulation frequency of 1 kHz and proton starting phase range of 60° [38,39,40]. It would also be very compact and light, since the radius of the outer yoke of the magnet is only 53 inches and the approximate weight of the accelerator plus the counterweight and the supporting system is about 150 tons. It seems well suited to a hospital environment and should have reasonable cost.

The superconducting magnet designed for this machine produces a central field of 55.3 kG which is about three times stronger than the field in conventional synchrocyclotrons. The superconducting coil has a simple rectangular cross section and carries a current density of 5200 amps per square centimeter. The calculation results of the equilibrium orbit code indicate that the magnetic field provides adequate radial and vertical focusing for the beam. The magnet configuration is also designed to reduce its size and weight while keeping the fringe magnetic field within an acceptable limit. The shimming of the magnet in the central region improved the magnetic field shape and optimized the capture time.

The extraction system is based on a regenerator followed by a passive magnetic channel which contains a series of deflecting and focusing elements. The Z^4 orbit code was used to perform the orbit tracking and extraction efficiency calculations for different initial conditions, and proved to be a useful tool for investigating the nonlinear effects in the extraction system. The results show that an extraction efficiency of about 40% can be achieved, using the extraction system presented, if the internal beam can be controlled so that both the radial and vertical amplitudes

do not exceed 3 mm. The required control of the internal beam depends ultimately on the design of the central region.

Ion source experiments show a strong dependence of the ion current from an enclosed ion source on the shape and size of the source chimney and slit. The results of the studies reported in chapter 4 indicate that it is possible to obtain enough ion current from an enclosed ion source with a very small diameter chimney, about 0.1 in., to meet the beam current requirement for the 250 MeV superconducting synchrocyclotron. The ion source could be similar to the Harper superconducting cyclotron ion source.

An electrode configuration was designed for the source-puller and dees that is consistent with the limited space available in the central region. The proposed dee voltage is 20 kV. A circular chimney aperture and small gap of 1.5 mm between the source chimney and the puller should be used to increase the internal ion current. The CYCLONE orbit code was used to perform the orbit calculations in the central region. The results show that the proposed design provides adequate vertical focusing and reasonably good centering for the orbits in the central region. In addition, the proton orbits have a phase acceptance of about 50° and a reasonable energy gain.

A transfer matrix program was also developed to continue the orbit calculations beyond the central region and hence

to determine the capture time for different values of the frequency time derivative. The results indicate that the capture time depends strongly on the magnetic field shape in the central region as well as $(-\frac{df}{dt})_i$, the initial frequency time derivative. The proposed modulation frequency is 1 kHz. Our results indicate an optimum capture efficiency of 0.43%, which corresponds to an initial beam current of 1.1 μ A. Finally, we studied two possible RF frequency programs that meet the requirement of keeping a constant bucket area during the acceleration and hence avoid the loss of protons.

In conclusion, this work has produced possible solutions to design problems of the magnet, extraction system, and central region by using relevant orbit calculations to confirm the results. However, further work is needed to finalize and improve the 250 MeV superconducting synchrocyclotron design. For instance, using a return coil at the corner of the outer yoke could control more effectively the fringe field of the magnet without significantly altering the field in the region of beam. In addition, a new RF system using electronic tuning should be designed to provide a 1 kHz modulation rate for a frequency range from 84.27 MHz down to 61.75 MHz. This high modulation rate and large RF frequency range severely complicates the RF design problems. Another alternative is to use a magnet

with sectors in order to make the field more isochronous and thereby reduce the required frequency range.

APPENDIX A

Geometry and Position of the Regenerator

As shown in Fig. A-1, the regenerator consists of 5 parts and is symmetric about the median plane. Each regenerator part consists of several iron rings with rectangular cross section and different angular width.

The geometry and position of the iron rings of the regenerator are given as following: (See Figure A-2)

$$\begin{array}{cccccc}
 n_1 & r_1 & r_2 & & & \\
 & \theta_{1i} & \theta_{2i} & z_{1i} & z_{2i} &
 \end{array}$$

where n_1 is the number of the rings in each regenerator part and $i = 1, 2, \dots, n_1$.

Part 1:

3	19.25	19.5		
	162	198	1.800	2.200
	165	195	1.400	1.800
	168	192	1.000	1.400

Part 2:

3	19.5	21.0		
	162	198	1.375	1.875
	165	195	1.000	1.375
	168	192	0.625	1.000

Part 3:

1	20.00	20.75		
	171	189	0.500	0.625

Part 4:

3	21.0	21.25		
	162	198	1.500	1.875
	165	195	1.125	1.500
	168	192	0.875	1.125

Part 5:

3	21.25	21.5		
	162	198	1.625	1.875
	165	195	1.500	1.625
	168	192	1.375	1.500

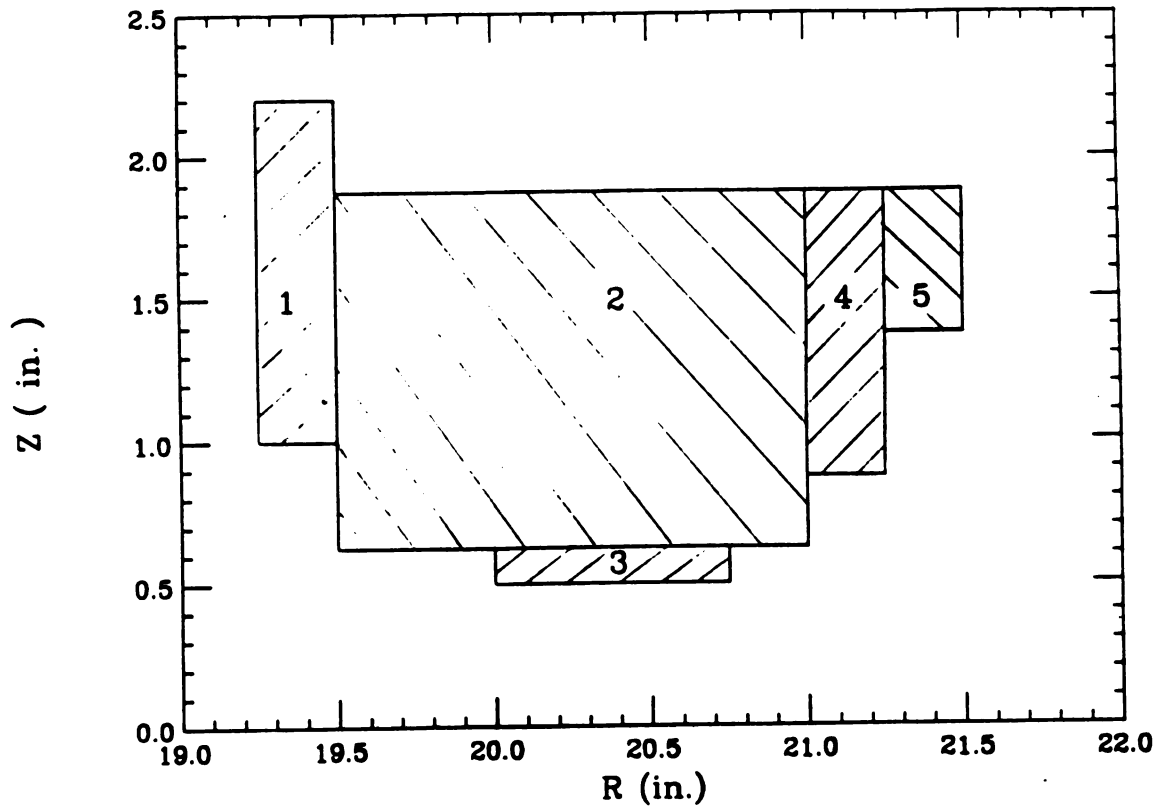


Fig. A-1 -- The radial profile of the regenerator above the median plane. The regenerator consists of 5 parts and is symmetric about the median plane. Each regenerator part consists of several iron rings with rectangular cross section and different angular width.

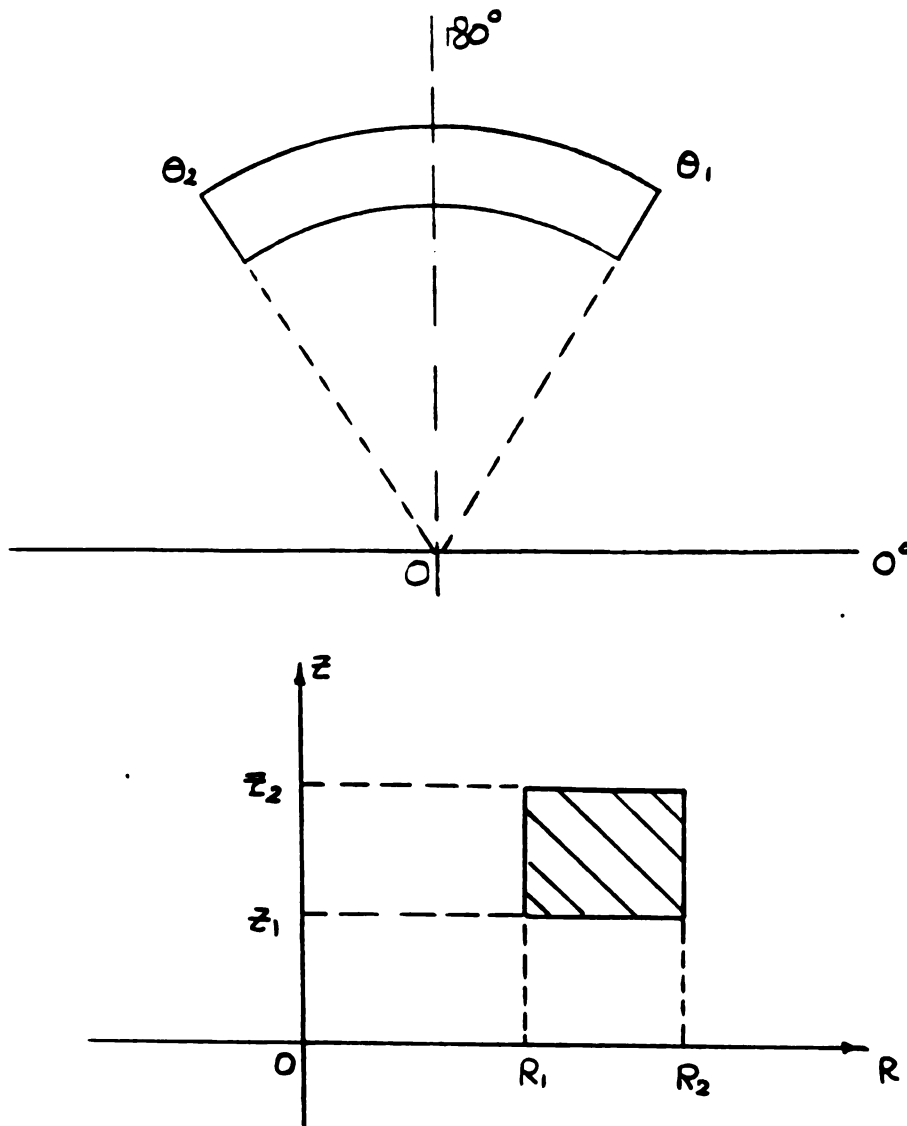


Fig. A-2 -- Coordinates required to define the iron rings in the each regenerator part.

APPENDIX B

Geometry and Position of the Magnetic Channel Elements

The geometry and position of the rectangular iron bars of the magnetic channel elements are given as following: (See Figure B-1)

n_1	r_b	B	a	l_1	l_2
	x_{oi}	dx_i	z_{oi}	dz_i	

where n_1 is the number of the rectangular iron bars in the channel element and $i = 1, 2, \dots, n_1$. r_b is the distance from the machine center and the center of the channel aperture.

M1:

10	20.16880	103.13000	3.53510	1.10000	1.10000
-0.3750	0.12500	-0.3	0.6		
0.25	0.125	-0.3	0.6		
-2.2	1.0	0.585	0.015		
-2.2	1.0	-0.6	0.015		
-1.2	0.675	0.55	0.05		
-1.2	0.675	-0.6	0.05		
-0.525	0.15	0.3	0.3		
-0.525	0.15	-0.6	0.3		
0.375	0.15	0.3	0.3		
0.375	0.15	-0.6	0.3		

M2:

10	20.33750	111.00000	3.48248	1.10000	1.10000
	-0.4250	0.12500	-0.3	0.6	
	0.3	0.125	-0.3	0.6	
	-2.4	1.2	0.585	0.015	
	-2.4	1.2	-0.6	0.015	
	-1.2	0.63	0.545	0.055	
	-1.2	0.63	-0.6	0.055	
	-0.57	0.17	0.31	0.29	
	-0.57	0.17	-0.6	0.29	
	0.4	0.17	0.31	0.29	
	0.4	0.17	-0.6	0.29	

M3:

11	20.51080	119.00000	3.46164	1.10000	1.10000
	-0.3750	0.12500	-0.25000	0.50000	
	0.25	0.125	-0.5	0.25	
	0.25	0.125	0.25	0.25	
	-2.2	0.9	0.59	0.01	
	-2.2	0.9	-0.6	0.01	
	-1.3	0.775	0.56	0.04	
	-1.3	0.775	-0.6	0.04	
	-0.525	0.15	0.3	0.3	
	-0.525	0.15	-0.6	0.3	
	0.375	0.15	0.3	0.3	
	0.375	0.15	-0.6	0.3	

M4:

11	20.68270	127.00000	3.37151	1.10000	1.10000
	-0.3750	0.12500	-0.25000	0.50000	
	0.25	0.125	-0.5	0.25	
	0.25	0.125	0.25	0.25	
	-2.2	0.9	0.59	0.01	
	-2.2	0.9	-0.6	0.01	
	-1.3	0.775	0.56	0.04	
	-1.3	0.775	-0.6	0.04	
	-0.525	0.15	0.3	0.3	
	-0.525	0.15	-0.6	0.3	
	0.375	0.15	0.3	0.3	
	0.375	0.15	-0.6	0.3	

M5:

10	20.85780	135.00000	3.53982	1.10000	1.10000
	-0.5500	0.25000	-0.37000	0.74000	
	0.300	0.25	-0.370	0.74	
	-2.5	1.0	0.58	0.02	
	-2.5	1.0	-0.6	0.02	
	-1.5	0.65	0.54	0.06	
	-1.5	0.65	-0.6	0.06	
	-0.85	0.3	0.37	0.23	
	-0.85	0.3	-0.6	0.23	
	0.55	0.3	0.37	0.23	
	0.55	0.3	-0.6	0.23	

M6:

10	21.04970	143.00000	3.97369	1.10000	1.10000
	-0.5500	0.25000	-0.37000	0.74000	
	0.300	0.25	-0.370	0.74	
	-2.5	1.0	0.58	0.02	
	-2.5	1.0	-0.6	0.02	
	-1.5	0.65	0.54	0.06	
	-1.5	0.65	-0.6	0.06	
	-0.85	0.3	0.37	0.23	
	-0.85	0.3	-0.6	0.23	
	0.55	0.3	0.37	0.23	
	0.55	0.3	-0.6	0.23	

M7:

9	21.33730	154.00000	4.48647	2.10000	2.10000
	-0.600	0.30000	-0.3000	0.60000	
	0.3	0.3	-0.60	0.3	
	0.3	0.3	0.3	0.3	
	-2.70	1.0	0.58	0.02	
	-2.70	1.0	-0.6	0.02	
	-1.7	0.7	0.545	0.055	
	-1.7	0.7	-0.6	0.055	
	-1.0	0.3	0.4	0.2	
	-1.0	0.3	-0.6	0.2	

M8:

3	21.85200	170.00000	5.23136	2.10000	2.10000
	-0.6000	0.30000	-0.30000	0.6000	
	0.3	0.3	-0.6	0.3	
	0.3	0.3	0.3	0.3	

M9:

3	22.77530	192.00000	7.28685	2.10000	2.10000
	-0.6000	0.30000	-0.30000	0.60000	
	0.3	0.3	-0.6	0.3	
	0.3	0.3	0.3	0.3	

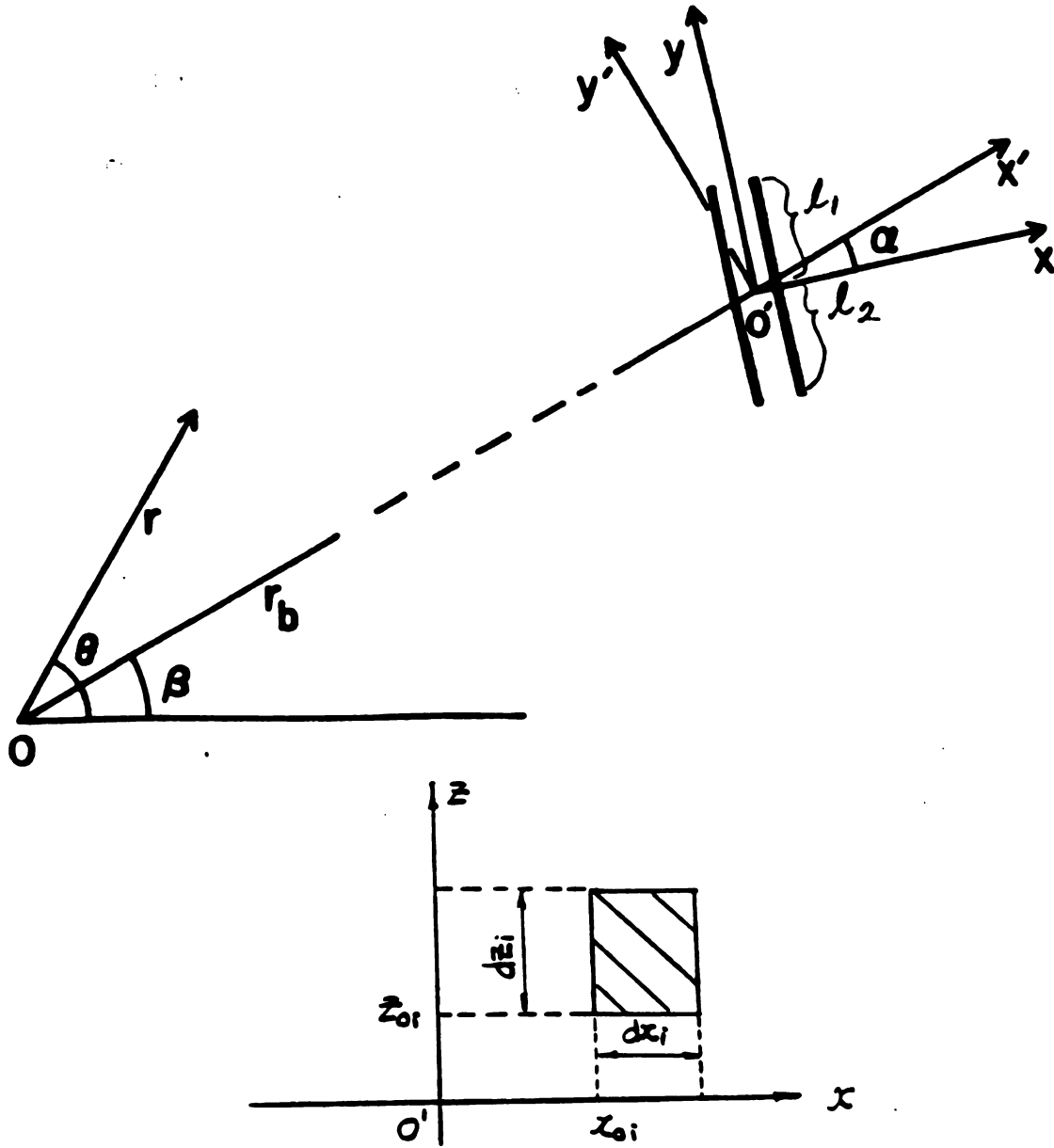


Fig. B-1 -- Coordinates required to define the rectangular iron bars in the magnetic channel element. O is the machine center and O' is the center of channel aperture.

APPENDIX C

Transfer Matrix Program Equations

In Transfer Matrix Program, instead of (x, p_x) , we use (x, \dot{x}) where $\dot{x} = R \frac{p_x}{p}$. Suppose that after the n gap crossing, the variables have the values x_n, \dot{x}_n, E_n and $\omega_0 t_n$. Given E_n , one can calculate the corresponding values of $R, \frac{E}{E_0}$ and v_r by interpolation from a table of E. O. data.

Just before the next $(n+1)$ gap crossing, the values of the variables are:

$$x_{n+1} = x_n \cos(\pi v) + \frac{\dot{x}_n}{v} \sin(\pi v)$$

$$\dot{x}_{n+1} = -v x_n \sin(\pi v) + \dot{x}_n \cos(\pi v)$$

$$\omega_0 t_{n+1} = \omega_0 t_n + \frac{1}{R} \left(\frac{\omega_0}{\omega} \right) \left\{ R\pi + \frac{x_n}{v} \sin(\pi v) + \frac{\dot{x}_n}{v^2} [1 - \cos(\pi v)] \right\}$$

where $v = v_r$. Of course, E_n does not change here.

Assuming the dee voltage varies as $\cos(\int \omega_r f dt)$, the energy change at the gap crossing is:

$$E_{n+1} = E_n + qV_d \cos \phi_{n+1}$$

where ϕ_{n+1} is the phase at the (n+1) gap crossing,

$$\phi_{n+1} = \phi_n + [1 + \epsilon - \frac{\lambda}{4\pi}(\omega_0 t_{n+1} + \omega_0 t_n)](\omega_0 t_{n+1} + \omega_0 t_n) - \pi$$

Since the value of $r = R + x$ does not change at the gap crossing, the value of x_{n+1} given above is replaced by

$$x_{n+1}^* = x_{n+1} - (R_{n+1} - R_n)$$

where R_n and R_{n+1} are the radius values of the E. O. data before and after the gap crossing. The values of \dot{x}_{n+1} and $\omega_0 t_{n+1}$ do not change at the gap crossing. The resultant values of x_{n+1}^* , x_{n+1} , E_{n+1} , and $\omega_0 t_{n+1}$ together with ϕ_{n+1} become the input values for the transfer to the next gap crossing.

The input is obtained from the output of part II of CYCLONE at a radius $R_0 \approx 0.4$ inch. If this output is at $\theta = \frac{\pi}{2}$, then a special routine is needed to transport the orbit to the next gap crossing ($\Delta\theta = \frac{\pi}{2}$). Suppose that if $\theta = \frac{\pi}{2}$, the variables are x_0 , \dot{x}_0 , E_0 and ϕ_0 . Then at the next gap crossing ($\theta = \pi$) the variables are:

$$x_1 = x_0 \cos(\frac{1}{2}\pi v) + \frac{\dot{x}_0}{v} \sin(\frac{1}{2}\pi v)$$

$$\dot{x}_1 = -v x_0 \sin(\frac{1}{2}\pi v) + \dot{x}_0 \cos(\frac{1}{2}\pi v)$$

$$\omega_0 t_1 = \omega_0 t_0 + \frac{1}{R} \left(\frac{\omega_0}{\omega} \right) \left\{ \frac{1}{2} R \pi + \frac{x_0}{v} \sin\left(\frac{1}{2} \pi v\right) + \frac{\dot{x}_0}{v^2} [1 - \cos\left(\frac{1}{2} \pi v\right)] \right\}$$

Here we take $\omega_0 t_0 = 2\pi j_0$, where j_0 is the number of turns the orbit has traveled in CYCLONE.

At $\theta = \pi$, the energy gain and the phase values are:

$$E_1 = E_0 + qV_d \cos\phi_1$$

with $\phi_1 = \phi_0 + [1 + \epsilon - \frac{\lambda}{4\pi}(\omega_0 t_1 + \omega_0 t_0)](\omega_0 t_1 + \omega_0 t_0) - \frac{1}{2}\pi$

Also the change in x_1 is calculated by:

$$x_1^* = x_1 - (R_1 - R_0) .$$

LIST OF REFERENCES

1. R. R. Wilson, *Radiology* 47 (1946) 487.
2. C. A. Tobias, H. O. Anger and J. H. Lawrence, *Am. J. Roentgenol. Rad. Ther. Nucl. Med.* 67 (1952) 1.
3. B. Gottschalk, *Fermi National Accelerator Laboratory Report Appendix* (1986) 1.
4. B. Larson, L. Leksell and R. Rexed, *Acta Chir. Scand.* 125 (1963) 1.
5. R. N. Kjellberg, et. al., *Trans. Amer. Neurol. Assoc.* 87 (1962) 216.
6. A. M. Koehler, *Proc. 9th Int. Conf. on Cyclotrons and Their Applications*, (Courtaboeuf, 1981) 667.
7. I. Riabukhin, *International Workshop on Particle Accelerator in Radiation Therapy*, Houston, Texas (1982).
8. L. Teng, D. Young and et. al., *Fermi National Accelerator Laboratory Report* (1986).
9. J. M. Slater, *Proceedings of the 5th PTCOG Meeting*, Report LBL-22962 (1987) 129.
10. H. Blosser, et. al., *NSCL Annual Report* (1986) 194.
11. H. Blosser, et. al., *Proc. of the 1989 Particle Accelerator Conf. 2* (IEEE, New York, 1989) 742.

12. H. Blosser, et. al., Proc. 11th Int. Conf. on Cyclotrons and their Applications, Ionics (1987) 157.
13. M. M. Gordon, Particle Accelerators 16 (1984) 39.
14. E. Braunersreuther, et. al., Proc. 7th Int. Conf. on Cyclotrons and their Applications, (Birkhauser, Basel, 1975) 187.
15. Powell, Henrick, Kearns Sewell and Thornton, Rev. Sci. Instr. 19 (1948) 506.
16. C. E. Leith, Phys. Rev. 78 (1950) 89.
17. J. Tuck and L. C. Teng, Chicago Progress Report III (1949-1950).
18. K. J. LeCouteur, Proc. Phys. Soc. B 64 (1951) 1073.
19. K. J. LeCouteur, Proc. Phys. Soc. B 66 (1953) 25.
20. K. J. LeCouteur and S. Lipton, Phil. Mag. 46 (1955) 1265.
21. S. Cohen and A. V. Grewe, Nucl. Instr. 1 (1957) 31.
22. A. V. Crewe and U. E. Kruse, Rev. Sci. Instr. 27 (1956) 5.
23. G. Calame, et. al., Nucl. Instr. and Meth. I (1957) 169.
24. B. Allardyce, et. al., Proc. 7th Int. Conf. on Cyclotrons and their Applications, (Birkhauser, Basel, 1975) 287.
25. S. Lindback, Proc. 5th International Cyclotron Conf., (Butterworths, London, 1971) 235.

26. M. M. Gordon and V. Taivassalo, Nucl. Instr. and Meth. **A247** (1986) 423.
27. M. M. Gordon and X. Y. Wu, Proc. of the 1987 Particle Accelerator Conf., (IEEE, New York, 1987) 1255.
28. X. Y. Wu and M. M. Gordon, Proc. 12th Int. Conf. on Cyclotrons and their Applications, (West Berlin, 1989)
29. H. Blosser, et. al., Proc. 10th Int. Conf. on Cyclotrons and their Applications, IEEE (1984) 431.
30. X. Y. Wu and H. Blosser, NSCL Annual Report, (1989).
31. C. Kost, TRIUMF, U. B. C., Canada.
32. R. Galiana, et. al., Proc. 7th Int. Conf. on Cyclotrons and their Applications, (Birkhauser, Basel, 1975) 371.
33. MSC Staff, CERN Internal Report MSC 67-5 (1967).
34. X. Y. Wu and M. M. Gordon, NSCL Annual Report, (1989).
35. F. Marti, M. M. Gordon and et. al., Proc. 9th Int. Conf. on Cyclotrons and their Applications, (Caen, France, 1981) 465.
36. D. Bohm and L. L. Foldy, Phys. Rev. **72** (1947) 649.
37. S. Kullander, CERN Report 66-27 (1966).
38. M. M. Gordon and X. Y. Wu, MSU Internal Report SC-4, (1987).
39. S. Holm, Proc. 5th International Cyclotron Conf., (Butterworths, London, 1971) 736.
40. S. Holm, Nucl. Instr. and Meth. **64** (1968) 317.

41. M. M. Gordon and Felix Marti, Particle Accelerators 12 (1982) 13.
42. M. Mallory and H. Blosser, IEEE Trans. on Nuclear Science, NS-13, 4 (1966) 163.
43. H. Blosser, et. al., Proc. 10th Int. Conf. on Cyclotrons and their Applications, IEEE (1984) 436.
44. H. Blosser, et. al., NSCL Annual Report (1989) 167.